1-29-2015 12:00 AM

Edge states and quantum Hall phases in graphene

Pavlo Piatkovskyi
The University of Western Ontario

Supervisor
Dr. Vladimir A. Miranskyy
The University of Western Ontario

Graduate Program in Applied Mathematics
A thesis submitted in partial fulfillment of the requirements for the degree in Doctor of Philosophy

Recommended Citation

Piatkovskyi, Pavlo, "Edge states and quantum Hall phases in graphene" (2015). *Electronic Thesis and Dissertation Repository*. 2675.
https://ir.lib.uwo.ca/etd/2675

EDGE STATES AND QUANTUM HALL PHASES IN GRAPHENE

(Thesis format: Integrated Article)

by

Pavlo Piatkovskyi

Graduate Program in Applied Mathematics

A thesis submitted in partial fulfillment
of the requirements for the degree of
Doctor of Philosophy

The School of Graduate and Postdoctoral Studies
The University of Western Ontario
London, Ontario, Canada

Abstract

The focus of this thesis is the dynamical symmetry breaking in monolayer and bilayer graphene in a magnetic field and the edge excitations in these systems. Due to the spin and valley degrees of freedom, the Coulomb interaction in graphene can lead to various broken-symmetry quantum Hall phases. The transport properties of each phase are affected by the low-energy edge excitations, and understanding the edge state properties can be crucial for identifying the true nature of the ground state.

We study edge states in biased bilayer graphene in a magnetic field within the four-band continuum model. The analysis is done for the semi-infinite graphene plane and for the graphene ribbon of a finite width, in the cases of zigzag and armchair edges. Exact dispersion equations for the edge states and analytic expressions for their wave functions are written in terms of the parabolic cylinder functions. The spectrum of edge states for each type of the boundary conditions is found by numerically solving the corresponding dispersion equations. The low-energy modes localized at zigzag edges are explored in detail.

In the case of monolayer graphene, we study edge excitations of the $\nu = 0$ quantum Hall state within the mean-field theory with different symmetry breaking terms. The analytical expressions for the continuum (Dirac) model wave functions are obtained for the charge density wave, Kekulé distortion, ferromagnetic and (canted) antiferromagnetic phases. The dispersion equations for each phase and boundary type (zigzag and armchair) are derived, numerically solved and compared to the results of the corresponding effective tight-binding model. The effect of the next-to-nearest neighbor hopping parameter on the edge state spectrum is studied and revealed to be essential. The criteria for the existence of gapless edge states are established for each phase and edge type.

Finally, we study different broken-symmetry quantum Hall phases in bilayer graphene with even filling factors. The gap equation is solved in the lowest Landau level approximation using the long-range screened Coulomb potential as well as the general form of the short-range interaction terms. Phase transitions driven by changing the external electric field and tilting the magnetic field are described.

Keywords: monolayer graphene, bilayer graphene, edge states, quantum Hall effect, dynamical symmetry breaking.

Co-Authorship Statement

This integrated-article thesis is based on three papers. Chapter 2 is based on the paper [1] for which I am the single author. Chapter 3 is based on the paper [2] for which Dr. V. A. Miransky formulated the problem and provided significant assistance in various aspects of the work. I was responsible for the numerical calculations and for the most part of the analytical derivation of results, and the manuscript was prepared by us together. Finally, Chapter 4 is based on yet to be published paper [3] in which Dr. V. A. Miransky formulated the problem and I performed the calculations.

The papers [1,2] are publications in an American Physical Society (APS) journal. This journal allows including this published or submitted material in this thesis, without requesting permission from the publisher. These copyright policies are outlined on the APS web site.

References

[1] P. K. Pyatkovskiy, *Edge states in bilayer graphene in a magnetic field*, Phys. Rev. B **88**, 205417 (2013).

[2] P. K. Pyatkovskiy and V. A. Miransky, *Spectrum of edge states in the* $\nu = 0$ *quantum Hall phases in graphene*, Phys. Rev. B **90**, 195407 (2014).

[3] P. K. Pyatkovskiy and V. A. Miransky, *Broken-symmetry quantum Hall states in bilayer graphene*, in preparation.

Acknowledgements

I would like to thank my supervisor Dr. Vladimir Miransky for his helpful guidance and assistance during the completion of my PhD studies. His insightful ideas, broad experience, and countless useful discussions we had immensely helped me advance as a physicist. I am sincerely grateful to Dr. Miransky for his patience, support, understanding and valuable advice in both science and life areas.

I gratefully acknowledge the financial support of my research by the Ontario Graduate Scholarship.

Finally, I wish to thank all my family. I am especially grateful to my wife Ganna for her love and encouraging me in the pursuit of my goals. I thank my parents and my son Yura for their love and support.

Contents

List of Figures

List of Abbreviations , Symbols, Nomenclature

AF	antiferromagnetic
CAF	canted antiferromagnetic
CDW	charge density wave
F	ferromagnetic
KD	Kekulé distortion
LL	Landau level
LLL	lowest Landau level
LP	layer polarized
NN	nearest neighbor
NNN	next-to-nearest neighbor
PLP	partially layer polarized
PSLP	partially spin-layer polarized

a	lattice constant
d	interlayer distance
$\Delta, \Delta', \tilde{\Delta}, \tilde{\Delta}_0$	mass gap parameters
$\epsilon_0 = \sqrt{2}\hbar v_F/l$	Landau energy scale in monolayer graphene
γ_1	interlayer hopping parameter
κ	dielectric constant
$l = \sqrt{\hbar c/\lvert eB_\perp\rvert}$	magnetic length
$\mu, \mu', \tilde{\mu}, \mu_0$	chemical potentials
$\mu_{\mathrm{Z}} = Z = \mu_{\mathrm{B}}B$	Zeeman splitting
μ_{B}	Bohr magneton
ν	filling factor
$\omega_c = \epsilon_0^2/(\hbar\gamma_1)$	cyclotron frequency in bilayer graphene
σ_i, $\tilde{\tau}_i$, τ_i	Pauli matrices
t	NN hopping parameter
t'	NNN hopping parameter
v_F	Fermi velocity

Chapter 1

Introduction

Graphene is an atomically thin flat sheet of carbon atoms with the hexagonal (honeycomb) lattice structure. This two-dimensional system is a building block for different carbon allotropes. The usual graphite has a layered structure and consists of weakly interacting two-dimensional graphene planes bound together by the weak van der Waals force. Carbon nanotubes and fullerene molecules can be viewed, respectively, as the nanometer-size cylinders and spheres made of graphene. The early theoretical studies of graphene [1–3], which started in 1947, were aimed at the description of the three-dimensional graphite and the model of an isolated graphene layer was considered as a starting point in all calculations.

The discovery of free-standing graphene in 2004 [4] that has been acclaimed by 2010 Nobel prize in Physics, initiated the extensive theoretical and experimental studies of this system. Graphene turned out to have outstanding mechanical and electrical properties, which made it a promising candidate for use in technology [5]. Moreover, the experiments with graphene in a magnetic fields [6, 7] performed right after its discovery confirmed the presence of the (pseudo)relativistic Dirac particles with the linear energy spectrum, predicted theoretically much earlier [8, 9]. A number of unusual for conventional condensed matter systems phenomena observed in graphene can be traced back to the relativistic-like nature of its charge carriers [10].

Bilayer graphene, a system consisting of two coupled graphene layers, has been discovered shortly after its monolayer counterpart [11] and became a separate subject of research due to its distinct features, unusual for two-dimensional condensed matter systems. The low-energy spectrum in bilayer graphene exhibits a quadratic band touching, while applying the perpendicular to the layers electric field results in the opening of a tunable band gap [12, 13].

Both monolayer and bilayer graphene provide the suitable playgrounds for exploring the many-body physics. In particular, the Coulomb interaction in the presence of magnetic field field leads to the splitting of degenerate Landau levels and a rich variety of possible broken-symmetry ground states.

1.1 Continuum model of graphene

1.1.1 Monolayer graphene

The linear relativistic-like spectrum of the charge carriers in graphene is a consequence of its honeycomb crystal structure (Fig. 1.1) with two atoms per unit cell giving rise to the two hexagonal sublattices *A* and *B*. The most straightforward and widely used way to derive the Dirac Hamiltonian is to use the simplest tight-binding model with only nearest-neighbor (NN) hopping parameter *t*:

$$H_0 = -t \sum_{\mathbf{n}} \sum_{i=1}^{3} \sum_{s=\pm} \left(a^{\dagger}_{\mathbf{n},s} b_{\mathbf{n}+\boldsymbol{\delta}_i,s} + b^{\dagger}_{\mathbf{n}+\boldsymbol{\delta}_i,s} a_{\mathbf{n},s} \right). \tag{1.1}$$

In the above equation, $a_{\mathbf{n},s}$ and $b_{\mathbf{n}+\boldsymbol{\delta}_i,s}$ are the Fermi operators of electrons with spin s on A and B sublattices, respectively,

$$\boldsymbol{\delta}_1 = \frac{\mathbf{a}_1 - \mathbf{a}_2}{3}, \qquad \boldsymbol{\delta}_2 = \frac{\mathbf{a}_1 + 2\mathbf{a}_2}{3}, \qquad \boldsymbol{\delta}_3 = -\frac{2\mathbf{a}_1 + \mathbf{a}_2}{3} \tag{1.2}$$

are the three vectors connecting the NN sites and the lattice vectors generating each sublattice can be chosen as

$$\mathbf{a}_1 = \left(\frac{a}{2}, \frac{\sqrt{3}a}{2} \right), \qquad \mathbf{a}_2 = \left(\frac{a}{2}, -\frac{\sqrt{3}a}{2} \right), \tag{1.3}$$

where $a \simeq 0.246$ nm is the lattice constant.

$$H_0 = \sum_{s=\pm} \int_{\mathrm{BZ}} \frac{d^2\mathbf{k}}{(2\pi)^2} \begin{pmatrix} a^{\dagger}_s(\mathbf{k}) \\ b^{\dagger}_s(\mathbf{k}) \end{pmatrix}^{\mathsf{T}} \begin{pmatrix} 0 & \phi(\mathbf{k}) \\ \phi^*(\mathbf{k}) & 0 \end{pmatrix} \begin{pmatrix} a_s(\mathbf{k}) \\ b_s(\mathbf{k}) \end{pmatrix}, \tag{1.4}$$

where

$$\phi(\mathbf{k}) \equiv -t \sum_{i=1}^{3} e^{i\mathbf{k}\boldsymbol{\delta}_i} = -t \left[\exp\left(i\frac{k_y a}{\sqrt{3}} \right) + 2\cos\frac{k_x a}{2} \exp\left(-i\frac{k_y a}{2\sqrt{3}} \right) \right], \tag{1.5}$$

and the integration goes over the Brillouin zone (BZ). Diagonalization of (1.4) yields the energy spectrum

$$E_\pm(\mathbf{k}) = \pm|\phi(\mathbf{k})| = \pm t\sqrt{1 + 4\cos^2\left(\frac{k_x a}{2}\right) + 4\cos\left(\frac{k_x a}{2}\right)\cos\left(\frac{\sqrt{3}k_y a}{2}\right)}. \tag{1.6}$$

with two branches (Fig. 1.1). These branches touch at two independent points K_+ and K_- (often denoted also as K and K'). In the undoped graphene only one of two π-orbitals is filled, thus the lower branch is completely filled at zero temperature (valence band) and upper one is empty (conductance band). In the vicinity of these points (in the K_+ and K_- valleys), which can be taken as

$$\mathbf{K}_\pm = \left(\pm\frac{4\pi}{\sqrt{3}a}, 0\right), \tag{1.7}$$

one has

$$\phi(\mathbf{K}_\pm + \mathbf{q}) \simeq \hbar v_F(\pm q_x + iq_y), \qquad \mathbf{q} \to 0, \tag{1.8}$$

where $v_F = \sqrt{3}ta/(2\hbar) \simeq 10^6$ m/s is the Fermi velocity, and the Hamiltonian can be written as

$$H_0 = \sum_{s=\pm}\int_{\mathrm{DC}} \frac{d^2\mathbf{q}}{(2\pi)^2}\overline{\Psi}_s(\mathbf{q})\mathcal{H}_0^{\mathrm{D}}(\mathbf{q})\Psi_s(\mathbf{q}), \qquad \mathcal{H}_0^{\mathrm{D}}(\mathbf{q}) = \hbar v_F(\gamma^1 q_x + \gamma^2 q_y), \tag{1.9}$$

where and the integration goes over the Dirac cones (DC), $\Psi_s = (\Psi^s_{K_+}, \Psi^s_{K_-})^\top$,

$$\Psi^s_{K_+}(\mathbf{q}) = \begin{pmatrix}\Psi^s_{K_+A}(\mathbf{q})\\ \Psi^s_{K_-B}(\mathbf{q})\end{pmatrix} = \begin{pmatrix}a_s(\mathbf{K}_+ + \mathbf{q})\\ b_s(\mathbf{K}_+ + \mathbf{q})\end{pmatrix}, \qquad \Psi^s_{K_-}(\mathbf{q}) = \begin{pmatrix}\Psi^s_{K_-B}(\mathbf{q})\\ -\Psi^s_{K_-A}(\mathbf{q})\end{pmatrix} = \begin{pmatrix}b_s(\mathbf{K}_- + \mathbf{q})\\ -a_s(\mathbf{K}_- + \mathbf{q})\end{pmatrix}, \tag{1.10}$$

$\overline{\Psi}_\sigma \equiv \Psi^\dagger_\sigma(\mathbf{k})\gamma_0$ is the Dirac conjugated spinor, and the gamma matrices are defined as

$$\gamma^0 = \tilde{\tau}_3 \otimes \tau_3, \quad \gamma^1 = i\tilde{\tau}_3 \otimes \tau_2, \quad \gamma^2 = -i\tilde{\tau}_3 \otimes \tau_1, \quad \gamma^3 = i\tilde{\tau}_1 \otimes \tau_0, \quad \gamma^5 = -\tilde{\tau}_2 \otimes \tau_0. \tag{1.11}$$

Here σ_i, $\tilde{\tau}_i$, and τ_i, $i = 1, 2, 3$, are the Pauli matrices that act on the spin, valley, and sublattice components of the wave function, respectively (σ_0, $\tilde{\tau}_0$, and τ_0 are the unit matrices).

The existence of the Dirac points with the band touching and the linear spectrum is a consequence of the symmetry of graphene lattice. Therefore, this property is valid beyond the simple tight-binding model considered here. In particular, the next-to-nearest (NNN) hopping terms, while adding some electron-hole asymmetry, do no change the dispersion of electrons near the Dirac points considerably [14]. However, these terms can seriously affect the spectrum of edge

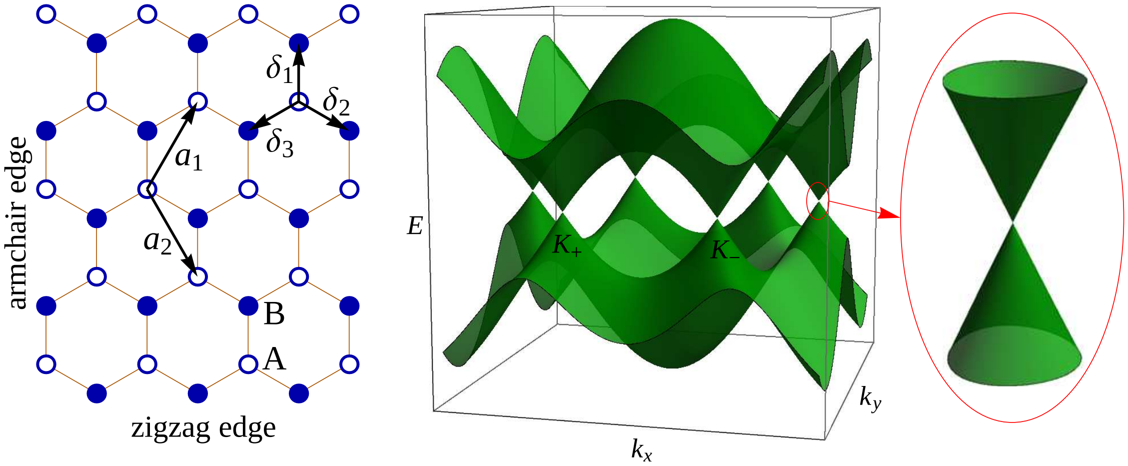

Figure 1.1: Crystal structure (left) and energy bands (right) of monolayer graphene.

states [15], which will be studied in detail in Chapter 3.

1.1.2 Bilayer graphene

In bilayer graphene with the Bernal stacking (Fig. 1.2), the A atoms of the top sublattice (A_2) are located directly above the B atoms of the bottom sublattice (B_1), and the interlayer interaction is dominated by the transitions between these sublattices. Neglecting all other interlayer hopping elements (the A_1B_2 hopping term leads to the trigonal warping of the bands, which becomes relevant only at very small energies), one arrives the following Hamiltonian in the momentum space:

$$H_0 = \sum_{s=\pm} \int_{\mathrm{BZ}} \frac{d^2\mathbf{k}}{(2\pi)^2} \begin{pmatrix} a^\dagger_{1s}(\mathbf{k}) \\ b^\dagger_{1s}(\mathbf{k}) \\ a^\dagger_{2s}(\mathbf{k}) \\ b^\dagger_{2s}(\mathbf{k}) \end{pmatrix}^{\mathsf{T}} \begin{pmatrix} 0 & \phi(\mathbf{k}) & 0 & 0 \\ \phi^*(\mathbf{k}) & 0 & \gamma_1 & 0 \\ 0 & \gamma_1 & 0 & \phi(\mathbf{k}) \\ 0 & 0 & \phi^*(\mathbf{k}) & 0 \end{pmatrix} \begin{pmatrix} a_{1s}(\mathbf{k}) \\ b_{1s}(\mathbf{k}) \\ a_{2s}(\mathbf{k}) \\ b_{2s}(\mathbf{k}) \end{pmatrix} \tag{1.12}$$

In the above equation, $a_{js}(\mathbf{k})$ and $b_{js}(\mathbf{k})$ are the Fourier transformed Fermi operators of electrons on a layer j with spin s on A and B sublattices, respectively. The energy spectrum has two pairs of electron-hole-symmetric bands (Fig. 1.2), one of which has higher energy ($|E| > \gamma_1$). The second pair exhibits band touching at the same K_+ and K_- points as in monolayer graphene, but the spectrum there is parabolic rather than linear. Expanding the Hamiltonian (1.12) in the

the $K_\pm$ valleys, one arrive at the effective Hamiltonian

$$H_0^{4\times4} = \sum_{s,\xi=\pm} \int \frac{d^2\mathbf{q}}{(2\pi)^2} \Psi_{K_\xi}^{s\dagger}(\mathbf{q}) \mathcal{H}_\xi^{4\times4}(\mathbf{q}) \Psi_{K_\xi}^{s}(\mathbf{q}), \tag{1.13}$$

where

$$\mathcal{H}_\xi^{4\times4}(\mathbf{q}) = \begin{pmatrix} 0 & \xi\hbar v_F(q_x - iq_y) & 0 & 0 \\ \xi\hbar v_F(q_x + iq_y) & 0 & \gamma_1 & 0 \\ 0 & \gamma_1 & 0 & \xi\hbar v_F(q_x - iq_y) \\ 0 & 0 & \xi\hbar v_F(q_x + iq_y) & 0 \end{pmatrix}, \tag{1.14}$$

and the wave function has four sublattice components for each spin $s = \pm$ and valley $\xi = \pm$,

$$\Psi_{K_+}^s(\mathbf{q}) = \begin{pmatrix} \Psi_{K_+A_1}^s(\mathbf{q}) \\ \Psi_{K_+B_1}^s(\mathbf{q}) \\ \Psi_{K_+A_2}^s(\mathbf{q}) \\ \Psi_{K_+B_2}^s(\mathbf{q}) \end{pmatrix} = \begin{pmatrix} a_{1s}(\mathbf{K}_+ + \mathbf{q}) \\ b_{1s}(\mathbf{K}_+ + \mathbf{q}) \\ a_{2s}(\mathbf{K}_+ + \mathbf{q}) \\ b_{2s}(\mathbf{K}_+ + \mathbf{q}) \end{pmatrix}, \quad \Psi_{K_-}^s(\mathbf{q}) = \begin{pmatrix} \Psi_{K_-B_2}^s(\mathbf{q}) \\ \Psi_{K_-A_2}^s(\mathbf{q}) \\ \Psi_{K_-B_1}^s(\mathbf{q}) \\ \Psi_{K_-A_1}^s(\mathbf{q}) \end{pmatrix} = \begin{pmatrix} b_{2s}(\mathbf{K}_- + \mathbf{q}) \\ a_{2s}(\mathbf{K}_- + \mathbf{q}) \\ b_{1s}(\mathbf{K}_- + \mathbf{q}) \\ a_{1s}(\mathbf{K}_- + \mathbf{q}) \end{pmatrix}. \tag{1.15}$$

In contrast to the monolayer case, in bilayer graphene a gap can be easily created by applying the external perpendicular electric field. The latter induces the additional term

$$\Delta \sum_{s,\xi=\pm} \xi \int \frac{d^2\mathbf{q}}{(2\pi)^2} \Psi_{K_\xi}^{s\dagger}(\mathbf{q}) \Psi_{K_\xi}^{s}(\mathbf{q}) \tag{1.16}$$

in the Hamiltonian, where 2Δ is the energy imbalance between the two layers. The Hamiltonian (1.13) will be used in Chapter 2 to study the edge states in bilayer graphene because it allows to impose the boundary conditions directly. However, the low-energy ($|E| \ll \gamma_1$) dynamics can be better understood from the simplified 2×2 model where the dimer atoms A_2 and B_1 are removed from consideration. The 2×2 Hamiltonian reads [12]:

$$H_0^{2\times2} = \sum_{s,\xi=\pm} \int \frac{d^2\mathbf{q}}{(2\pi)^2} \psi_{K_\xi}^{s\dagger}(\mathbf{q}) \mathcal{H}_\xi^{2\times2}(\mathbf{q}) \psi_{K_\xi}^{s}(\mathbf{q}), \tag{1.17}$$

Here

$$\psi_{K_+}^s = \begin{pmatrix} \Psi_{K_+A_1}^s \\ \Psi_{K_+B_2}^s \end{pmatrix}, \qquad \psi_{K_-}^s = \begin{pmatrix} \Psi_{K_-B_2}^s \\ \Psi_{K_-A_1}^s \end{pmatrix} \tag{1.18}$$

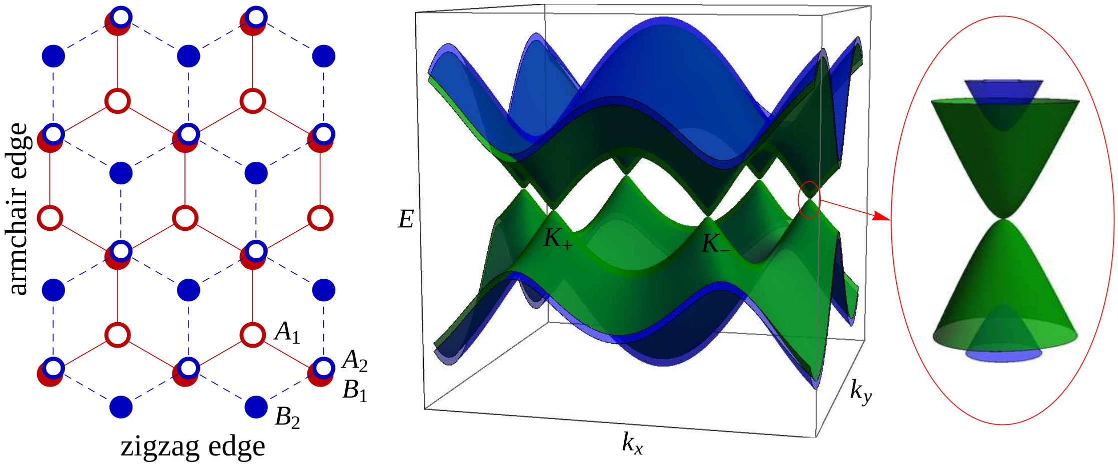

Figure 1.2: Crystal structure (left) and energy bands (right) of bilayer graphene.

and

$$\mathcal{H}_{\xi}^{2\times 2}(\mathbf{q}) = -\frac{1}{2m}\begin{pmatrix} 0 & (q_x - iq_y)^2 \\ (q_x + iq_y)^2 & 0 \end{pmatrix}, \tag{1.19}$$

where $m \equiv \gamma_1/2v_F^2$ is the effective mass of the quasiparticles.

1.2 Quantum Hall effect in graphene

The unusual quantization of the Hall conductivity $\sigma_{xy} = \nu e^2/h$ in monolayer graphene,

$$\nu = \pm 4\left(n + \frac{1}{2}\right), \quad n = 0, 1, 2, \ldots, \tag{1.20}$$

observed [6, 7] soon after the discovery of graphene, was the first compelling evidence of the Dirac nature of its charge carriers. In bilayer graphene, the integer quantum Hall effect with the filling factors

$$\nu = \pm 4n, \quad n = 0, 1, 2, \ldots, \tag{1.21}$$

also is the consequence of the peculiar sequence of Landau levels. The Hall plateaux reflect the fourfold degeneracy of LLs (and, in the bilayer case, the eightfold degeneracy of the LLL). This property is perfectly explained by the noninteracting theory [16, 17]. However, later experiments [18–25] with the cleaner graphene samples in stronger magnetic field detected the presence of integer Hall plateaux not described by Eqs. (1.20) and (1.21). The origin of the latter is the (quasi)spontaneous breaking of the U(4) symmetry due to the strong Coulomb interactions. This symmetry breaking has been described by the two theories. First theory, quantum Hall ferromagnetism [26–30], has been originally developed to describe the integer quantum Hall effect in multicomponent semiconductor systems [31–35]. It is based on projection on a given LL which is assumed to be split due to the exchange interactions. The second theory, magnetic catalysis [36–41], has been originally developed in relativistic theory where the gap formation becomes more favourable in the presence of the magnetic field due to enhanced density of states and the effective dimensional reduction [42–44]. Interestingly, both scenarios turned out to complement each other rather than compete and the order parameters proposed within each model were shown to necessarily coexist [45].

1.2.1 Dirac quasiparticles in a magnetic field

The external magnetic field $\mathbf{B} = \nabla \times \mathbf{A}$ is introduced in tight-binding Hamiltonian (1.1) of monolayer graphene by the Peierls substitution

$$c_i^\dagger c_j \to c_i^\dagger c_j \exp\left(\frac{ie}{\hbar c} \int_{\mathbf{r}_i}^{\mathbf{r}_j} d\mathbf{r} \cdot \mathbf{A}\right) \tag{1.22}$$

in the hopping terms corresponding to the transitions between the lattice sites $\mathbf{r}_i$ and $\mathbf{r}_j$. This leads (see e.g., [46]) to the following equation for two-dimensional Dirac fermions in magnetic field:

$$\left[i\gamma^0 \hbar \partial_t + i\hbar v_F \gamma^1 \left(\partial_x + \frac{ie}{\hbar c} A_x\right) + i\hbar v_F \gamma^2 \left(\partial_x + \frac{ie}{\hbar c} A_x\right)\right] \Psi_s(t, \mathbf{r}) = 0. \tag{1.23}$$

It has been solved in 1956 by McClure [3] who considered a single-layer graphene as a starting point for his calculations with graphite. The energy eigenvalues are Landau levels (Fig. 1.3)

$$E_{n\pm}^{s\xi} = \pm \epsilon_0 \sqrt{n}, \qquad n \geq 1, \tag{1.24}$$

$$E_0^{s\xi} = 0 \tag{1.25}$$

($\epsilon_0 = \sqrt{2}\hbar v_F / l$ is the Landau energy scale), which are not equidistant in a (pseudo)relativistic system. As a consequence of the U(4) spin-valley symmetry of the Hamiltonian, the energy eigenvalues are the same for both valleys ($\xi = \pm$) and spins ($s = \pm$). The corresponding wave functions in the gauge $\mathbf{A} = (-By, 0)$ are

$$\Psi_s(t, \mathbf{r}) = \sum_{s=\pm} \begin{pmatrix} C_{K_+}^s \Psi_{K_+}^s(t, \mathbf{r}) \\ C_{K_-}^s \Psi_{K_-}^s(t, \mathbf{r}) \end{pmatrix}, \tag{1.26}$$

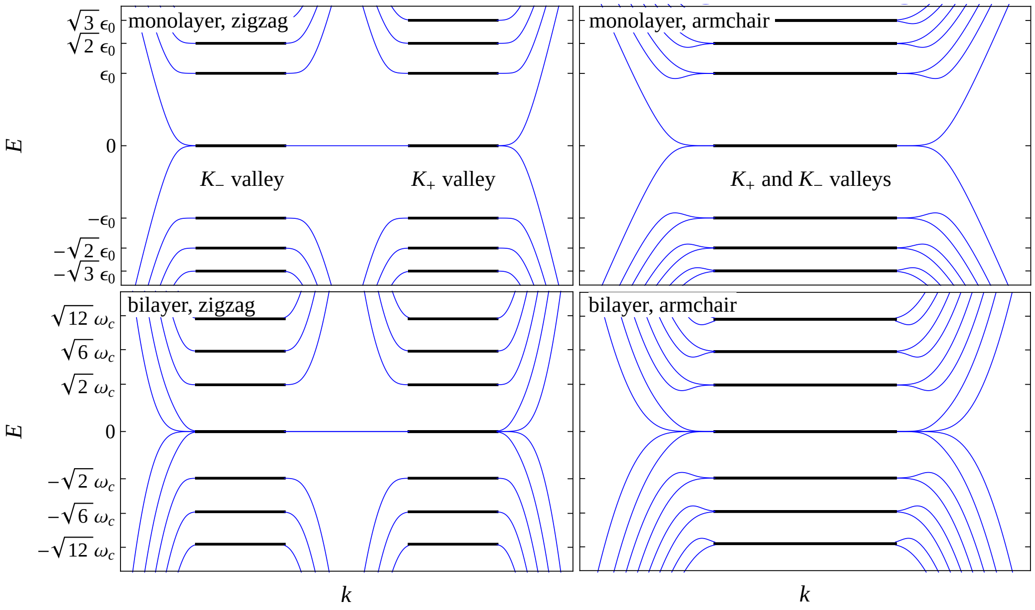

Figure 1.3: Energy spectra of free electrons (in the absence of LL splitting) in wide ($W \gg l$) monolayer (top panels) and bilayer (bottom panels) graphene ribbons with zigzag (left) and armchair (right) edges in a magnetic field. The thick lines schematically show the bulk LLs.

where $\Psi^s_{K_\pm}(t,\mathbf{r})$ are (unnormalized) solutions for each valley $K_\pm$,

$$\Psi^s_{K_\pm}(t,\mathbf{r}) = e^{-iE_n + ikx}\begin{pmatrix} \pm\varphi_{n-1}(\eta) \\ -\varphi_n(\eta) \end{pmatrix}, \tag{1.27}$$

where $\varphi(\eta) = 2^{-n/2}e^{-\eta^2/2}H_n(\eta)$ are the harmonic oscillator wave functions, $\eta = x/l - kl$ is the (shifted) dimensionless coordinate, and $H_n(x)$ are the Hermite polynomials. The lowest Landau level (LLL) with zero energy is peculiar: only the second component of the wave function (1.27) is nonzero, which means that electrons reside solely on A (B) sublattice in the K_- (K_+) valley.

Bilayer graphene in a magnetic field is described by the equation (for the 2×2 low-energy Hamiltonian)

$$\left\{ i\hbar\partial_t - \frac{1}{2m}\left[\tau_+(\hat{\pi}^\dagger)^2 + \tau_-\hat{\pi}^2\right]\right\}\Psi^s_{K_\xi}(t,\mathbf{r}) = 0, \tag{1.28}$$

where

$$\tau_\pm \equiv \tau_x \pm i\tau_y, \qquad \hat{\pi} \equiv \partial_x + i\partial_y + \frac{ie}{\hbar c}(A_x + iA_y). \tag{1.29}$$

It has the following energy solutions (Landau levels)

$$E^{s\xi}_{n\pm} = \pm\hbar\omega_c \sqrt{n(n-1)}, \qquad n \geq 2, \tag{1.30}$$

$$E^{s\xi}_0 = E^{s\xi}_1 = 0, \tag{1.31}$$

where $\omega_c = \epsilon_0^2/(\hbar\gamma_1)$ is the cyclotron frequency. The corresponding wave functions are

$$\Psi^s_{K_\pm}(t, \mathbf{r}) = e^{-iE_n+ikx} \begin{pmatrix} \pm\varphi_{n-2}(\eta) \\ -\varphi_n(\eta) \end{pmatrix}. \tag{1.32}$$

In the bilayer case, two Landau levels with $n = 0, 1$ have zero energy with the corresponding wave functions located on a single sublattice. Taking into account the spin, valley and the additional orbital ($n = 0, 1$) degeneracy, the LLL is eightfold degenerate.

1.2.2 Edge states

The wave functions (1.27), (1.32) are the plane waves in the x direction and localized near the “guiding center” $y = k/l^2$ in the y direction, with the localization length of the order of a magnetic length.In a ribbon geometry, the states residing far from the edges of the sample are bulk states, which are almost unperturbed infinite-plane solutions (1.27), (1.32). When the guiding center is close to the edge, the wave function has to be modified substantially in order to satisfy the boundary condition, which depends on the edge orientation, see Figs. 1.1 and 1.2. The energy spectrum is also modified for the states: normally the edge states acquire finite dispersion (with an exception of zigzag boundary dispersionless states located between the two valleys, see Fig. 1.3). Those of the dispersing edge states which are located at the Fermi level, carry the edge currents and play and important role in the creation of quantized off-diagonal conductance [47]. In graphene, there are electron-like edge state branches dispersing upwards and the hole-like branches dispersing downwards [48], see Fig. 1.3. The next two chapters are devoted to the important question whether the current-carrying edge states exist in a gap between the LLLs split either by external electric field (Chapter 2) or induced dynamically by the Coulomb interactions (Chapter 3).

1.3 Interactions and symmetry breaking in graphene

The LLL splitting that leads to the emergence of the new quantum Hall plateaus observed in high magnetic fields both in monolayer [18–21] and bilayer [22–25] graphene occurs mainly due to the strong long-range Coulomb interaction

$$H_C = \frac{1}{2}\sum_{s,s'=\pm}\int d^2\mathbf{r}d^2\mathbf{r}'\Psi^\dagger_s(\mathbf{r})\Psi_s(\mathbf{r})V(\mathbf{r}-\mathbf{r}')\Psi^\dagger_{s'}(\mathbf{r}')\Psi_{s'}(\mathbf{r}'), \tag{1.33}$$

where $V(\mathbf{r})$ is the screened Coulomb potential. If all other interactions were absent, this would be a spontaneous U(4) symmetry breaking. In a real situation, this symmetry is broken explicitly by the following smaller interaction terms:

- Zeeman interaction (in the presence of a magnetic field), which can be changed in a controlled way without modifying the Landau scale ϵ_0 by adding a longitudinal $\mathbf{B}$ component, i.e., by tilting the field;

- layer potential imbalance due to the external perpendicular electric field (in the bilayer case), also can be changed in a controlled way;

- asymmetric lattice-scale components of the Coulomb interactions and electron-phonon interactions: local four-fermion interaction terms with eight unknown coupling constants (two independent constants remain in a high magnetic field limit).

All of the above terms are much smaller then the U(4) symmetric part of the Coulomb interaction, mainly responsible for the gap creation. However, the interplay between these terms determines the quantum number of the filled and empty LLL sublevels at a given filling factor. The nature of the ground state can be identified experimentally by comparing the expected phase transitions with the properties of the given phase, such as a finite conductivity due to the presence of the gapless edge states.

Within the mean-field theory, different phases (ground states) are described by the specific symmetry breaking terms (order parameters). The term connected with the chemical potential,

$$\mu\sum_{s,\xi=\pm}\Psi^{s\dagger}_{K_\xi}\Psi^{s}_{K_\xi} = \mu\sum_{s,\xi=\pm}\left(\Psi^{s\dagger}_{K_\xi A}\Psi^{s}_{K_\xi A} + \Psi^{s\dagger}_{K_\xi B}\Psi^{s}_{K_\xi B}\right) \tag{1.34}$$

preserves the U(4) symmetry and does not create a gap. The symmetry is also preserved in the presence of a Haldane mass term

$$\Delta \sum_{s,\xi=\pm} \Psi^{s\dagger}_{K_\xi} \tau_3 \Psi^{s}_{K_\xi} = \Delta \sum_{s,\xi=\pm} \xi \left(\Psi^{s\dagger}_{K_\xi A} \Psi^{s}_{K_\xi A} - \Psi^{s\dagger}_{K_\xi B} \Psi^{s}_{K_\xi B} \right), \tag{1.35}$$

which breaks the time reversal symmetry and leads to the nonzero Hall conductivity even in the absence of a magnetic field [49]. It creates a band gap of 2Δ in the case $\mathbf{B} = 0$ but does not split the LLL at finite magnetic field. The U(4) symmetry-breaking terms can be introduced as the spin- and valley-dependent chemical potentials μ and Haldane masses Δ. For example, if μ has the opposite signs for the two spins, we obtain the ferromagnetic term

$$\mu_3 \sum_{s,\xi=\pm} s \Psi^{s\dagger}_{K_\xi} \Psi^{s}_{K_\xi} = \mu_3 \sum_{s,\xi=\pm} s \left(\Psi^{s\dagger}_{K_\xi A} \Psi^{s}_{K_\xi A} + \Psi^{s\dagger}_{K_\xi B} \Psi^{s}_{K_\xi B} \right). \tag{1.36}$$

Similarly, if Δ has the opposite signs for the two valleys, one gets the Dirac mass term that describes the density imbalance between the two sublattices (layers in the bilayer case),

$$\tilde{\Delta} \sum_{s,\xi=\pm} \xi \Psi^{s\dagger}_{K_\xi} \tau_3 \Psi^{s}_{K_\xi} = \tilde{\Delta} \sum_{s} \overline{\Psi}_s \Psi_s = \tilde{\Delta} \sum_{s,\xi=\pm} \left(\Psi^{s\dagger}_{K_\xi A} \Psi^{s}_{K_\xi A} - \Psi^{s\dagger}_{K_\xi B} \Psi^{s}_{K_\xi B} \right). \tag{1.37}$$

Combining the four-component spinors Ψ_s with the opposite spins $s = \pm$ into an eight-component wave function,

$$\Psi = \begin{pmatrix} \Psi_+ \\ \Psi_- \end{pmatrix}, \tag{1.38}$$

one can rewrite the free Hamiltonian of monolayer graphene as

$$H_0 = \hbar v_F \int d^2\mathbf{r}\, \Psi^\dagger(\mathbf{r}) \sigma_0 \otimes \tilde{\tau}_0 \otimes (\tau_1 \pi_x + \tau_2 \pi_y) \Psi(\mathbf{r}). \tag{1.39}$$

The general symmetry-breaking term in the mean-field theory has the form

$$\sum_{\alpha,\beta=0}^{3} \sigma_\alpha \otimes \tilde{\tau}_\beta \otimes (\mu_{\alpha\beta} \tau_0 + \Delta_{\alpha\beta} \tau_3) \tag{1.40}$$

(without the term $\alpha = \beta = 0$, which corresponds to the chemical potential μ and Haldane mass Δ). In Chapter 3, we calculate the energy spectrum of edge states for different symmetry-breaking terms (1.40) which describe the quantum Hall phases proposed in the literature. In Chapter 4, we find the dynamically generated terms (1.40) in bilayer graphene by solving the gap equation in the LLL approximation (when parameters $\mu_{\alpha\beta}$ and $\Delta_{\alpha\beta}$ become equivalent) for even filling factors.

Bibliography

[1] P. R. Wallace, Phys. Rev. **71**, 622 (1947).

[2] J. C. Slonczewski and P. R. Weiss, Phys. Rev. **109**, 272 (1958).

[3] J. W. McClure, Phys. Rev. **104**, 666 (1956).

[4] K. S. Novoselov, A. K. Geim, S. V. Morozov, D. Jiang, Y. Zhang, S. V. Dubonos, I. V. Grigorieva, and A. A. Firsov, Science **306**, 666 (2004).

[5] A. K. Geim, Science **324**, 1530 (2009).

[6] K. S. Novoselov, A. K. Geim, S. V. Morozov, D. Jiang, M. I. Katsnelson, I. V. Grigorieva, S. V. Dubonos, and A. A. Firsov, Nature **438**, 197 (2005).

[7] Y. Zhang, Y.-W. Tan, H. L. Stormer, and P. Kim, Nature **438**, 201 (2005).

[8] D. P. DiVincenzo and E. J. Mele, Phys. Rev. B **29**, 1685 (1984).

[9] G. W. Semenoff, Phys. Rev. Lett. **53**, 2449 (1984).

[10] M. Katsnelson and K. Novoselov, Solid State Commun. **143**, 3 (2007).

[11] K. S. Novoselov, E. McCann, S. V. Morozov, V. I. Fal'ko, M. I. Katsnelson, U. Zeitler, D. Jiang, F. Schedin, and A. K. Geim, Nat. Phys. **2**, 177 (2006).

[12] E. McCann and V. I. Fal'ko, Phys. Rev. Lett. **96**, 086805 (2006).

[13] T. Ohta, A. Bostwick, T. Seyller, K. Horn, and E. Rotenberg, Science **313**, 951 (2006).

[14] A. Kretinin, G. L. Yu, R. Jalil, Y. Cao, F. Withers, A. Mishchenko, M. I. Katsnelson, K. S. Novoselov, A. K. Geim, and F. Guinea, Phys. Rev. B **88**, 165427 (2013).

[15] K. Sasaki, S. Murakami, and R. Saito, Appl. Phys. Lett. **88**, 113110 (2006).

[16] V. P. Gusynin and S. G. Sharapov, Phys. Rev. Lett. **95**, 146801 (2005).

[17] N. M. R. Peres, F. Guinea, and A. H. Castro Neto, Phys. Rev. B **73**, 125411 (2006).

[18] Y. Zhang, Z. Jiang, J. P. Small, M. S. Purewal, Y.-W. Tan, M. Fazlollahi, J. D. Chudow, J. A. Jaszczak, H. L. Stormer, and P. Kim, Phys. Rev. Lett. **96**, 136806 (2006).

[19] Z. Jiang, Y. Zhang, H. L. Stormer, and P. Kim, Phys. Rev. Lett. **99**, 106802 (2007).

[20] X. Du, I. Skachko, F. Duerr, A. Luican, and E. Y. Andrei, Nature **462**, 192 (2009).

[21] K. I. Bolotin, F. Ghahari, M. D. Shulman, H. L. Stormer, and P. Kim, Nature **462**, 196 (2009).

[22] B. E. Feldman, J. Martin, and A. Yacoby, Nat. Phys. **5**, 889 (2009).

[23] Y. Zhao, P. Cadden-Zimansky, Z. Jiang, and P. Kim, Phys. Rev. Lett. **104**, 066801 (2010).

[24] R. T. Weitz, M. T. Allen, B. E. Feldman, J. Martin, and A. Yacoby, Science **330**, 812 (2010).

[25] J. Martin, B. E. Feldman, R. T. Weitz, M. T. Allen, and A. Yacoby, Phys. Rev. Lett. **105**, 256806 (2010).

[26] K. Nomura and A. H. MacDonald, Phys. Rev. Lett. **96**, 256602 (2006).

[27] K. Yang, S. Das Sarma, and A. H. MacDonald, Phys. Rev. B **74**, 075423 (2006).

[28] M. O. Goerbig, R. Moessner, and B. Douçot, Phys. Rev. B **74**, 161407 (2006).

[29] J. Alicea and M. P. A. Fisher, Phys. Rev. B **74**, 075422 (2006).

[30] L. Sheng, D. N. Sheng, F. D. M. Haldane, and L. Balents, Phys. Rev. Lett. **99**, 196802 (2007).

[31] K. Yang, K. Moon, L. Zheng, A. MacDonald, S. Girvin, D. Yoshioka, and S.-C. Zhang, Phys. Rev. Lett. **72**, 732 (1994).

[32] K. Moon, H. Mori, K. Yang, S. Girvin, A. MacDonald, L. Zheng, D. Yoshioka, and S.-C. Zhang, Phys. Rev. B **51**, 5138 (1995).

[33] K. Yang, K. Moon, L. Belkhir, H. Mori, S. Girvin, A. MacDonald, L. Zheng, and D. Yoshioka, Phys. Rev. B **54**, 11644 (1996).

[34] D. Arovas, A. Karlhede, and D. Lilliehöök, Phys. Rev. B **59**, 13147 (1999).

[35] Z. Ezawa and K. Hasebe, Phys. Rev. B **65**, 075311 (2002).

[36] D. V. Khveshchenko, Phys. Rev. Lett. **87**, 206401 (2001).

[37] E. V. Gorbar, V. P. Gusynin, V. A. Miransky, and I. A. Shovkovy, Phys. Rev. B **66**, 045108 (2002).

[38] V. P. Gusynin, V. A. Miransky, S. G. Sharapov, and I. A. Shovkovy, Phys. Rev. B **74**, 195429 (2006).

[39] I. F. Herbut, Phys. Rev. Lett. **97**, 146401 (2006).

[40] I. F. Herbut, Phys. Rev. B **75**, 165411 (2007).

[41] I. F. Herbut, Phys. Rev. B **76**, 085432 (2007).

[42] V. P. Gusynin, V. A. Miransky, and I. A. Shovkovy, Phys. Rev. Lett. **73**, 3499 (1994).

[43] V. P. Gusynin, V. A. Miransky, and I. A. Shovkovy, Phys. Rev. D **52**, 4718 (1995).

[44] V. Gusynin, V. Miransky, and I. Shovkovy, Nucl. Phys. B **462**, 249 (1996).

[45] E. V. Gorbar, V. P. Gusynin, V. A. Miransky, and I. A. Shovkovy, Phys. Rev. B **78**, 085437 (2008).

[46] V. P. Gusynin, S. G. Sharapov, and J. P. Carbotte, Int. J. Mod. Phys. B **21**, 4611 (2007).

[47] B. I. Halperin, Phys. Rev. B **25**, 2185 (1982).

[48] L. Brey and H. A. Fertig, Phys. Rev. B **73**, 195408 (2006).

[49] F. D. M. Haldane, Phys. Rev. Lett. **61**, 2015 (1988).

Chapter 2

Edge states in bilayer graphene in a magnetic field

2.1 Introduction

[1] Transport properties of a two-dimensional system can be significantly affected by the presence of edge states. These quasi-one-dimensional states, localized at the boundary of the sample, may provide the current-carrying channels even when the bulk excitations are gapped. In a magnetic field, edge states at the Fermi level give an important contribution to the Hall conductance of a two-dimensional electron gas [2].

Edge state spectrum in graphene, an atomically thin layer of carbon atoms arranged in a honeycomb crystalline lattice [3], depends on the type of the edge termination. There are two typical shapes of a graphene edge, *zigzag* and *armchair*. In addition to the quantum Hall edge states, zigzag edges of monolayer graphene support the dispersionless zero-energy edge states [4–6], present even without magnetic field [7, 8]. The spin splitting of the lowest Landau level results in the counterpropagating quantum Hall edge states with opposite spin polarization [6, 9, 10] at zero chemical potential ($\nu = 0$ state). In a more general case of the quantum Hall ferromagnetic order parameters [11–13] and the magnetic catalysis parameters (Dirac masses) [14–20], the existence of the gapless edge states depends both on the ratio of different order parameters and the edge type [21, 22].

Bilayer graphene consists of two AB (Bernal) stacked graphene monolayers. The spectrum gap in this system can be tuned by applying a gate voltage (bias) which creates the charge imbalance between the two layers [23, 24]. In the case of zigzag edges, in addition to the

---

[1] A version of this chapter has been published [1]

dispersionless modes similar to the ones that exist in monolayer graphene, there are also dispersive subgap edge excitations that carry counterpropagating currents in two valleys at a given edge [25–27]. In the presence of a perpendicular magnetic field, the charge imbalance between the two layers leads to the valley splitting of the zero-energy Landau levels which manifests itself in experiments as an extra $\nu = 0$ quantum Hall plateau [28]. The edge state structure in this regime in the case of zigzag edges has been studied both by the tight-binding method [28–31] and by the perturbation and variational methods within the continuum (Dirac) model [29]. The calculations of the edge state spectrum in bilayer graphene with armchair edges in a magnetic field have so far been limited to narrow samples where the Landau level formation occurs only at unrealistic field magnitudes [32]. The aim of the present chapter is to study the edge state spectrum of bilayer graphene ribbon or semi-infinite plane with zigzag or armchair edges in a magnetic field using the exact solutions to the differential equations of the continuum model, by combining analytic and numerical methods.

The low-energy edge state spectrum is found to be qualitatively different for the two edge types. In the case of zigzag edges, two zero-energy states per edge and spin are present at all accessible magnetic field values, which is consistent with previous findings [28–31]. Furthermore, one of these states is shown to be almost independent of a magnetic field strength, whereas the other one exhibits the partial hybridization with the bulk state $n = 1$. In contrast, in the case of armchair edges the spectrum is gapped and zero-energy states are absent.

The chapter is organized as follows. In Sec. 2.2 we introduce the four band continuum model for bilayer graphene in a magnetic field and present the general solution for the wave functions. The dispersion equations for edge states are derived and solved in Sec. 2.3 in the cases of zigzag edges and in Sec. 2.4 in the case of armchair edges. In Sec. 2.5 we give a brief summary of our results. Detailed derivations of the general solution and its different asymptotes are given in three appendixes.

2.2 General solution in the continuum model

2.2.1 Model

We consider bilayer graphene with Bernal stacking (Fig. 2.1), taking into account only the nearest-neighbor in-plane hopping $t \simeq 3\,\text{eV}$ and the interlayer A_2B_1 hopping $\gamma_1 \simeq 0.4\,\text{eV}$. We limit ourselves to the case of perfect zigzag or armchair edges, neglecting the effects of disorder and electron-electron interactions. The effective four band Hamiltonian for non-interacting

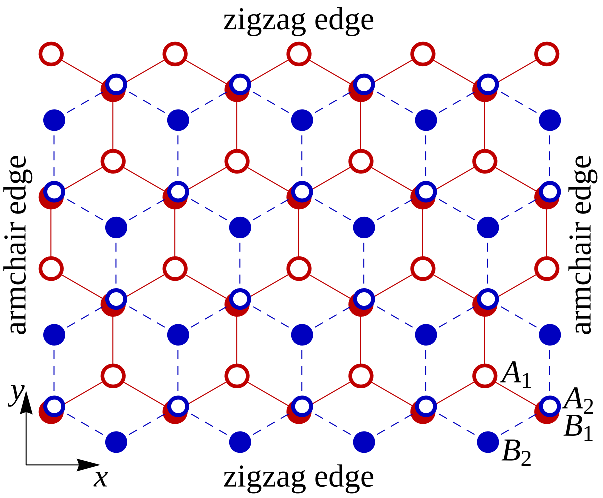

Figure 2.1: The lattice structure of bilayer graphene with zigzag and armchair edges.

electrons in each valley $K_{\xi=\pm}$ is [23]

$$H_\xi = \xi \begin{pmatrix} \Delta & v_F\hat{\pi}^\dagger & 0 & 0 \\ v_F\hat{\pi} & \Delta & \xi\gamma_1 & 0 \\ 0 & \xi\gamma_1 & -\Delta & v_F\hat{\pi}^\dagger \\ 0 & 0 & v_F\hat{\pi} & -\Delta \end{pmatrix}, \tag{2.1}$$

where $\hat{\pi} = \hat{p}_x + i\hat{p}_y$, $v_F = \sqrt{3}ta/(2\hbar) \simeq 10^6$ m/s is the Fermi velocity, $a \simeq 0.246$ nm is the lattice constant of graphene. The magnitude of the layer asymmetry gap parameter $\Delta = U/2$, where U is the interlayer potential induced by the applied perpendicular electric field, is bound by the relation $2|\Delta| < \gamma_1$ [33]. The external magnetic field $\mathbf{B} = \nabla \times \mathbf{A} = (0, 0, B)$ is perpendicular to the graphene plane (we assume $B > 0$), and the momentum operator is $\hat{\mathbf{p}} = -i\hbar\nabla + (e/c)\mathbf{A}$ with the electron charge $-e < 0$.

The Hamiltonian (2.1) acts on wave functions, the components of which correspond to different layers and sublattices. They are written in valleys K_+ and K_- as

$$\Psi^s_+ = \begin{pmatrix} \Psi^s_{+A_1} \\ \Psi^s_{+B_1} \\ \Psi^s_{+A_2} \\ \Psi^s_{+B_2} \end{pmatrix}, \qquad \Psi^s_- = \begin{pmatrix} \Psi^s_{-B_2} \\ \Psi^s_{-A_2} \\ \Psi^s_{-B_1} \\ \Psi^s_{-A_1} \end{pmatrix}, \tag{2.2}$$

where $s = \pm$ is the additional spin index.

2.2.2 General solution with x translational invariance

For edges along the x axis (this orientation corresponds to the zigzag edge type, see Fig. 2.1), it is suitable to use the Landau gauge $\mathbf{A} = (-By, 0)$. The wave functions are plane waves in the x direction,

$$\Psi_\xi^s(x, y) = e^{ikx}\Psi_\xi^s(y, k), \tag{2.3}$$

where the envelope functions $\Psi_\xi^s(y, k) \equiv \Psi_\xi^s(\eta)$ depend only on a single combination of the variables, $\eta = y/l - kl$, with $l = \sqrt{\hbar c/(eB)}$ being the magnetic length. They satisfy the equation

$$\xi \begin{pmatrix} \Delta & -\epsilon_0\hat{a} & 0 & 0 \\ -\epsilon_0\hat{a}^\dagger & \Delta & \xi\gamma_1 & 0 \\ 0 & \xi\gamma_1 & -\Delta & -\epsilon_0\hat{a} \\ 0 & 0 & -\epsilon_0\hat{a}^\dagger & -\Delta \end{pmatrix} \Psi_\xi^s(\eta) = E\Psi_\xi^s(\eta), \tag{2.4}$$

where $\hat{a} = 2^{-1/2}(\eta + \partial_\eta)$ and $\hat{a}^\dagger = 2^{-1/2}(\eta - \partial_\eta)$ are the annihilation and creation operators and $\epsilon_0 = \sqrt{2}\hbar v_F/l \simeq 36\sqrt{B[\mathrm{T}]}$ meV is the cyclotron energy in monolayer graphene.

The general solution of the system of differential equations (2.4) is the linear combination

$$\Psi_\xi^s(\eta) = \sum_{i=1}^{4} C_i^\xi \Phi_\xi^{(i)}(\eta) \tag{2.5}$$

of four independent functions (see Appendix 2.6 for details),

$$\begin{aligned} \Phi_\xi^{(1)}(\eta) &= f^\xi_{\lambda_1^\xi}(\eta), \\ \Phi_\xi^{(2)}(\eta) &= \frac{1}{\lambda_1^\xi - \lambda_2^\xi}\Big[f^\xi_{\lambda_1^\xi}(\eta) - f^\xi_{\lambda_2^\xi}(\eta)\Big], \\ \Phi_\xi^{(3)}(\eta) &= h^\xi_{\lambda_1^\xi}(\eta), \\ \Phi_\xi^{(4)}(\eta) &= \frac{1}{\lambda_1^\xi - \lambda_2^\xi}\Big[h^\xi_{\lambda_1^\xi}(\eta) - h^\xi_{\lambda_2^\xi}(\eta)\Big], \end{aligned} \tag{2.6}$$

where

$$\lambda_{1,2}^\xi = \frac{1}{2} + \frac{E^2 + \Delta^2}{\epsilon_0^2} \pm \frac{\sqrt{(\epsilon_0^2 - 4\xi\Delta E)^2 + 4\gamma_1^2(E^2 - \Delta^2)}}{2\epsilon_0^2}, \tag{2.7}$$

are two energy dependent dimensionless parameters (in general, complex) and the individual solutions $f^\xi_{\lambda_i^\xi}(\eta)$ and $h^\xi_{\lambda_i^\xi}(\eta)$ are written in terms of the parabolic cylinder functions $U(a, z)$ and

$V(a, z)$ [34],

$$f_\lambda^\pm(\eta) = \begin{pmatrix} \pm\nu_\pm(\lambda)U(\frac{3}{2}-\lambda,\ \sqrt{2}\eta) \\ \frac{(E\pm\Delta)^2-\epsilon_0^2\lambda}{\epsilon_0\gamma_1}U(\frac{1}{2}-\lambda,\ \sqrt{2}\eta) \\ \frac{E\pm\Delta}{\epsilon_0}U(\frac{1}{2}-\lambda,\ \sqrt{2}\eta) \\ \mp U(-\frac{1}{2}-\lambda,\ \sqrt{2}\eta) \end{pmatrix}, \tag{2.8}$$

$$h_\lambda^\pm(\eta) = \begin{pmatrix} \mp V(\frac{3}{2}-\lambda,\ \sqrt{2}\eta) \\ \frac{E\mp\Delta}{\epsilon_0}V(\frac{1}{2}-\lambda,\ \sqrt{2}\eta) \\ \frac{(E\mp\Delta)^2-\epsilon_0^2(\lambda-1)}{\epsilon_0\gamma_1}V(\frac{1}{2}-\lambda,\ \sqrt{2}\eta) \\ \pm\nu_\mp(\lambda-1)V(-\frac{1}{2}-\lambda,\ \sqrt{2}\eta) \end{pmatrix}, \tag{2.9}$$

with

$$\nu_\pm(\lambda) = \frac{(E\pm\Delta)(\gamma_1^2+\Delta^2-E^2)+(E\mp\Delta)\epsilon_0^2\lambda}{\epsilon_0^2\gamma_1}. \tag{2.10}$$

2.2.3 Bulk solutions

On an infinite plane, the normalizable wave functions contain only the parabolic cylinder functions $U(a, z)$ which are bound at $z \to \pm\infty$ provided that $a = -n - 1/2$, where n is a non-negative integer. In this case, the following relation is valid:

$$U\Big(-n-1/2,\ \sqrt{2}\eta\Big) = 2^{-\frac{n}{2}}e^{-\frac{\eta^2}{2}}H_n(\eta), \quad n = 0, 1, 2, \ldots, \tag{2.11}$$

where $H_n(z)$ are the Hermite polynomials. Therefore, there is a nontrivial bound solution proportional to $f_n^\xi(\eta)$ on an infinite plane when $\lambda_1^\xi = n$ or $\lambda_2^\xi = n$ with $n = 2, 3, 4, \ldots$. This condition is equivalent to the quartic equation for the energy of bulk Landau levels [35]

$$\Big[(E+\xi\Delta)^2 - n\epsilon_0^2\Big]\Big[(E-\xi\Delta)^2 - (n-1)\epsilon_0^2\Big] - \gamma_1^2(E^2-\Delta^2) = 0. \tag{2.12}$$

For each $\xi = \pm$ and $n = 2, 3, 4, \ldots$, it has four solutions $E_{\pm n}^{\kappa,\xi}$, where $\kappa = +(-)$ corresponds to the high (low) energy band. All high-energy band Landau levels have energies satisfying $(E_{\pm n}^{+,\xi})^2 > \gamma_1^2 + \Delta^2$.

As seen from Eq. (2.8), at $\lambda_i^\xi = 1$ the solution proportional to $f_1^\xi(\eta)$ is normalizable on an infinite plane provided that $\nu_\xi(1) = 0$. Therefore, in addition to the solutions of Eq. (2.12), there are two more high-energy levels $E_{\pm 1}^{+,\xi}$ and one low-energy level $E_1^{-,\xi}$, given by the roots of the cubic equation

$$(E+\xi\Delta)(\gamma_1^2+\Delta^2-E^2) + (E-\xi\Delta)\epsilon_0^2 = 0. \tag{2.13}$$

Finally, in the case $\lambda_i^\xi = 0$ there is a valid solution proportional to $f_0^\xi(\eta)$ on an infinite plane provided that $v_\xi(0) = 0$ and $E + \xi\Delta = 0$, which yields the remaining low-energy level

$$E_0^{-,\xi} = -\xi\Delta. \tag{2.14}$$

The corresponding bulk wave functions are [35, 36]

$$\Psi_\xi^s(\eta) = C_1^\xi f_n^\xi(\eta) = C_1^\xi 2^{\frac{2-n}{2}} e^{-\frac{\eta^2}{2}} \begin{pmatrix} \frac{(n-1)[n\epsilon_0^2 - (E_{\pm n}^{\kappa,\xi} + \xi\Delta)^2]}{\gamma_1(\xi E_{\pm n}^{\kappa,\xi} - \Delta)} H_{n-2}(\eta) \\ \frac{(E_{\pm n}^{\kappa,\xi} + \xi\Delta)^2 - n\epsilon_0^2}{\sqrt{2}\epsilon_0\gamma_1} H_{n-1}(\eta) \\ \frac{E_{\pm n}^{\kappa,\xi} + \xi\Delta}{\sqrt{2}\epsilon_0} H_{n-1}(\eta) \\ -\frac{\xi}{2} H_n(\eta) \end{pmatrix}. \tag{2.15}$$

In the case of unbiased bilayer graphene ($\Delta = 0$), the Landau level energies are equal in both valleys $K_\pm$ and are given by expression [35]

$$E_{\pm n}^{\kappa,\xi} = \pm\frac{1}{\sqrt{2}}\left(\left|\gamma_1^2 + (2n-1)\epsilon_0^2\right| + \kappa\sqrt{(\gamma_1^2 - \epsilon_0^2)^2 + 4n\gamma_1^2\epsilon_0^2}\right)^{1/2}. \tag{2.16}$$

Finite Δ causes the valley splitting of Landau levels as well as the splitting between levels $n = 0$ and $n = 1$ [36].

In the case $\gamma_1 \gg \epsilon_0 \gg |\Delta|$, the low-energy Landau levels are approximately given by the two band effective model [23]

$$E_{\pm n}^{-,\xi} \simeq \pm\sqrt{\hbar^2\omega_c^2 n(n-1) + \Delta^2}, \quad n = 2, 3, 4, \ldots, \tag{2.17}$$

$$E_1^{-,\xi} \simeq E_0^{-,\xi} = -\xi\Delta, \tag{2.18}$$

where ω_c is the cyclotron frequency in bilayer graphene, $\hbar\omega_c = \epsilon_0^2/\gamma_1 \simeq 3.2B[\mathrm{T}]$ meV.

2.3 Zigzag edges

2.3.1 Dispersion equations for half-plane

On a semi-infinite plane $y > 0$, the normalizable wave functions are given in terms of only $U(a, z)$ function, which decreases exponentially as $z \to \infty$, while the function $V(a, z)$ grows exponentially in both directions $z \to \pm\infty$. Therefore, $C_3^\xi = C_4^\xi = 0$ and the solution is

$$\Psi_\xi^s(\eta) = C_1^\xi \Phi_\xi^{(1)}(\eta) + C_2^\xi \Phi_\xi^{(2)}(\eta). \tag{2.19}$$

In the limit $\Delta \to 0$, this solution reduces to the one used in Ref. [37] in the description of interface states on the monolayer-bilayer graphene junction.

The boundary conditions at the zigzag edge $y = 0$ of the half-plane (which corresponds to $\eta = -kl$) are [29]

$$\Psi_{\xi A_i}^s(-kl) = 0, \qquad i = 1,2, \tag{2.20}$$

i.e., the wave functions on A atoms should vanish at the edge on both layers. These boundary conditions do not mix the components of the wave functions from different valleys ($\xi = \pm$) and lead to the following system of 2 equations for each valley K_ξ:

$$C_1^\xi \Phi_{\xi A_i}^{(1)}(-kl) + C_2^\xi \Phi_{\xi A_i}^{(2)}(-kl) = 0, \qquad i = 1,2, \tag{2.21}$$

where the layer and sublattice components of $\Phi_\xi^{(j)}$, f_λ^ξ and h_λ^ξ are chosen in the same way as the components of Ψ_ξ^s in Eq. (2.2). These systems have nontrivial solutions when the corresponding determinants of the coefficient functions are zero, i.e.,

$$\det\begin{pmatrix} \Phi_{\xi A_1}^{(1)}(-kl) & \Phi_{\xi A_1}^{(2)}(-kl) \\ \Phi_{\xi A_2}^{(1)}(-kl) & \Phi_{\xi A_2}^{(2)}(-kl) \end{pmatrix} = 0, \tag{2.22}$$

which is equivalent to

$$\frac{1}{\lambda_2^\xi - \lambda_1^\xi} \det\begin{pmatrix} f_{\lambda_1^\xi}^{\xi A_1}(-kl) & f_{\lambda_2^\xi}^{\xi A_1}(-kl) \\ f_{\lambda_1^\xi}^{\xi A_2}(-kl) & f_{\lambda_2^\xi}^{\xi A_2}(-kl) \end{pmatrix} = 0. \tag{2.23}$$

Writing the components of $f_{\lambda_i^\xi}^\xi(-kl)$ explicitly, one arrives at the dispersion equation for the K_+ valley,

$$\frac{E+\Delta}{\lambda_2^+ - \lambda_1^+}\left\{ \nu_+(\lambda_1^+) U\Big(\frac{3}{2} - \lambda_1^+, -\sqrt{2}kl\Big) U\Big(\frac{1}{2} - \lambda_2^+, -\sqrt{2}kl\Big) - (\lambda_1^+ \leftrightarrow \lambda_2^+) \right\} = 0, \tag{2.24}$$

and the K_- valley,

$$\frac{1}{\lambda_2^- - \lambda_1^-}\left\{ \left[(E-\Delta)^2 - \epsilon_0^2 \lambda_1^-\right] U\Big(\frac{1}{2} - \lambda_1^-, -\sqrt{2}kl\Big) U\Big(-\frac{1}{2} - \lambda_2^-, -\sqrt{2}kl\Big) - (\lambda_1^- \leftrightarrow \lambda_2^-) \right\} = 0. \tag{2.25}$$

2.3.2 Dispersion equations for ribbon

The boundary conditions at two ribbon edges $y = 0$ and $y = W$ (corresponding to $\eta = -kl$ and $\eta = W/l - kl$, respectively) are [29]

$$\psi^s_{\xi A_i}(-kl) = \Psi^s_{\xi B_i}(W/l - kl) = 0, \qquad i = 1, 2, \tag{2.26}$$

i.e., in addition to the condition (2.20) at the edge $y = 0$, the components $B_{1,2}$ must vanish at the opposite edge. These boundary conditions also do not mix valleys and imply the following independent system of 4 equations for each valley:

$$\begin{aligned} &\textstyle\sum_{j=1}^4 C^\xi_j \Phi^{(j)}_{\xi A_i}(-kl) = 0, \\ &\textstyle\sum_{j=1}^4 C^\xi_j \Phi^{(j)}_{\xi B_i}(W/l - kl) = 0, \qquad i = 1, 2. \end{aligned} \tag{2.27}$$

These systems have nontrivial solutions when the corresponding determinants of coefficient functions are zero. After some straightforward algebra, we obtain the dispersion equation for the K_+ valley,

$$\frac{1}{(\lambda^+_2 - \lambda^+_1)^2} \det \begin{pmatrix} X^+_1(-kl) & Y^+_1(W/l - kl) \\ X^+_2(-kl) & Y^+_2(W/l - kl) \end{pmatrix} = 0, \tag{2.28}$$

and the K_- valley,

$$\frac{1}{(\lambda^-_2 - \lambda^-_1)^2} \det \begin{pmatrix} X^-_1(W/l - kl) & Y^-_1(-kl) \\ X^-_2(W/l - kl) & Y^-_2(-kl) \end{pmatrix} = 0, \tag{2.29}$$

where the 2×2 blocks $X^\pm_i(\eta)$ and $Y^\pm_i(\eta)$ are defined as

$$X^\pm_i(\eta) = \begin{pmatrix} \nu_\pm(\lambda^\pm_i) U(\frac{3}{2} - \lambda^\pm_i,\, \sqrt{2}\eta) & \frac{E\pm\Delta}{\epsilon_0} U(\frac{1}{2} - \lambda^\pm_i,\, \sqrt{2}\eta) \\ -V(\frac{3}{2} - \lambda^\pm_i,\, \sqrt{2}\eta) & \frac{(E\mp\Delta)^2 - \epsilon_0^2(\lambda^\pm_i - 1)}{\epsilon_0\gamma_1} V(\frac{1}{2} - \lambda^\pm_i,\, \sqrt{2}\eta) \end{pmatrix}, \tag{2.30}$$

$$Y^\pm_i(\eta) = \begin{pmatrix} -U(-\frac{1}{2} - \lambda^\pm_i,\, \sqrt{2}\eta) & \frac{(E\pm\Delta)^2 - \epsilon_0^2\lambda^\pm_i}{\epsilon_0\gamma_1} U(\frac{1}{2} - \lambda^\pm_i,\, \sqrt{2}\eta) \\ \nu_\mp(\lambda^\pm_i - 1) V(-\frac{1}{2} - \lambda^\pm_i,\, \sqrt{2}\eta) & \frac{E\mp\Delta}{\epsilon_0} V(\frac{1}{2} - \lambda^\pm_i,\, \sqrt{2}\eta) \end{pmatrix}. \tag{2.31}$$

Using the expressions for $U(a, z)$ and $V(a, z)$ in terms of the parabolic cylinder function $D_\lambda(z)$,

$$U\left(-\frac{1}{2} - \lambda, z\right) = D_\lambda(z), \tag{2.32}$$

$$V\left(-\frac{1}{2} - \lambda, z\right) = \frac{\Gamma(-\lambda)}{\pi}[D_\lambda(-z) - \cos(\pi\lambda) D_\lambda(z)], \tag{2.33}$$

one can show the following symmetry property of the determinants in Eqs. (2.28)–(2.29):

$$\det\begin{pmatrix} X_1^{\xi}(\eta_1) & Y_1^{\xi}(\eta_2) \\ X_2^{\xi}(\eta_1) & Y_2^{\xi}(\eta_2) \end{pmatrix} = \det\begin{pmatrix} X_1^{\xi}(-\eta_1) & Y_1^{\xi}(-\eta_2) \\ X_2^{\xi}(-\eta_1) & Y_2^{\xi}(-\eta_2) \end{pmatrix}. \tag{2.34}$$

It implies that the energy spectra in two valleys are related by

$$E^{\xi}(k) = -E^{-\xi}(W/l^2 - k) \tag{2.35}$$

(note that the momenta in each valley are measured from the corresponding K points). The corresponding wave functions are related by

$$\Psi_{\xi}^{s}(y,k) = C\begin{pmatrix} \sigma_3 & 0 \\ 0 & \sigma_3 \end{pmatrix}\Psi_{-\xi}^{s}(W-y, W/l^2 - k), \tag{2.36}$$

where σ_3 is the Pauli matrix.

2.3.3 Results for the spectra

We numerically solve dispersion equations (2.24)–(2.25) in the case of the semi-infinite plane and Eqs. (2.28)–(2.29) in the case of the finite width ribbon. The solutions include both low energy band ($\kappa = -1$) and high energy band ($\kappa = +1$) spectrum branches. In what follows, we limit our consideration to energies lower than γ_1 and focus only on the low energy branches. It is also assumed that $\Delta \geq 0$, taking into account that in the zigzag edge case the change of the sign of Δ results in merely the inversion $E \to -E$ of the spectrum.

First, we consider the case $2\Delta < \epsilon_0$ when $n = 1$ and $n = 2$ are the two Landau levels with the lowest energies. Our results are consistent with those obtained previously in the tight-binding studies [28–31]. The examples of the spectra showing a few lower Landau levels in the case of a half-plane and two different widths of the ribbon are shown in Fig. 2.2. On a half-plane, the spectrum branches at $kl \gg 1$ asymptotically approach the bulk Landau levels given by Eqs. (2.12)–(2.14). The states corresponding to these asymptotes (plateaus) are approximately described by infinite plane solutions (2.15) with $\eta = y/l - kl$. They are localized in the bulk and centered along the y direction at $y_k = kl^2$ (the position wave-vector duality in Landau gauge). The same is true for wide ribbons $W \gg l$ [see Fig. 2.2 (b)], where the plateaus closely approaching the bulk Landau levels are formed. For a given branch, all states to the left (right) of the bulk plateau are localized in the vicinity of the edges $y = 0$ ($y = W$). There are also two purely edge state branches in each valley, which do not correspond to any of the bulk Landau

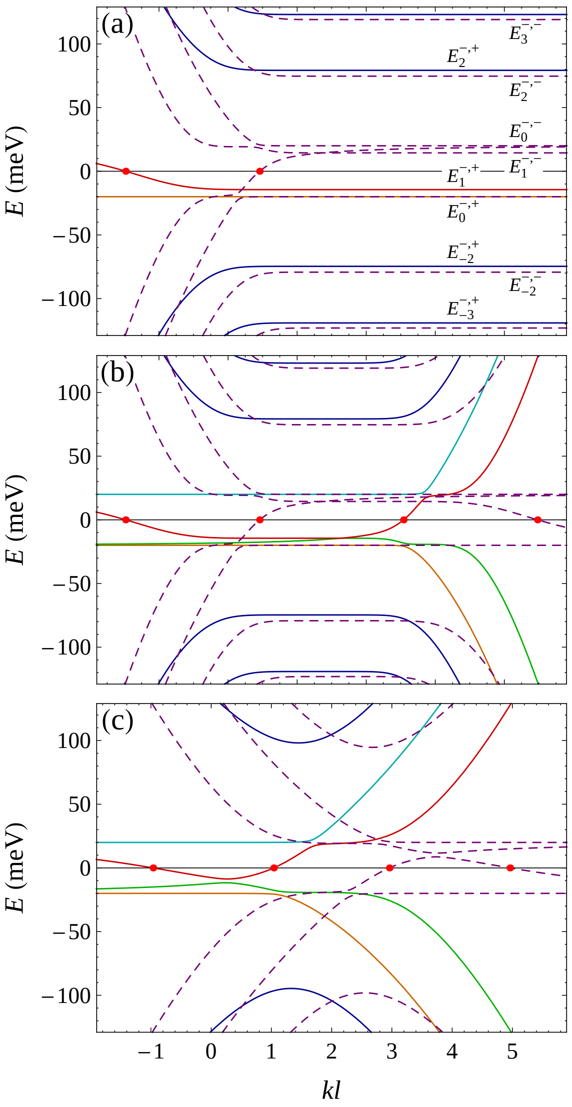

Figure 2.2: Numerical results for the low-energy spectrum in bilayer graphene with zigzag edge(s) at $B = 20\,\mathrm{T}$ and $\Delta = 20\,\mathrm{meV}$: (a) half-plane, (b) ribbon of the width $W = 10l$, (c) ribbon of the width $W = 4l$. Solid (dashed) lines represent the spectrum in the K_+ (K_-) valley. On panel (a), the bulk Landau level energies $E_n^{\kappa,\xi}$ are indicated. Gapless edge states at $\mu_s = 0$ are marked by dots.

levels. The states on these branches, as well as the edge states corresponding to the levels $n = 0, 1$, remain present even at $B = 0$. As we will see below, the main effect of magnetic field on these edge state modes is the relative horizontal shift $\delta k = W/l^2$ between the states on the opposite edges.

The width of a given bulk plateau is determined by the range of y_k for which the corresponding bulk wave function (2.15) remains almost unperturbed by the edges. Due to the increase of the localization length of the bulk state with increasing $|n|$, the widths of the higher bulk Landau level plateaus are smaller. In the case of a narrow ribbon, shown in Fig. 2.2 (c) the bulk Landau level plateaus are not formed.

In the following, we consider only the spectrum in the K_+ valley, taking into account that the energies and the wave functions in the two valleys are related by Eqs. (2.35) and (2.36). The structure of the spectrum at the energy scale $|E| \lesssim \Delta$ is shown in Fig. 2.3 for different values of a magnetic field and Δ, and the properties of the corresponding states are given in Fig. 2.4. This low-energy spectrum consists of the four branches and is complicated by their avoided crossings. For the moment, we ignore the level splittings at these anticrossings and briefly describe the eigenstates corresponding to each branch. We assume that the ribbon is wide enough ($W/l \gg 1$) so that the plateaus corresponding to bulk states $n = 0$ and $n = 1$ are formed, and in the middle of these plateaus the effects of the edges on the bulk wave functions can be neglected.

The wave function (2.15) of the $n = 0$ bulk Landau level resides solely on a single layer and sublattice B_2 with

$$\Psi^s_{+B_2}(y, k) = (\sqrt{\pi}l)^{-1/2} e^{-(y-y_k)^2/2l^2}, \tag{2.37}$$

and is not perturbed by the left edge ($y = 0$) of the ribbon. The only effect of this edge on the wave function is that it becomes zero outside the ribbon and the normalization constant in Eq. (2.37) changes accordingly. When the momentum becomes negative and the guiding center y_k moves further away from the ribbon, the bulk Landau level $n = 0$ evolves into a dispersionless branch of strongly localized near the left edge states residing on a single sublattice and layer B_2 with the same energy $E = -\Delta$ and described by the wave function

$$\Psi^s_{+B_2}(y, k) = Ce^{-|k|y-y^2/2l^2} \simeq Ce^{-|k|y}, \tag{2.38}$$

where C is a normalization constant. On a half-plane, these states correspond to the exact solution $E = -\Delta$ of dispersion equation (2.24).

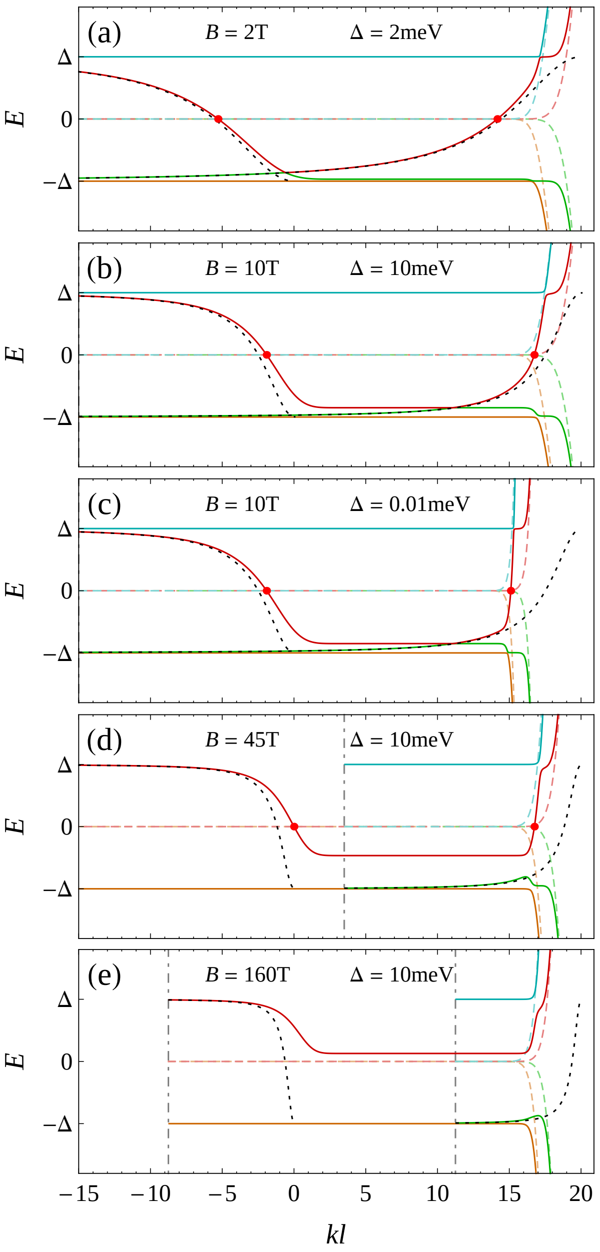

Figure 2.3: Numerical results for the lowest spectrum branches in the K_+ valley for zigzag ribbon of a width $W = 20l$ at different values of magnetic field and gap parameter $\Delta \ll \epsilon_0$. Dashed lines correspond to the unbiased case ($\Delta = 0$), and dotted lines show the subgap edge modes at $B = 0$ (right edge mode is shifted horizontally with $k \to k + W/l^2$ in order to illustrate the effect of a magnetic field). Dot-dashed vertical lines display the cutoffs for the edge modes. Gapless edge states at $\mu_s = 0$ are marked by dots.

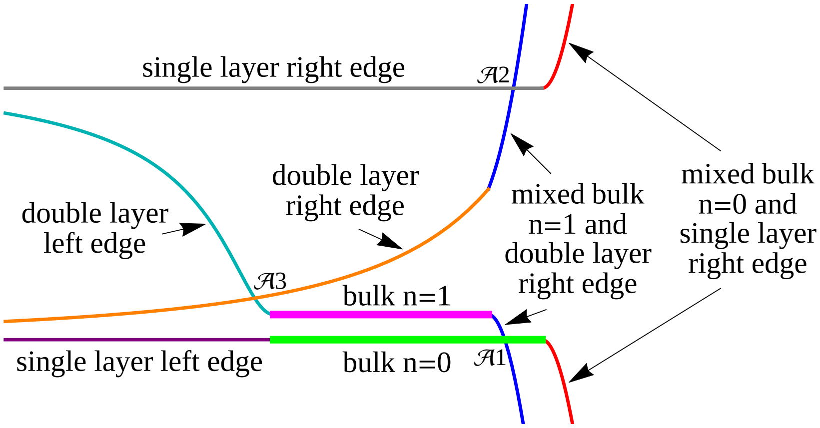

Figure 2.4: Schematic illustration of the spectrum branches with the lowest energy in the K_+ valley for wide zigzag ribbon ($W \gg l$) at small gap parameter and moderate magnetic field ($\Delta \ll \epsilon_0 \ll \gamma_1$), indicating the properties of the corresponding states. Level splittings at avoided crossings $\mathcal{A}1$, $\mathcal{A}2$, $\mathcal{A}3$ of the branches are removed for clarity. Bulk Landau levels are shown by thick lines.

The wave function (2.15) of the $n = 1$ bulk Landau level has three nonzero components,

$$\Psi_+^s(y,k) = Ce^{-(y-y_k)^2/2l^2} \begin{pmatrix} 0 \\ \frac{\epsilon_0^2-(E_1^{-,+}+\Delta)^2}{\sqrt{2}\epsilon_0\gamma_1} \\ -\frac{E_1^{-,+}+\Delta}{\sqrt{2}\epsilon_0} \\ (y-y_k)/l \end{pmatrix}. \tag{2.39}$$

This level disperses upwards when the guiding center y_k approaches the left edge, and its energy grows gradually from $E_1^{-,+}$ to Δ. This behavior has been qualitatively described in Ref. [29] by the variational method, using the "bulklike" anzatz $\Psi_{+A_1}^s(y,k) \equiv 0$. Here, by using the properties of the parabolic cylinder functions, we find the exact asymptotic behavior of this branch at large positive and negative momenta (see Appendix 2.7). For $kl \gg 1$, the deviation from the bulk energy $E_1^{-,+}$ is exponentially small and given by Eq. (2.93), whereas at $-kl \gg 1$ the energy has the following asymptotic behavior:

$$E \simeq \Delta\left(1 - \frac{\gamma_1^2}{2\hbar^2 v_F^2 k^2}\right), \tag{2.40}$$

and the corresponding wave function of the resulting edge mode is approximately given by

$$\Psi_+^s(y,k) \simeq C e^{-|k|y} \begin{pmatrix} -\frac{\Delta\gamma_1 y}{\hbar^2 v_F^2 k} \\ \frac{2\hbar v_F k}{\gamma_1} \\ \frac{2\Delta y}{\hbar v_F} \\ 1+2ky \end{pmatrix}. \tag{2.41}$$

In contrast to the *single layer* left edge dispersionless mode (2.38), this solution has nonzero components corresponding to both graphene layers, and thus will be referred to as a *double layer* left edge mode.

For a ribbon of a finite width W, there are two more low-energy solutions of the dispersion equations, which are absent in the case of a half-plane and correspond to the modes localized near the right edge ($y = W$) of the ribbon. One of them forms horizontal plateau with energy $E = \Delta$, which does not correspond to any of the bulk Landau levels. This mode is described by the wave function

$$\Psi_+^s(y,k) \simeq C e^{-\frac{\eta^2}{2}} \begin{pmatrix} \frac{\sqrt{2\pi}\Delta\gamma_1}{\epsilon_0^2} e^{\eta^2}\,\mathrm{erfc}(-\eta) \\ \frac{\epsilon_0^2-4\Delta^2}{\gamma_1\epsilon_0} \\ -\frac{2\Delta}{\epsilon_0} \\ \sqrt{2}\eta \end{pmatrix}, \tag{2.42}$$

where $\eta = y/l - kl$ and

$$\mathrm{erfc}(x) = 1 - \frac{2}{\sqrt{\pi}} \int_0^x dt\, e^{t^2} \tag{2.43}$$

is the complementary error function. The boundary condition $\Psi^s_{+B_{1,2}}(W,k) = 0$ does not perturb this state noticeably because all its components, except $\Psi^s_{+A_1}$, are localized in the bulk near $y = y_k$. At $kl - W/l \ll -1$ these bulklike components are negligibly small compared to $\Psi^s_{+A_1}(y,k)$, and the normalized wave function (2.42) is approximately given by

$$\Psi_+^s(y,k) \simeq \sqrt{2|k'|} e^{-|k'|(W-y)} \begin{pmatrix} 1 \\ 0 \\ 0 \\ 0 \end{pmatrix}, \qquad k' \equiv k - \frac{W}{l^2}. \tag{2.44}$$

As one can see, this *single layer* state is localized near the right edge even when the guiding center y_k is deep in the bulk, hence the position wave-vector duality is not applicable in this case. This purely edge state branch is completely analogous to the one that exists in gapped monolayer graphene [22].

The energy of another right edge mode changes from $+\Delta$ to $-\Delta$ as y_k moves into the bulk. At $-k'l \gg 1$ it is described by the asymptote (see Appendix 2.7)

$$E \simeq \Delta\left(1 - \frac{\gamma_1^2}{2\hbar^2 v_F^2 k'^2}\right), \tag{2.45}$$

and the corresponding wave function is approximately given by

$$\Psi_+^s(y,k) \simeq C e^{-|k'|(W-y)} \begin{pmatrix} 1 + 2k'(W-y) \\ -\frac{2\Delta(W-y)}{\hbar v_F} \\ \frac{2\hbar v_F k'}{\gamma_1} \\ \frac{\Delta\gamma_1(W-y)}{\hbar^2 v_F^2 k'} \end{pmatrix}. \tag{2.46}$$

The position wave-vector duality is not applicable for this *double layer* right edge mode mode as well.

In unbiased ($\Delta = 0$) bilayer graphene, the spectrum is electron-hole symmetric, with the positive and negative energy solutions related by

$$\Psi_\xi^s(y,k,E) = C \begin{pmatrix} \sigma_3 & 0 \\ 0 & \sigma_3 \end{pmatrix} \Psi_\xi^s(y,k,-E). \tag{2.47}$$

The orthogonality of those states implies that the probabilities of finding the electron on each sublattice are equal,

$$\int_0^W dy\left(\left|\Psi_{\xi A_1}^s\right|^2 + \left|\Psi_{\xi A_2}^s\right|^2\right) = \int_0^W dy\left(\left|\Psi_{\xi B_1}^s\right|^2 + \left|\Psi_{\xi B_2}^s\right|^2\right) = \frac{1}{2}. \tag{2.48}$$

At $\Delta = 0$ in the K_+ valley, the bulk states $n = 0$ and $n = 1$ with zero energy reside solely on the B sublattice, while the edge states (2.44) and (2.46) reside on the A sublattice. Therefore, in the range of momenta where the bulk $n = 0, 1$ solutions are present, these bulk states are hybridized with the right edge states, so that the probabilities to find the electron in the bulk and at the right edge are equal. Similar mixing of the bulk and edge states occurs in gapless monolayer graphene with zigzag edges [5, 10, 38]. In Appendix 2.7 we show that when y_k is deep in the bulk ($-k'l \gg 1$), the bulk $n = 0$ ($n = 1$) states admix mainly with the single (double) layer right edge states and also find the dispersion of these mixed bulk-edge modes.

At finite Δ, the spectrum of the lowest energy branches for y_k located near the right edge of the ribbon is characterized by a transition from the distinct bulk and edge branches at $-k'l \gg 1$

to the mixed bulk-edge modes on the energy scales $\Delta \ll |E| \ll \epsilon_0$. At $-k'l \gg 1$, the deviations of the $n = 0$ and $n = 1$ level energies from their bulk values are exponentially small, see Eqs. (2.95) and (2.96). When y_k moves towards the right edge and these deviations become comparable with the separations between the two levels, the bulk modes start admixing with the corresponding edge modes, so that at $|E| \gtrsim \Delta$ the modes are almost completely hybridized and their energies quickly approach their $\Delta = 0$ counterparts (dashed lines in Fig. 2.3). As the guiding center y_k of the bulk states crosses the right edge of the ribbon, these mixed bulk-edge modes evolve further into conventional quantum Hall edge states similar to those at the higher Landau levels.

The bulk wave function (2.39) of the level $n = 1$ is extended through a larger y interval and therefore is perturbed stronger by the edge than the wave function (2.37) of the level $n = 0$. Because of this, the level $n = 1$ starts dispersing downwards at smaller k, and the avoided crossings $\mathcal{A}1$ and $\mathcal{A}2$ of the partially mixed bulk $n = 1$ and double layer edge modes with bulk $n = 0$ plateau and dispersionless single layer edge branch are formed (Fig. 2.4). The third avoided crossing $\mathcal{A}3$ occurs when the double layer right edge state mode intersects either the left edge double layer mode [Fig. 2.3(a)] or the bulk $n = 1$ plateau [Fig. 2.3(b)–(d)], depending on the magnetic field strength and the width of the ribbon.

In the case $2\Delta \ll \epsilon_0$, the structure of the spectrum at the energy scale $|E| \lesssim \Delta$ is almost independent of the gap parameter. The main effect of decreasing Δ is that the bulk and edge modes start mixing and approach their $\Delta = 0$ counterparts at smaller k, see Figs. 2.2 (b),(c).

The spacings between higher Landau levels ($|n| \geq 2$) decrease with decreasing magnetic field or increasing gate voltage. In particular, when the parameter Δ/ϵ_0 is increased above the threshold value of $1/2$, the crossings of different Landau levels occur [35] and the levels $n = 0$ and $n = 1$ are no longer the lowest ones. The numerical results for the energy spectrum in this regime are shown in Fig. 2.5.

As one can see from Eqs. (2.38)–(2.41) and (2.44)–(2.46), all four edge modes at large momenta do not depend on magnetic field strength. Indeed, the dispersionless single layer edge modes are exactly given by Eqs. (2.38) and (2.44) at $k < 0$ in the limit of $B \to 0$ ($l \to \infty$). In Appendix 2.8 we also show that the double layer edge modes in this limit turn into the subgap edge modes described by the dispersion equation [26]

$$\hbar^2 v_F^2 (k + \kappa_+)(k + \kappa_-) = (E \mp \Delta)^2, \tag{2.49}$$

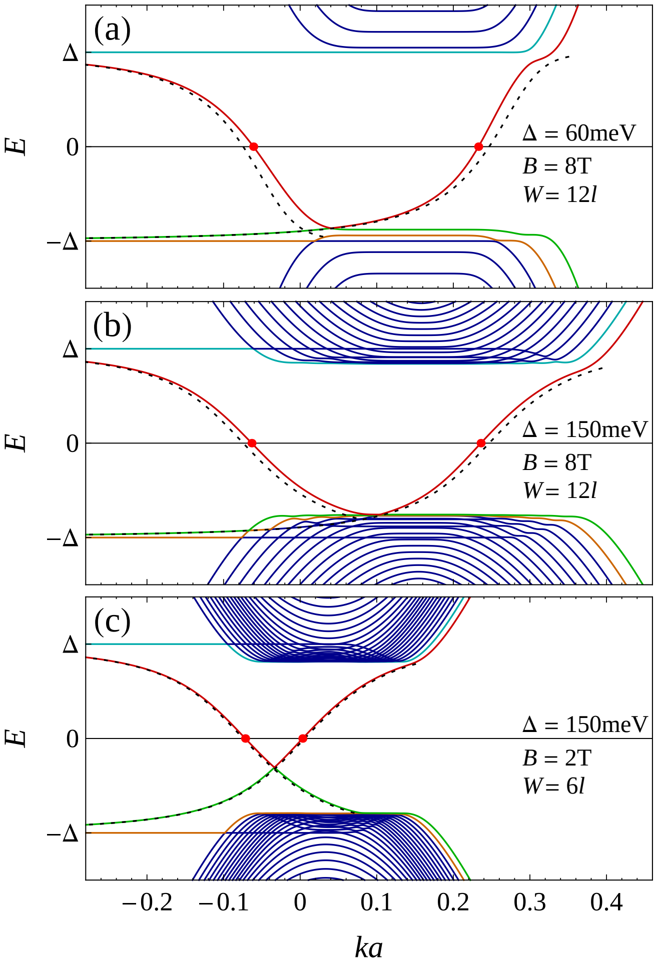

Figure 2.5: Numerical results for the low-energy spectrum in the K_+ valley for zigzag ribbon of a constant width $W \simeq 110\,\text{nm}$ at different values of magnetic field and gap parameter $\Delta > \epsilon_0/2$. Dotted lines show the subgap edge modes at $B = 0$ (right edge mode is shifted horizontally with $k \to k + W/l^2$ in order to illustrate the effect of a magnetic field). Gapless edge states at $\mu_s = 0$ are marked by dots.

where

$$\kappa_\pm^2 = k^2 - \frac{E^2 + \Delta^2 \pm i\sqrt{\gamma_1^2(\Delta^2 - E^2) - 4E^2\Delta^2}}{\hbar^2 v_F^2}, \qquad \mathrm{Re}\,\kappa_\pm > 0, \tag{2.50}$$

and the upper (lower) sign in Eq. (2.49) is chosen for the left (right) edge mode.

Moderate magnetic fields change the dispersion of the left edge states determined by equation (2.49) only slightly, whereas the right edge mode becomes partially hybridized with the states of the bulk $n = 1$ Landau level (Fig. 2.4) and shifted horizontally with $\delta k = W/l^2$.

At large negative momenta all four branches continue as their counterparts in the K_- valley, with the energy spectrum and the corresponding wave functions related by Eqs. (2.35)–(2.36). Thus the width of each edge state mode is equal to $2\pi/(3a)$, i.e., the spacing between K_+ and K_- points (although not captured by the continuum model, this fact can be directly seen from the tight-binding calculations [28, 29]). The finiteness of the branches can be taken into account within a continuum model by introducing the momentum cutoffs $k_c^{(\prime)} = -\pi/(3a)$ for the left (right) edge modes in the K_+ valley, and the corresponding cutoffs in the K_- valley. These cutoffs can be seen in Figs. 2.2 (d)–(e).

The electronic structure described above implies that current-carrying gapless edge states (states located at the Fermi level, $E = \mu_s \equiv \mu + s\mu_Z$, $s = \pm$, where μ is the chemical potential and $\mu_Z = \mu_B B \approx 0.06\,B[\mathrm{T}]$ meV is the Zeeman energy) are always present for all realistic magnetic fields. At $\mu = 0$ and $\mu_Z \ll \Delta$, there are two gapless states in each valley, which carry currents in opposite directions on a given edge (with both valleys taken into account, the net current is zero) [28, 29]. Zero-energy states exist if the energy of the $n = 1$ Landau level $E_1^{-,+}$ is negative. This condition is violated only at ultrahigh magnetic fields [see Fig. 2.3(e)] exceeding B_{cr}, the exact value of which can be determined from Eq. (2.13) at $E = 0$,

$$\epsilon_0^2 = \gamma_1^2 + \Delta^2, \tag{2.51}$$

which implies

$$B_{\mathrm{cr}}\,[\mathrm{T}] \approx 123[1 + (2.5\Delta[\mathrm{eV}])^2]. \tag{2.52}$$

In Fig. 2.6, the evolution of the gapless states at $\mu_s = 0$ with increasing magnetic field is shown: the left edge state in the K_+ valley remains almost unchanged, while the right edge state becomes partially admixed with the $n = 1$ bulk state.

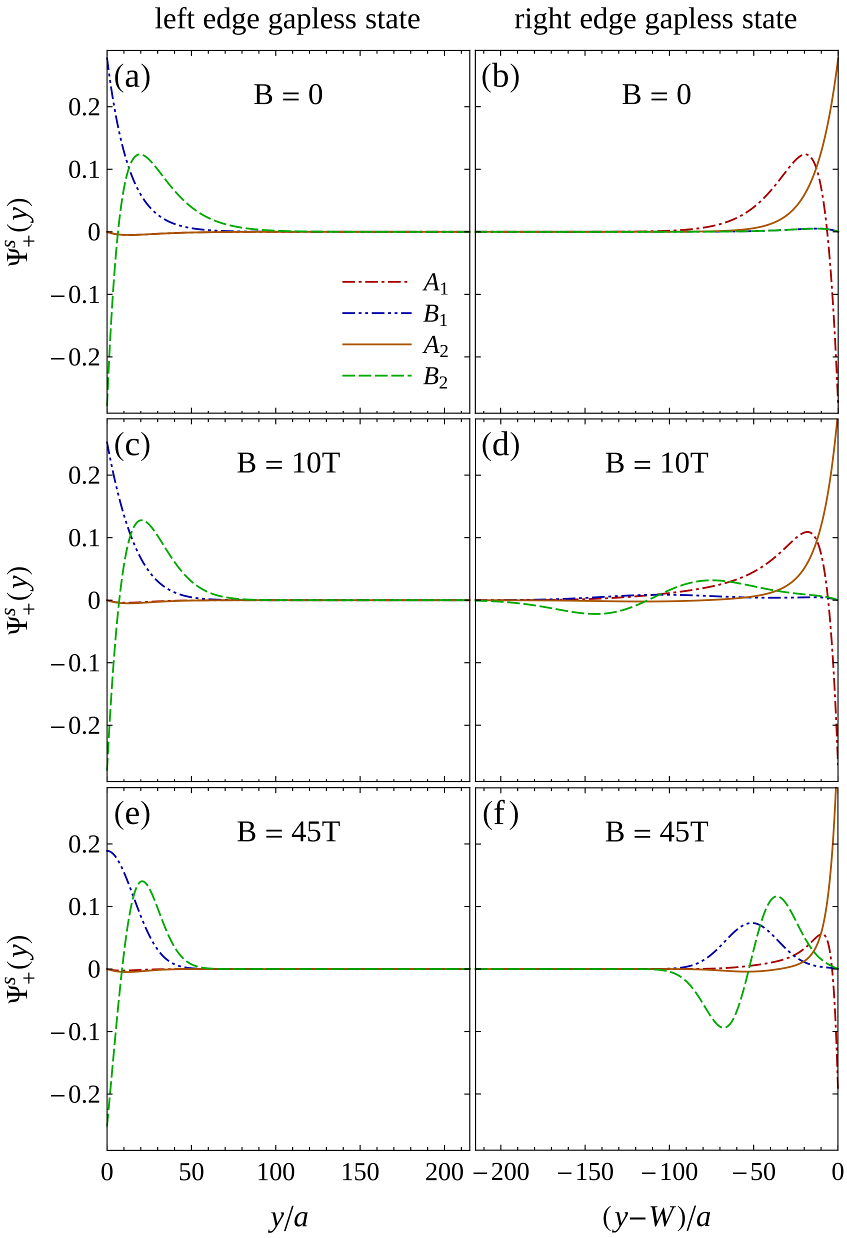

Figure 2.6: Wave functions of zero-energy states in a wide zigzag ribbon in the K_+ valley at $\Delta = 10\,\text{meV}$ and different values of a magnetic field.

2.4 Armchair edges

2.4.1 General solution with y translational invariance

In the armchair edge case, the solution (2.6) has to be modified as follows. We consider the edge(s) along the y axis and choose the gauge $\mathbf{A} = (0, Bx)$. The wave functions are plane waves in the y direction,

$$\Psi^s_\xi(x,y) = e^{iky}\widetilde{\Psi}^s_\xi(x,k), \tag{2.53}$$

where the envelope functions $\widetilde{\Psi}^s_\xi(x,k) \equiv \widetilde{\Psi}^s_\xi(\eta)$ depend only on a single combination of the variables, $\eta = x/l + kl$, and satisfy the equation

$$\xi \begin{pmatrix} \Delta & -i\epsilon_0\hat{a} & 0 & 0 \\ i\epsilon_0\hat{a}^\dagger & \Delta & \xi\gamma_1 & 0 \\ 0 & \xi\gamma_1 & -\Delta & -i\epsilon_0\hat{a} \\ 0 & 0 & i\epsilon_0\hat{a}^\dagger & -\Delta \end{pmatrix} \widetilde{\Psi}^s_\xi(\eta) = E\widetilde{\Psi}^s_\xi(\eta), \tag{2.54}$$

or, equivalently, Eq. (2.4) with the solution related by the unitary transformation

$$\Psi^s_\xi(\eta) = \hat{S}^{-1}\widetilde{\Psi}^s_\xi(\eta), \qquad \hat{S} = \begin{pmatrix} i & 0 & 0 & 0 \\ 0 & 1 & 0 & 0 \\ 0 & 0 & 1 & 0 \\ 0 & 0 & 0 & -i \end{pmatrix}. \tag{2.55}$$

Therefore, the general solution in this case is

$$\widetilde{\Psi}^s_\xi(\eta) = \sum_{i=1}^{4} C^\xi_i \widetilde{\Phi}^{(i)}_\xi(\eta), \tag{2.56}$$

where

$$\widetilde{\Phi}^{(i)}_\xi(\eta) = \hat{S}\,\Phi^{(i)}_\xi(\eta). \tag{2.57}$$

2.4.2 Dispersion equation for half-plane

On a semi-infinite plane $x > 0$, the normalizable wave functions are given in terms of only $U(a,z)$ function, and the solution is

$$\widetilde{\Psi}^s_\xi(\eta) = C^\xi_1\widetilde{\Phi}^{(1)}_\xi(\eta) + C^\xi_2\widetilde{\Phi}^{(2)}_\xi(\eta). \tag{2.58}$$

At the armchair edge $x = 0$ (which corresponds to $\eta = kl$) of a semi-infinite plane, the appropriate boundary conditions for the continuum model are that the wave function should vanish on both sublattices [5,6] and layers:

$$\sum_{\xi=\pm} \widetilde{\Psi}^{s}_{\xi A_i}(kl) = \sum_{\xi=\pm} \widetilde{\Psi}^{s}_{\xi B_i}(kl) = 0, \qquad i = 1, 2. \tag{2.59}$$

These boundary conditions mix the components of the wave function from two valleys $\xi = \pm$, and we have the system of 4 equations

$$\begin{aligned} &\sum_{\xi=\pm}\Big[C^{\xi}_{1}\widetilde{\Phi}^{(1)}_{\xi A_i}(kl) + C^{\xi}_{2}\widetilde{\Phi}^{(2)}_{\xi A_i}(kl)\Big] = 0, \\ &\sum_{\xi=\pm}\Big[C^{\xi}_{1}\widetilde{\Phi}^{(1)}_{\xi B_i}(kl) + C^{\xi}_{2}\widetilde{\Phi}^{(2)}_{\xi B_i}(kl)\Big] = 0, \qquad i = 1, 2, \end{aligned} \tag{2.60}$$

which has a nontrivial solution when the corresponding determinants of coefficient functions are zero. This condition can be written as

$$\frac{1}{(\lambda^{+}_{2} - \lambda^{+}_{1})(\lambda^{-}_{2} - \lambda^{-}_{1})} \det \begin{pmatrix} a^{+}_{1} & a^{+}_{2} & d^{-}_{1} & d^{-}_{2} \\ b^{+}_{1} & b^{+}_{2} & c^{-}_{1} & c^{-}_{2} \\ c^{+}_{1} & c^{+}_{2} & b^{-}_{1} & b^{-}_{2} \\ d^{+}_{1} & d^{+}_{2} & a^{-}_{1} & a^{-}_{2} \end{pmatrix} = 0, \tag{2.61}$$

where

$$\begin{aligned} a^{\pm}_{i} &= \nu_{\pm}(\lambda^{\pm}_{i})U\Big(\frac{3}{2} - \lambda^{\pm}_{i},\, \sqrt{2}kl\Big), \\ b^{\pm}_{i} &= \frac{E \pm \Delta}{\epsilon_0}U\Big(\frac{1}{2} - \lambda^{\pm}_{i},\, \sqrt{2}kl\Big), \\ c^{\pm}_{i} &= \frac{(E \pm \Delta)^2 - \epsilon_0^2\lambda^{\pm}_{i}}{\epsilon_0\gamma_1}U\Big(\frac{1}{2} - \lambda^{\pm}_{i},\, \sqrt{2}kl\Big), \\ d^{\pm}_{i} &= -U\Big(-\frac{1}{2} - \lambda^{\pm}_{i},\, \sqrt{2}kl\Big). \end{aligned} \tag{2.62}$$

It is easy to see that the l.h.s. of the dispersion equation (2.61) does not depend on the sign of the energy, therefore, the spectrum is symmetric under the transformation $E \to -E$. The corresponding wave functions are transformed as

$$\Psi^{s}_{\xi}(x, k) \to \xi C \begin{pmatrix} \sigma_0 & 0 \\ 0 & -\sigma_0 \end{pmatrix} \Psi^{s}_{-\xi}(x, k), \tag{2.63}$$

where σ_0 is a unit 2×2 matrix.

2.4.3 Dispersion equations for ribbon

The boundary conditions at two armchair edges $x = 0$ and $x = W$ (corresponding to $\eta = kl$ and $\eta = W/l + kl$, respectively) are

$$\sum_{\xi=\pm}\widetilde{\Psi}^s_{\xi A_i}(kl) = \sum_{\xi=\pm}\widetilde{\Psi}^s_{\xi B_i}(kl) = \sum_{\xi=\pm}\widetilde{\Psi}^s_{\xi A_i}(W/l+kl) = \sum_{\xi=\pm}\widetilde{\Psi}^s_{\xi B_i}(W/l+kl) = 0, \qquad i = 1,2, \tag{2.64}$$

i.e., the boundary condition (2.59) is imposed at both ribbon edges. These valley mixing boundary conditions lead to the system of 8 equations

$$\begin{aligned}
&\textstyle\sum_{j=1}^4\sum_{\xi=\pm} C^\xi_j\widetilde{\Phi}^{(j)}_{\xi A_i}(kl) = 0,\\
&\textstyle\sum_{j=1}^4\sum_{\xi=\pm} C^\xi_j\widetilde{\Phi}^{(j)}_{\xi B_i}(kl) = 0,\\
&\textstyle\sum_{j=1}^4\sum_{\xi=\pm} C^\xi_j\widetilde{\Phi}^{(j)}_{\xi A_i}(W/l+kl) = 0,\\
&\textstyle\sum_{j=1}^4\sum_{\xi=\pm} C^\xi_j\widetilde{\Phi}^{(j)}_{\xi B_i}(W/l+kl) = 0, \qquad i = 1,2.
\end{aligned} \tag{2.65}$$

Equating the determinant of the above system to zero, one gets the dispersion equation for the ribbon with armchair edges. After some algebra, it can be written as

$$\frac{1}{(\lambda_2^+-\lambda_1^+)^2(\lambda_2^--\lambda_1^-)^2}\det\begin{pmatrix} Z_1(kl) & Z_1(W/l+kl)\\ Z_2(kl) & Z_2(W/l+kl)\end{pmatrix} = 0, \tag{2.66}$$

where

$$Z_i(\eta) = \begin{pmatrix} X_i^+(\eta) & Y_i^+(\eta)\\ Y_i^-(\eta) & X_i^-(\eta)\end{pmatrix} \tag{2.67}$$

is a 4×4 matrix constructed with 2×2 blocks $X_i^\pm(\eta)$, $Y_i^\pm(\eta)$ defined in Eqs. (2.30), (2.31).

The spectrum is symmetric both with respect to the change of the sign of energy, with the wave function being transformed according to Eq. (2.63), and the transformation $k \to -W/l^2 - k$, with the wave functions transforming as

$$\Psi^s_\xi(x,k) \to C\begin{pmatrix}\sigma_3 & 0\\ 0 & -\sigma_3\end{pmatrix}\Psi^s_\xi(W-x, -W/l^2-k). \tag{2.68}$$

2.4.4 Numerical results for the spectra

We numerically solve the dispersion equations (2.61) and (2.66) in the case of the semi-infinite plane and the finite width ribbon, respectively. The examples of the spectra showing a few lower Landau levels in the case of a half-plane and two different widths of the ribbon are shown in Fig. 2.7.

On a half-plane, the branches of the spectrum asymptotically approach the bulk Landau levels given by Eqs. (2.12)–(2.14). The states corresponding to these bulk asymptotes (plateaus) are localized in the bulk and centered along the x direction at $x_k = -kl^2$ [the position wavevector duality in the gauge $A = (0, Bx)$]. These states are bulk states predominantly concentrated on a single valley K_ξ and approximately described by the infinite plane solutions (2.15) with $\eta = x/l + kl$, transformed according to Eq. (2.55). The same is true for wide ribbons $W \gg l$ [see Fig. 2.7(b)], where the plateaus closely approaching the bulk Landau levels are developed. For a given branch, all states to the left (right) of the bulk plateau are localized in the vicinity of the edge $x = W$ ($x = 0$).

Similarly to the zigzag edge case, the widths of the Landau level plateaus with larger $|n|$ are smaller due to the growing localization lengths of the bulk states. For the same reason, the avoided crossings of the branches corresponding to $n = 0$ and $n = 1$ Landau levels are formed.

In contrast to the zigzag case, there are no additional edge state branches, and gapless quantum Hall edge states exist only when the chemical potential (including the Zeeman energy) μ_s exceeds the spectrum gap. The latter is determined by the energy of the lowest-lying Landau level. At $2\Delta < \epsilon_0$ the lowest level is $n = 1$ and the spectrum gap is equal to $2|E_1^{-,+}|$, whereas at $2\Delta > \epsilon_0$, the gap in the spectrum is determined by the higher Landau levels. This gap decreases monotonically with increasing B, closes at $B = B_{\mathrm{cr}}$ given by Eq. (2.52) and then grows again (Fig. 2.8). For all experimentally accessible values of magnetic field and layer asymmetry gap, the size of the spectrum gap varies between Δ and 2Δ.

2.5 Conclusions

In summary, we studied the spectrum of biased bilayer graphene with zigzag or armchair edges in a magnetic field within the continuum four-band model. We derived the general analytic solution for the wave functions in a ribbon with zigzag or armchair edges. For both edge types, the exact dispersion equations were written in terms of the parabolic cylinder functions. Solving these dispersion equations numerically, we obtained the spectra of noninteracting electrons in a bilayer graphene ribbon or semi-infinite plane at different values of magnetic field and

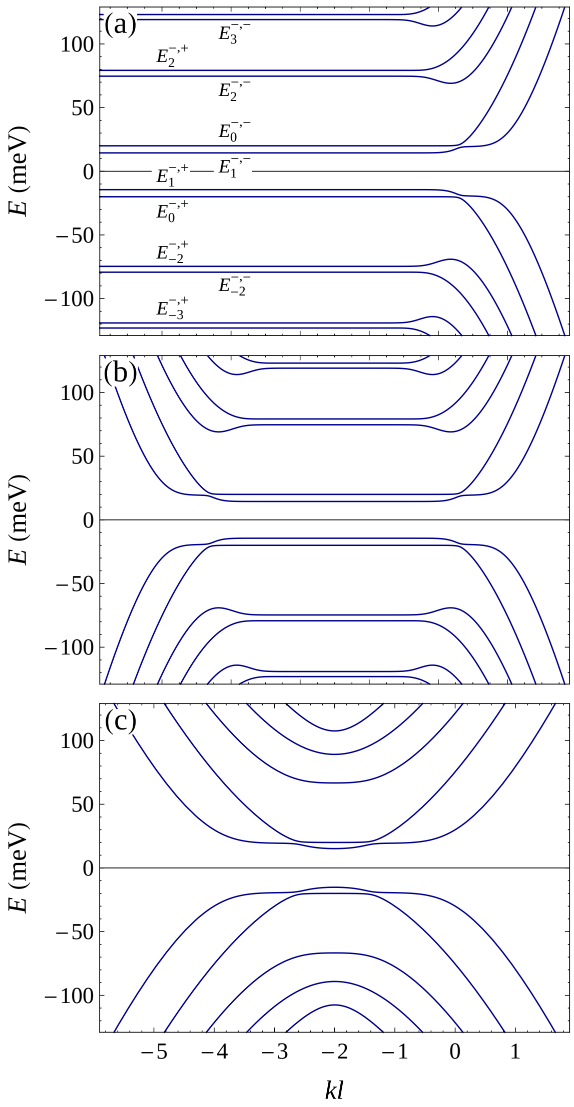

Figure 2.7: Numerical results for the low-energy spectrum in bilayer graphene with armchair edge(s) at $B = 20\,\mathrm{T}$ and $\Delta = 20\,\mathrm{meV}$: (a) half-plane, (b) ribbon of the width $W = 10l$, (c) ribbon of the width $W = 4l$. On panel (a), the bulk Landau level energies $E_n^{\kappa,\xi}$ are indicated.

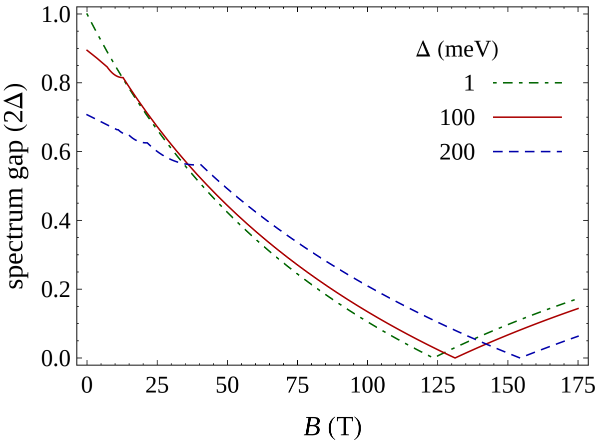

Figure 2.8: Gap in the spectrum (in the units of 2Δ) in the armchair edge case as a function of a magnetic field at different values of Δ.

layer asymmetry gap induced by the gate voltage.

The edge state spectrum close to the charge neutrality point is found to depend strongly on the edge type. Zigzag edges are shown to support zero-energy edge states propagating in opposite directions in the two valleys, in agreement with the previous tight-binding studies [28–31]. Some of these states remain almost unchanged when the magnetic field is turned on and increased up to the highest values currently accessible in experiments, whereas the others become partially hybridized with the bulk state of the $n = 1$ Landau level. The behavior of the lowest-energy spectrum branches at large momenta as well as their zero magnetic field limit has been investigated in detail by using the asymptotic properties of the parabolic cylinder functions. In contrast, the spectrum of armchair bilayer graphene ribbon is gapped and zero-energy edge states are absent. The gap in the edge state spectrum is equal to the gate-voltage induced bulk gap (Fig. 2.8), the size of which is determined both by the gap parameter Δ and the magnetic field strength.

The obtained structure of edge states suggests the following implications on transport properties of bilayer graphene ribbon in the quantum Hall regime at zero filling. When the spin splitting is less than the gate induced gap, the current-carrying gapless edge states are present only in the case of zigzag edges. In clean samples with ideal zigzag edges, these states should form the conducting channels resulting in the metallic state with the finite two-terminal or four-terminal longitudinal conductance equal to $4e^2/h$ (corresponding to the states with different spin projections at each edge of the ribbon). However, these edge channels are not protected against the backscattering in the presence the valley-mixing edge disorder, therefore their contribution to the conductance can be sensitive to the edge structure of real samples [27]. When the spin splitting exceeds the gate induced gap, metallic behavior is expected regardless of the edge type due to the counterpropagating gapless edge states with opposite spin projections [6, 9, 10, 39, 40].

While the present chapter deals with the case of nonzero layer asymmetry gap and the spin splitting, it would be interesting to extend our analysis to a more general set of order parameters, similarly to the studies of Refs. [21, 22] in monolayer graphene. Experiments with bilayer graphene in magnetic fields at the charge neutrality point reveal different phases with spontaneously broken symmetries [41–43], and the knowledge of low-energy edge state structure is essential for identifying the true nature of the ground state in each phase [39,40,43].

2.6 Appendix A. Derivation of the general solution

Let us start with equation (2.4) for the K_+ valley, which is written in components as

$$\begin{aligned}
\epsilon_0 \hat{a} \Psi^s_{+B_1} &= -(E-\Delta)\Psi^s_{+A_1}, \\
\epsilon_0 \hat{a}^\dagger \Psi^s_{+A_1} &= -(E-\Delta)\Psi^s_{+B_1} + \gamma_1 \Psi^s_{+A_2}, \\
\epsilon_0 \hat{a} \Psi^s_{+B_2} &= -(E+\Delta)\Psi^s_{+A_2} + \gamma_1 \Psi^s_{+B_1}, \\
\epsilon_0 \hat{a}^\dagger \Psi^s_{+A_2} &= -(E+\Delta)\Psi^s_{+B_2}.
\end{aligned} \tag{2.69}$$

Eliminating $\Psi^s_{+A_1}$, $\Psi^s_{+A_2}$ and $\Psi^s_{+B_2}$ leads to the fourth order differential equation

$$\left[\epsilon_0^2 \hat{a}\hat{a}^\dagger - (E+\Delta)^2\right]\left[\epsilon_0^2 \hat{a}^\dagger \hat{a} - (E-\Delta)^2\right]\Psi^s_{+B_1} = \gamma_1^2 (E^2-\Delta^2)\Psi^s_{+B_1}, \tag{2.70}$$

which admits the factorization [35]

$$\left(\partial_\eta^2 - \eta^2 - 1 + 2\lambda_1^+\right)\left(\partial_\eta^2 - \eta^2 - 1 + 2\lambda_2^+\right)\Psi^s_{+B_1}(\eta) = 0 \tag{2.71}$$

with $\lambda^\xi_{1,2}$ defined in Eq. (2.7). Therefore, the general solutions of equations

$$\left(\partial_\eta^2 - \eta^2 - 1 + 2\lambda_i^+\right)\Psi_{+B_1}(\eta) = 0, \qquad i = 1, 2, \tag{2.72}$$

given by the pairs of the linearly independent parabolic cylinder functions $U(1/2 - \lambda_i,\ \sqrt{2}\eta)$, $V(1/2 - \lambda_i,\ \sqrt{2}\eta)$, also satisfy Eq. (2.71). Combining these solutions gives

$$\begin{aligned}\Psi_{+B_1}(\eta) = {} & C_1 U\Big(\frac{1}{2} - \lambda_1^+,\ \sqrt{2}\eta\Big) + C_2 U\Big(\frac{1}{2} - \lambda_2^+,\ \sqrt{2}\eta\Big) \\ & + C_3 V\Big(\frac{1}{2} - \lambda_1^+,\ \sqrt{2}\eta\Big) + C_4 V\Big(\frac{1}{2} - \lambda_2^+,\ \sqrt{2}\eta\Big).\end{aligned} \tag{2.73}$$

All four functions in the above equation are linearly independent at $\lambda_1^+ \neq \lambda_2^+$, which can be proved in the following way. The functions $U(a_1, z)$, $U(a_2, z)$, $V(a_1, z)$, $V(a_2, z)$, where $a_{1,2} = -1/2 - \lambda_{1,2}^+$ and $z = \sqrt{2}\eta$, are the solutions of differential equation (2.71) which has zero coefficient at the third derivative term. This implies [44] that the Wronskian of these functions is equal to some constant, dependent on the parameters $a_{1,2}$. The value of this constant can be found, for example, by evaluating the Wronskian at $z \to +\infty$ and using the asymptotic expressions for the parabolic cylinder functions [34]

$$U\Big(a - \frac{1}{2}, z\Big) = e^{-\frac{z^2}{4}} z^{-a}\Big[1 - \frac{a(a+1)}{2z^2} + \frac{a(a+1)(a+2)(a+3)}{8z^4} - \dots\Big], \tag{2.74}$$

$$V\Big(a + \frac{1}{2}, z\Big) = \sqrt{\frac{2}{\pi}} e^{\frac{z^2}{4}} z^{a}\Big[1 + \frac{a(a-1)}{2z^2} + \frac{a(a-1)(a-2)(a-3)}{8z^4} + \dots\Big]. \tag{2.75}$$

The result is

$$\mathcal{W}\Big[U(a_1, z), U(a_2, z), V(a_1, z), V(a_2, z)\Big] = \frac{2}{\pi}(a_1 - a_2)^2. \tag{2.76}$$

At $\lambda_1^+ = \lambda_2^+$ [this equality is possible in the case $\epsilon_0^4 < 4\Delta^2(\gamma_1^2 + 4\Delta^2)$], the solutions in Eq. (2.73) are not linearly independent. This can be fixed by rearranging terms as

$$\begin{aligned}\Psi_{+B_1}(\eta) = {} & \widetilde{C}_1 U(1/2 - \lambda_1^+,\ \sqrt{2}\eta) + \widetilde{C}_2 \frac{U(1/2 - \lambda_1^+,\ \sqrt{2}\eta) - U(1/2 - \lambda_2^+,\ \sqrt{2}\eta)}{\lambda_1^+ - \lambda_2^+} \\ & + \widetilde{C}_3 V(1/2 - \lambda_1^+,\ \sqrt{2}\eta) + \widetilde{C}_4 \frac{V(1/2 - \lambda_1^+,\ \sqrt{2}\eta) - V(1/2 - \lambda_2^+,\ \sqrt{2}\eta)}{\lambda_1^+ - \lambda_2^+},\end{aligned} \tag{2.77}$$

where the resulting four solutions are linearly independent at arbitrary $\lambda_{1,2}^+$, with the corresponding Wronskian

$$\mathcal{W}\Big[U(a_1, z), \frac{U(a_2, z) - U(a_1, z)}{a_2 - a_1}, V(a_1, z), \frac{V(a_2, z) - V(a_1, z)}{a_2 - a_1}\Big] = \frac{2}{\pi}. \tag{2.78}$$

The remaining components of Ψ_+^s can be obtained from Eqs. (2.69) and (2.73) by using the recurrence relations for the parabolic cylinder functions, which are written in terms of operators

$\hat{a}$ and $\hat{a}^\dagger$ as

$$\hat{a}U\Big(-\lambda - 1/2,\ \sqrt{2}\eta\Big) = \lambda\, U\Big(-\lambda + 1/2,\ \sqrt{2}\eta\Big), \tag{2.79}$$

$$\hat{a}^\dagger U\Big(-\lambda + 1/2,\ \sqrt{2}\eta\Big) = U\Big(-\lambda - 1/2,\ \sqrt{2}\eta\Big), \tag{2.80}$$

$$\hat{a}V\Big(-\lambda - 1/2,\ \sqrt{2}\eta\Big) = V\Big(-\lambda + 1/2,\ \sqrt{2}\eta\Big), \tag{2.81}$$

$$\hat{a}^\dagger V\Big(-\lambda + 1/2,\ \sqrt{2}\eta\Big) = \lambda\, V\Big(-\lambda - 1/2,\ \sqrt{2}\eta\Big). \tag{2.82}$$

The overall factors for the solutions are chosen in such a way that no singularities arise at $E = \pm\Delta$. This leads to expressions (2.6)–(2.9) with $\xi = +$. The corresponding solutions for the K_- valley can be obtained by making the formal replacement $E \to -E$, $\gamma_1 \to -\gamma_1$.

2.7 Appendix B. Large momentum asymptotes

Here we consider the case of a wide zigzag ribbon ($W \gg l$) so that the influence of the right edge can be neglected and derive the large momentum asymptotes for the modes in the K_+ valley localized near the left edge by using the corresponding dispersion equation (2.24) for the semi-infinite plane. Assuming $\lambda_1^\xi \neq \lambda_2^\xi$ and $E \neq \pm\Delta$ it can be written as

$$\frac{(\lambda_1^+ - 1)w_{\lambda_1^+ - 1}(\sqrt{2}kl)}{(E-\Delta)^2 - (\lambda_1^+ - 1)\epsilon_0^2} = \frac{(\lambda_2^+ - 1)w_{\lambda_2^+ - 1}(\sqrt{2}kl)}{(E-\Delta)^2 - (\lambda_2^+ - 1)\epsilon_0^2}, \tag{2.83}$$

where

$$w_\lambda(z) = \frac{U(1/2 - \lambda, -z)}{U(-1/2 - \lambda, -z)}. \tag{2.84}$$

For the modes in the K_+ valley localized at the right edge of the ribbon, we employ the half-plane dispersion equation (2.25) for the K_- valley, which can be written as

$$\Big[(E-\Delta)^2 - \lambda_1^- \epsilon_0^2\Big] w_{\lambda_1^-}\Big(\sqrt{2}kl\Big) = \Big[(E-\Delta)^2 - \lambda_2^- \epsilon_0^2\Big] w_{\lambda_2^-}\Big(\sqrt{2}kl\Big), \tag{2.85}$$

and use the correspondence (2.35)–(2.36) between the solutions in different valleys.

We are interested in the large kl asymptotics of the solutions of Eqs. (2.83) and (2.85) in the case when at least one of the parameters $\lambda_{1,2}^\xi$ approaches some integer value. This corresponds to the spectrum near the bulk Landau level plateaus or the low-energy edge modes with horizontal asymptotes $E \to \pm\Delta$. Using asymptotic expansions (2.74)–(2.75) and relations (2.32)–(2.33) between different parabolic cylinder functions, we get at $z \gg 1$, $|\epsilon| \ll 1$:

$$w_{n+\epsilon}(z) \simeq -z\frac{\sqrt{2\pi}(n-1)!\epsilon - z^{2n-1}e^{-z^2/2}}{\sqrt{2\pi}n!\epsilon - z^{2n+1}e^{-z^2/2}}, \qquad n = 1, 2, 3, \ldots, \tag{2.86}$$

$$w_{\epsilon}(z) \simeq \frac{\sqrt{2\pi}z}{ze^{-z^2/2} - (1 + 1/z^2)\epsilon\sqrt{2\pi}}, \tag{2.87}$$

$$w_\lambda(z) \simeq -\frac{z}{\lambda}\left(1 - \frac{\lambda+1}{z^2}\right), \quad \lambda \neq 0, 1, 2, \ldots, \tag{2.88}$$

$$w_\lambda(-z) \simeq \frac{1}{z}\left(1 + \frac{\lambda-1}{z^2}\right). \tag{2.89}$$

Using the above approximations, we find the asymptotic form of the solutions to dispersion equations (2.83) and (2.85) at $|k|l \gg 1$. The corresponding wave functions are then obtained from the half-plane solution satisfying the boundary conditions, which can be written as

$$\Psi^s_\xi(\eta) = C^\xi_1 f^\xi_{\lambda^\xi_1}(\eta) + C^\xi_2 f^\xi_{\lambda^\xi_2}(\eta) \tag{2.90}$$

with

$$\begin{aligned} C^+_j &= (-1)^j\Big[U\Big(1/2 - \lambda^+_j, -\sqrt{2}kl\Big)\Big]^{-1}, \\ C^-_j &= (-1)^j\Big[U\Big(-1/2 - \lambda^-_j, -\sqrt{2}kl\Big)\Big]^{-1}. \end{aligned} \tag{2.91}$$

Let us start with dispersion equation (2.83) for the K_+ valley. For the double layer edge mode ($E \simeq \Delta$, $\lambda^+_{1(2)} \simeq 1$, $\lambda^+_{2(1)} \simeq 4\Delta^2/\epsilon_0^2$, $-kl \gg 1$) we use Eq. (2.89) and arrive at

$$E \simeq \Delta\left(1 - \frac{\gamma_1^2}{\epsilon_0^2 k^2 l^2}\right), \tag{2.92}$$

which is equivalent to Eq. (2.40). Note that both the $n = 0$ Landau level and the single layer edge mode are strictly dispersionless with their energy $E = -\Delta$ being an exact solution of the half-plane dispersion equation (2.24). For the dispersion near the bulk $n = 1$ level ($E \simeq E_1^{-,+}$, $\lambda^+_{1(2)} \simeq 1$, $\lambda^+_{2(1)} \simeq 2(E_1^2 + \Delta^2)/\epsilon_0^2$, $kl \gg 1$) we use Eqs. (2.87)–(2.88) and arrive at

$$E \simeq E_1^{-,+} + \frac{(E_1^{-,+} - \Delta)^2\epsilon_0^2 kl\, e^{-k^2l^2}}{2\sqrt{\pi}[\Delta\gamma_1^2 + (E_1^{-,+} + \Delta)(E_1^{-,+} - \Delta)^2]}. \tag{2.93}$$

In the K_- valley, we consider only the case $kl \gg 1$. For the double layer edge mode ($E \simeq \Delta$,

$\lambda_1^- \simeq 0$, $\lambda_2^- \simeq 1 + 4\Delta^2/\epsilon_0^2$) we use Eqs. (2.87)–(2.88) and arrive at Eq. (2.92), which translates into the asymptotic formula (2.45) for the right double layer edge mode in the K_+ valley.

For the single layer edge mode ($E \simeq -\Delta$, $\lambda_{1(2)}^- \simeq 1$, $\lambda_{2(1)}^- \simeq 4\Delta^2/\epsilon_0^2$) we use Eqs. (2.86) with $n = 1$ and (2.88), which leads to

$$E \simeq -\Delta\left(1 + \frac{\epsilon_0^2(\epsilon_0^2 - 4\Delta^2)kl\, e^{-k^2l^2}}{2\sqrt{\pi}\Delta^2\gamma_1^2}\right). \tag{2.94}$$

For the bulk $n = 0$ level ($E \simeq \Delta$, $\lambda_1^- \simeq 0$, $\lambda_2^- \simeq 1 + 4\Delta^2/\epsilon_0^2$) we use Eqs. (2.87)–(2.88) and arrive at

$$E \simeq \Delta\left(1 + \frac{\epsilon_0^4 k^3 l^3 e^{-k^2l^2}}{\sqrt{\pi}\Delta^2\gamma_1^2}\right). \tag{2.95}$$

For the bulk $n = 1$ level ($E \simeq E_1^{-,-}$, $\lambda_{1(2)}^- \simeq 1$, $\lambda_{2(1)}^- \simeq 2(E_1^2 + \Delta^2)/\epsilon_0^2$) we use Eqs. (2.86) with $n = 1$ and (2.88) and arrive at

$$E \simeq E_1^{-,-} + \frac{1}{\sqrt{\pi}}\left(\frac{E_1^{-,-} + \Delta}{E_1^{-,-} - \Delta}\right)^2 \frac{\epsilon_0^4 k^3 l^3 e^{-k^2l^2}}{(E_1^{-,-} - \Delta)(E_1^{-,-} + \Delta)^2 - \Delta\gamma_1^2}. \tag{2.96}$$

The exponentially small deviations from the bulk Landau levels [Eqs. (2.93), (2.95), and (2.96)] and the dispersionless edge state branch [Eq. (2.94)] are accompanied by exponentially small corrections to the corresponding wave functions, while for the edge modes with dispersion (2.92), the wave functions in the K_+ valley are given by Eqs. (2.41) and (2.46).

In the unbiased case ($\Delta = 0$), the spectrum is electron-hole symmetrical and the bulk Landau levels $n = 0$ and $n = 1$ are degenerate. In the vicinity of this degenerate level ($E \simeq 0$, $kl \gg 1$), one has

$$\lambda_1^- = 1 + \frac{E^2}{\epsilon_0^2}\left(1 + \frac{\gamma_1^2}{\epsilon_0^2}\right) + O(E^4/\epsilon_0^4), \tag{2.97}$$

$$\lambda_2^- = \frac{E^2}{\epsilon_0^2}\left(1 - \frac{\gamma_1^2}{\epsilon_0^2}\right) + O(E^4/\epsilon_0^4). \tag{2.98}$$

Using Eqs. (2.86)–(2.87), we find the two pairs of approximate solutions of the dispersion equation (2.85) at $kl \gg 1$,

$$E_\pm^{(a)} = \pm\frac{\epsilon_0^2\, e^{-k^2l^2/2}}{\pi^{1/4}\gamma_1\sqrt{2kl}}\left[1 + O\Big((kl)^{-2}\Big)\right], \tag{2.99}$$

and

$$E_{\pm}^{(b)} = \pm\frac{\epsilon_0\gamma_1}{\pi^{1/4}}\sqrt{\frac{2k^3l^3}{\gamma_1^2+\epsilon_0^2}}e^{-k^2l^2/2}\Big[1+O\Big((kl)^{-2}\Big)\Big]. \tag{2.100}$$

The corresponding wave functions (2.90) are the linear combinations of the bulk states $\Psi_-^{s\,(n=0)}$ and $\Psi_-^{s\,(n=1)}$ given by Eq. (2.15), which at $\Delta = 0$ reside solely on the A sublattice, and the two orthogonal edge states residing on the B sublattice, which at $y \ll y_k$ are given by

$$\Psi_-^{s\,(\text{edge I})}(y,k) = C_{\text{I}}\, e^{-ky+\frac{y^2}{2l^2}}\begin{pmatrix}1\\0\\0\\0\end{pmatrix}, \tag{2.101}$$

$$\Psi_-^{s\,(\text{edge II})}(y,k) = C_{\text{II}}\, e^{-ky+\frac{y^2}{2l^2}}\begin{pmatrix}c-2ky\\0\\-\frac{2\hbar v_F k}{\gamma_1}\\0\end{pmatrix}, \tag{2.102}$$

where $c = 1+(kl)^{-2}+O((kl)^{-4})$ is independent of y. More specifically, the wave functions corresponding to the lower energy solutions (2.99) in the main order in $1/(kl)$ are given by the mix of $n = 0$ bulk state and the single layer edge state,

$$\Psi_-^{s\,(a)\pm} \simeq \frac{1}{\sqrt{2}}\Big[\Psi_-^{s\,(n=0)} \pm \Psi_-^{s\,(\text{edge I})}\Big] + \frac{1}{2kl}\Big[\sqrt{1+\epsilon_0^2/\gamma_1^2}\Psi_-^{s\,(n=1)} \mp \frac{\epsilon_0}{\gamma_1}\Psi_-^{s\,(\text{edge II})}\Big], \tag{2.103}$$

while the higher energy solutions (2.100) in the main order in $1/(kl)$ correspond to the hybridized bulk $n = 1$ state and the double layer edge state,

$$\Psi_-^{s\,(b)\pm} \simeq \frac{1}{\sqrt{2}}\Big[\Psi_-^{s\,(n=1)} \pm \Psi_-^{s\,(\text{edge II})}\Big] - \frac{1}{2kl}\Big[\sqrt{1+\epsilon_0^2/\gamma_1^2}\Psi_-^{s\,(n=0)} \mp \frac{\epsilon_0}{\gamma_1}\Psi_-^{s\,(\text{edge I})}\Big]. \tag{2.104}$$

2.8 Appendix C. Limit of zero magnetic field

In the limit $B \to 0$, the argument z of the parabolic cylinder function $U(a,z)$ in Eqs. (2.8), (2.24) and (2.25) is proportional to $l \to \infty$ while its complex parameter a grows as l^2 (at fixed wave vector and energy). The appropriate asymptotic formula for this case is [45]

$$U\Big(-\frac{\mu^2}{2},\mu t\sqrt{2}\Big) = g(\mu)\frac{e^{-\mu^2\xi(t)}}{(t^2-1)^{\frac{1}{4}}}\Big[1+O(|\mu|^{-2})\Big], \tag{2.105}$$

where

$$\xi(t) = \frac{1}{2} t \sqrt{t^2 - 1} - \frac{1}{2} \ln\left(t + \sqrt{t^2 - 1}\right). \tag{2.106}$$

It is valid as $|\mu| \to \infty$, uniformly with respect to $t \in \mathbf{S}(\arg\mu)$ and $\arg\mu \in [-\pi + \epsilon, \pi - \epsilon]$, where ϵ is an arbitrary positive small constant. We will not need the explicit form of the function $g(\mu)$. The t domain of validity $\mathbf{S}$, as well as the choice of the branch of the multivalued functions in Eqs. (2.105)–(2.106) have a rather complicated dependence on $\arg\mu$ (see Ref. [45] for details). For our purposes, it is sufficient to know that the expansion is valid with the multivalued functions taken on their principal branches when μt is real, $\operatorname{Re} \sqrt{t^2 - 1} > 0$ and $|\arg t| \neq \pi$ (the value at $t = 0$ is obtained by continuity).

From (2.105) we get

$$\frac{U\left(-\mu^2/2, (\mu t + s/\mu)\sqrt{2}\right)}{U\left(-\mu^2/2, \mu t\sqrt{2}\right)} = e^{-s\sqrt{t^2-1}}\left[1 + O(|\mu|^{-2})\right], \tag{2.107}$$

and for the derivative $U'(a, z) \equiv \partial U(a, z)/\partial z$ we obtain from (2.105)

$$U'\left(-\frac{\mu^2}{2}, \mu t\sqrt{2}\right) = -\frac{\mu}{\sqrt{2}} g(\mu)(t^2 - 1)^{\frac{1}{4}} e^{-\mu^2\xi(t)}\left[1 + O(|\mu|^{-2})\right]. \tag{2.108}$$

Using Eqs. (2.105), (2.108) and recurrence relation (2.79) for the parabolic cylinder function, one has

$$\frac{U\left(1 - \mu^2/2, \mu t\sqrt{2}\right)}{U\left(-\mu^2/2, \mu t\sqrt{2}\right)} = \frac{\sqrt{2}}{\mu}\left(t - \sqrt{t^2 - 1}\right)\left[1 + O(|\mu|^{-2})\right]. \tag{2.109}$$

Taking $\mu = \sqrt{2\lambda}$, $t = -kl/\sqrt{2\lambda}$, and $s = \sqrt{2\lambda}\, y/l$, we obtain from Eqs. (2.107), (2.109):

$$\frac{U\left(-\lambda, \sqrt{2}(y/l - kl)\right)}{U\left(-\lambda, -\sqrt{2}kl\right)} = e^{-y\sqrt{k^2 - 2\lambda/l}}\left[1 + O(|\lambda|^{-1})\right], \tag{2.110}$$

$$\frac{U\left(1 - \lambda, -\sqrt{2}kl\right)}{U\left(-\lambda, -\sqrt{2}kl\right)} = -\frac{kl + \sqrt{k^2l^2 - 2\lambda}}{\sqrt{2}\lambda}\left[1 + O(|\lambda|^{-1})\right], \tag{2.111}$$

where $\operatorname{Re} \sqrt{k^2l^2 - 2\lambda} > 0$ and k must be negative if λ is real. Using Eq. (2.111) with $\lambda = \lambda_i^+ - 1/2$ and taking into account that in the limit $l \to \infty$

$$\sqrt{k^2 - 2\lambda_{1,2}^{\xi}/l} \to \kappa_\pm, \tag{2.112}$$

where $\kappa_\pm$ are defined in Eq. (2.50), the l.h.s. of dispersion equation (2.24) can be written in this limit as

$$U\Big(1/2-\lambda_1^+,-\sqrt{2}kl\Big)U\Big(1/2-\lambda_2^+,-\sqrt{2}kl\Big)\frac{(E^2-\Delta^2)(\kappa_+-\kappa_-)}{\sqrt{2}\epsilon_0\gamma_1(\lambda_1-\lambda_2)}\left[1-\frac{\epsilon_0^2l^2(k+\kappa_+)(k+\kappa_-)}{2(E-\Delta)^2}\right], \quad (2.113)$$

which immediately implies Eq. (2.49) with the upper sign for the left edge subgap mode in the K_+ valley.

In the same way, we apply Eq. (2.111) with $\lambda = \lambda_i^- + 1/2$ to the half-plane dispersion equation (2.25), which leads to the equation

$$\hbar^2 v_F^2(k-\kappa_+)(k-\kappa_-) = (E-\Delta)^2 \qquad (2.114)$$

for the left edge subgap mode in the K_- valley.

The corresponding wave functions of the left edge states in both valleys can be obtained from Eq. (2.8) by using Eqs. (2.110)–(2.112). The result reads

$$\Psi_\pm^s(y,k) = \sum_{\sigma=\pm} C_\sigma^\pm e^{-\kappa_\sigma y}\begin{pmatrix} -1 \\ \mp\frac{E\mp\Delta}{\hbar v_F(k+\kappa_\sigma)} \\ \pm\frac{\hbar^2 v_F^2(k^2-\kappa_\sigma^2)-(E\mp\Delta)^2}{\hbar v_F\gamma_1(k+\kappa_\sigma)} \\ \frac{(E\mp\Delta)(\gamma_1^2-E^2+\Delta^2)+\hbar^2v_F^2(k^2-\kappa_\sigma^2)(E\pm\Delta)}{\hbar^2 v_F^2\gamma_1(k+\kappa_\sigma)^2} \end{pmatrix}, \qquad (2.115)$$

in agreement with Ref. [26].

Zero-energy solution for the left edge subgap state in both valleys $K_{\xi=\pm}$ at $B = 0$ can be found analytically. This state is located at $\hbar v_F k = -\xi\gamma_1$ [27], and the corresponding wave function (2.115) is given by

$$\begin{aligned} \Psi_{\xi A_i}^s(y) &= Ce^{-\frac{\gamma_1 y}{2\hbar v_F}}\sin\left(\frac{\Delta y}{\hbar v_F}\right), \qquad i=1,2, \\ \Psi_{\xi B_1}^s(y) &= -Ce^{-\frac{\gamma_1 y}{2\hbar v_F}}\cos\left(\frac{\Delta y}{\hbar v_F}\right), \\ \Psi_{\xi B_2}^s(y) &= -\Psi_{\xi B_1}^s(y) - \frac{\gamma_1}{\Delta}\Psi_{\xi A_1}^s(y). \end{aligned} \qquad (2.116)$$

The dispersion equation of the right edge subgap mode in the K_+ valley [Eq. (2.49) with the lower sign] and the corresponding wave functions are obtained from Eqs. (2.114)–(2.116), using the correspondence Eqs. (2.35)–(2.36) between the spectra and the wave functions in two valleys.

Bibliography

[1] P. K. Pyatkovskiy, Phys. Rev. B **88**, 205417 (2013).

[2] B. I. Halperin, Phys. Rev. B **25**, 2185 (1982).

[3] K. S. Novoselov, A. K. Geim, S. V. Morozov, D. Jiang, Y. Zhang, S. V. Dubonos, I. V. Grigorieva, and A. A. Firsov, Science **306**, 666 (2004).

[4] N. M. R. Peres, F. Guinea, and A. H. Castro Neto, Phys. Rev. B **73**, 125411 (2006).

[5] L. Brey and H. A. Fertig, Phys. Rev. B **73**, 195408 (2006).

[6] D. A. Abanin, P. A. Lee, and L. S. Levitov, Phys. Rev. Lett. **96**, 176803 (2006).

[7] M. Fujita, K. Wakabayashi, K. Nakada, and K. Kusakabe, J. Phys. Soc. Jpn. **65**, 1920 (1996).

[8] K. Nakada, M. Fujita, G. Dresselhaus, and M. S. Dresselhaus, Phys. Rev. B **54**, 17954 (1996).

[9] H. A. Fertig and L. Brey, Phys. Rev. Lett. **97**, 116805 (2006).

[10] D. A. Abanin, P. A. Lee, and L. S. Levitov, Solid State Communications **143**, 77 (2007).

[11] K. Nomura and A. H. MacDonald, Phys. Rev. Lett. **96**, 256602 (2006).

[12] M. O. Goerbig, R. Moessner, and B. Douçot, Phys. Rev. B **74**, 161407 (2006).

[13] J. Alicea and M. P. A. Fisher, Phys. Rev. B **74**, 075422 (2006).

[14] V. P. Gusynin, V. A. Miransky, S. G. Sharapov, and I. A. Shovkovy, Phys. Rev. B **74**, 195429 (2006).

[15] E. V. Gorbar, V. P. Gusynin, V. A. Miransky, and I. A. Shovkovy, Phys. Rev. B **78**, 085437 (2008).

[16] I. F. Herbut, Phys. Rev. Lett. **97**, 146401 (2006).

[17] I. F. Herbut, Phys. Rev. B **75**, 165411 (2007).

[18] I. F. Herbut, Phys. Rev. B **76**, 085432 (2007).

[19] M. Ezawa, J. Phys. Soc. Jpn. **76**, 094701 (2007).

[20] M. Ezawa, Physica E **40**, 269 (2007).

[21] V. P. Gusynin, V. A. Miransky, S. G. Sharapov, and I. A. Shovkovy, Phys. Rev. B **77**, 205409 (2008).

[22] V. P. Gusynin, V. A. Miransky, S. G. Sharapov, I. A. Shovkovy, and C. M. Wyenberg, Phys. Rev. B **79**, 115431 (2009).

[23] E. McCann and V. I. Fal'ko, Phys. Rev. Lett. **96**, 086805 (2006).

[24] T. Ohta, A. Bostwick, T. Seyller, K. Horn, and E. Rotenberg, Science **313**, 951 (2006).

[25] E. V. Castro, N. M. R. Peres, J. M. B. Lopes dos Santos, A. H. C. Neto, and F. Guinea, Phys. Rev. Lett. **100**, 026802 (2008).

[26] J. Li, A. F. Morpurgo, M. Büttiker, and I. Martin, Phys. Rev. B **82**, 245404 (2010).

[27] J. Li, I. Martin, M. Buttiker, and A. F. Morpurgo, Nat. Phys. **7**, 38 (2011).

[28] E. V. Castro, K. S. Novoselov, S. V. Morozov, N. M. R. Peres, J. M. B. Lopes dos Santos, J. Nilsson, F. Guinea, A. K. Geim, and A. H. C. Neto, Phys. Rev. Lett. **99**, 216802 (2007).

[29] V. Mazo, E. Shimshoni, and H. A. Fertig, Phys. Rev. B **84**, 045405 (2011).

[30] S. Wu, M. Killi, and A. Paramekanti, Phys. Rev. B **85**, 195404 (2012).

[31] Y.-T. Zhang, X. C. Xie, and Q.-f. Sun, Phys. Rev. B **86**, 035447 (2012).

[32] H. Xu, T. Heinzel, and I. V. Zozoulenko, Phys. Rev. B **80**, 045308 (2009).

[33] F. Zhang, B. Sahu, H. Min, and A. H. MacDonald, Phys. Rev. B **82**, 035409 (2010).

[34] M. Abramowitz and I. A. Stegun, *Handbook of Mathematical Functions with Formulas, Graphs, and Mathematical Tables* (U.S. Goverment Printing Office, Washington, DC, 1972).

[35] J. M. Pereira, F. M. Peeters, and P. Vasilopoulos, Phys. Rev. B **76**, 115419 (2007).

[36] M. Nakamura, E. V. Castro, and B. Dóra, Phys. Rev. Lett. **103**, 266804 (2009).

[37] M. Koshino, T. Nakanishi, and T. Ando, Phys. Rev. B **82**, 205436 (2010).

[38] I. Romanovsky, C. Yannouleas, and U. Landman, Phys. Rev. B **83**, 045421 (2011).

[39] M. Kharitonov, Phys. Rev. Lett. **109**, 046803 (2012).

[40] M. Kharitonov, Phys. Rev. B **86**, 075450 (2012).

[41] R. T. Weitz, M. T. Allen, B. E. Feldman, J. Martin, and A. Yacoby, Science **330**, 812 (2010).

[42] J. Velasco, J., L. Jing, W. Bao, Y. Lee, P. Kratz, V. Aji, M. Bockrath, C. N. Lau, C. Varma, R. Stillwell, D. Smirnov, F. Zhang, J. Jung, and A. H. MacDonald, Nat. Nanotechnol. **7**, 156 (2012).

[43] P. Maher, C. R. Dean, A. F. Young, T. Taniguchi, K. Watanabe, K. L. Shepard, J. Hone, and P. Kim, Nat. Phys. **9**, 154 (2013).

[44] W. E. Boyce and R. C. DiPrima, *Elementary Differential Equations and Boundary Value Problems* (Wiley, New York, 2001).

[45] F. W. J. Olver, J. Res. Natl. Bur. Stand. B **63**, 131 (1959).

Chapter 3

Spectrum of edge states in the $\nu = 0$ quantum Hall phases in graphene

3.1 Introduction

[1] The unconventional sequence of the integer quantum Hall states at filling factors $\nu = \pm 4(n + 1/2)$, $n = 0, 1, 2, \ldots$ [2, 3], in graphene is a direct experimental manifestation of the Dirac quasiparticles [4, 5] and the fourfold (spin and valley) degeneracy of Landau levels (LLs) in this system. In high magnetic fields, however, the additional quantum Hall plateaux are observed [6–9], including the insulating state at the charge neutrality point ($\nu = 0$) [10, 11], which indicates the lifting of the LL degeneracy due to the Coulomb interactions. Several scenarios of the interaction-induced splitting of the lowest Landau level (LLL) leading to the $\nu = 0$ state have been proposed, including the charge density wave (CDW) [12–15], the Kekulé distortion (KD) [16, 17], the ferromagnetic (F) [18, 19], the antiferromagnetic (AF) [15, 20], and the canted antiferromagnetic (CAF) [21–24] phases. Whereas the bulk energy spectrum is gapped in all these phases, the differences in the edge transport can help to identify the nature of the ground state experimentally. Therefore, it is important to have an accurate theoretical description of the edge state properties for each phase.

Most of the existent studies of edge excitations in the $\nu = 0$ quantum Hall state take the simplified approach: the mean-field symmetry breaking potential is assumed to be constant across the sample area [18, 23, 25–28]. More rigorous treatment takes into account the modification of the order parameter at the edge [20, 29–32]. Both approaches predict the existence of the current-carrying gapless edge excitations in the F phase [18,20,29], which rules out this state in

---

[1] A version of this chapter has been published [1]

the case of a magnetic field perpendicular to the graphene plane, for which the divergent resistance was observed experimentally in Ref. [10,11] (see also Refs. [8,33]). The transition from an insulating to a metallic state, which occurs upon tilting the magnetic field [34], supports the scenario of transition between the CAF and F phases [23,31][2]. The absence of dispersing gapless edge states in the KD phase has been shown for the cases of a particular valley isospin orientation [28, 35] or the simplified confining boundary potential [27, 36]. The edge state spectrum of the armchair graphene ribbon in the CDW and AF phases, obtained numerically by the self-consistent Hartree-Fock calculations, was found to be gapped [20]. On the other hand, the analysis done within the continuum (Dirac) model showed that in the case of zigzag edges, the existence of gapless edge states depends on the ratio between the coexisting [37] chemical-potential-like symmetry breaking term and the corresponding mass gap (assumed to be constant) [25,26].

In this chapter, we present the systematic study of the edge excitations in the CDW, KD, AF, CAF, and F phases in the cases of ideal zigzag or armchair edges, using the effective Dirac Hamiltonian with constant mean-field symmetry breaking terms. We derive the dispersion equations for the edge states and find the analytic expressions for the corresponding wave functions, taking into account the finite next-to-nearest neighbor (NNN) hopping parameter.

Besides that, the edge state spectrum is also obtained numerically from the effective tight-binding model for noninteracting electrons where the symmetry-breaking potentials are introduced as the on-site energies and the imaginary NNN hopping parameters. This allows us to calculate the spectrum of edge states between the two valleys (in the case of zigzag edges), where it is not captured by the Dirac model. Within the simplified model, neglecting the modification of the order parameter near the edge, we formulate the most general criteria for the existence of gapless edge excitations for each considered phase and boundary type.

In the case of an armchair ribbon, the spectrum is found to be almost independent of the NNN hopping parameter. We find, in agreement with the previously reported results, that the band gap in the CDW and AF phases is equal to the bulk LLL splitting, and the transition from the CAF to F phase is accompanied by the edge-gap closure. For the KD phase, in general, the spectrum is gapped, however, the edge gap closes at some critical value of the valley isospin angle. This occurs due to the interplay between the bulk order and the effective infinite Kekulé mass at the boundary.

In the case of a zigzag ribbon, the finite NNN hopping parameter leads to the deformation of the edge state branch between the two valleys, which makes the energy spectrum gapless

---

[2] The authors of the recent Ref. [24] conclude that the inclusion of all filled LLs can essentially change the phase diagram in monolayer graphene in a magnetic field.

(provided the magnitude of the NNN hopping parameter exceeds the LLL splitting) in CDW, AF, CAF, and F phases. The only gapped phase is the KD state, where the edge gap is approximately equal to the half of the bulk LLL splitting. At zero NNN hopping, the spectrum is found to be gapped in the KD phase and gapless in the F phase, whereas for the CDW, AF, and CAF phases the band gap depends on the ratio between the corresponding mass gaps and the chemical-potential-like parameters.

The chapter is organized as follows. In Sec. 3.2 we describe the effective continuum mean-field model for the broken symmetry phases, the corresponding tight-binding models, formulate the boundary conditions, and derive the general form of the wave function in the arbitrary phase. The dispersion equations for edge states are written and analyzed numerically for each phase in Sec. 3.3. The discussion of the main results is given in Sec. 3.4. The expressions for the effective tight-binding Hamiltonians for zigzag and armchair graphene ribbons are provided in the Appendix.

3.2 Model and general solution

3.2.1 Dirac model with broken symmetry

We consider monolayer graphene subject to the external magnetic field $\mathbf{B} = \nabla \times \mathbf{A}$ that can be tilted with respect to the xy plane of the two-dimensional lattice (Fig. 3.1). The effective mean-field Hamiltonian is $H = H_0 + H_1$ with the free U(4)-symmetric part given by

$$H_0 = v_{\mathrm{F}}\sigma_0 \otimes \tilde{\tau}_0 \otimes (\tau_1\hat{\pi}_x + \tau_2\hat{\pi}_y). \tag{3.1}$$

Here $(\hat{\pi}_x, \hat{\pi}_y) = -i\hbar\nabla + (e/c)\mathbf{A}$ is the momentum operator (the electron charge is $-e < 0$), $v_{\mathrm{F}} = \sqrt{3}ta/(2\hbar) \simeq 10^6$ m/s is the Fermi velocity, $t \simeq 3$ eV is the nearest-neighbor (NN) hopping parameter, and $a \simeq 0.246$ nm is the lattice constant of graphene. The Pauli matrices σ_i, $\tilde{\tau}_i$, and τ_i, $i = 1, 2, 3$, act on the spin ($s = \pm$), valley ($K_\pm$), and sublattice (A and B) components of the wave function $\Psi = (\Psi^+_{K_+}, \Psi^+_{K_-}, \Psi^-_{K_+}, \Psi^-_{K_-})^\intercal$, respectively, where

$$\Psi^s_{K_+} = \begin{pmatrix} \Psi^s_{K_+A} \\ \Psi^s_{K_+B} \end{pmatrix}, \qquad \Psi^s_{K_-} = \begin{pmatrix} \Psi^s_{K_-B} \\ -\Psi^s_{K_-A} \end{pmatrix}, \tag{3.2}$$

and σ_0, $\tilde{\tau}_0$, τ_0 are the unit matrices. The basis spin states (the eigenstates of σ_3) correspond to the direction of the external magnetic field, which does not coincide with the z axis if the field

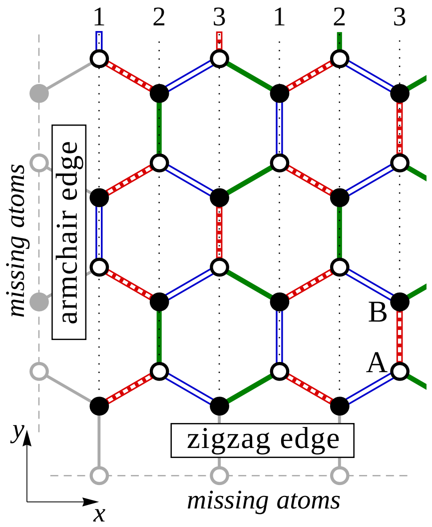

Figure 3.1: Graphene lattice with zigzag and armchair edges. Numbered vertical dotted lines label the three inequivalent atom types within each sublattice in the case of Kekulé order (the modulation of the NN hopping parameter is indicated by three different types of lines representing the NN bonds).

is tilted. The symmetry-breaking part H_1 has the general form

$$H_1^{\text{gen}} = \sum_{\alpha,\beta=0}^{3} \sigma_\alpha \otimes \tilde{\tau}_\beta \otimes (\tau_3 \Delta_{\alpha\beta} - \tau_0 \mu_{\alpha\beta}). \tag{3.3}$$

It includes the Zeeman splitting term $H_Z = \mu_Z \sigma_3 \otimes \tilde{\tau}_0 \otimes \tau_0$ with $\mu_Z = \mu_B B \approx 0.06\, B[\text{T}]$ meV and the dynamical part, which is mostly generated by the Coulomb interaction. The explicit form of this part depends on a given ground state determined by the interplay between the small lattice-scale asymmetric part of the Coulomb interactions, the Zeeman coupling, and the electron-phonon interactions [22].

In the absence of perpendicular magnetic field, parameters $\mu_{\alpha\beta}$ act like the chemical potentials shifting the Dirac cones for different spins and valleys, whereas the parameters $\Delta_{\alpha\beta}$ result in the (mass) gaps in the bulk spectrum. On the other hand, in the limit of a strong perpendicular magnetic field, within the projection on the LLL, these parameters appear only as a linear combination $\Delta_{\alpha\beta} + \mu_{\alpha\beta}$ and cause the same LLL splitting (but act differently on the higher LLs). However, even in high magnetic fields the edge state spectrum depends on the ratio between $\mu_{\alpha\beta}$ and $\Delta_{\alpha\beta}$ in the case of zigzag edges [25,26]. The coexistence of these two types of parameters is a general phenomenon and has been explicitly shown for the F and CDW phases in both monolayer [37] and bilayer [38] graphene (and also for AF phase in bilayer graphene [39]). We assume here that such a coexistence can also take place for CAF and KD phases. We also assume that the parameters $\mu_{\alpha\beta}$ and $\Delta_{\alpha\beta}$ are determined self-consistently for the infinite graphene sheet and do not vary near the edges of the system. In the following, we consider some specific cases of symmetry-broken phases.

In the mean-field symmetry breaking term

$$H_1^{\rm F} = \sigma_3 \otimes \tilde{\tau}_0 \otimes (\Delta' \tau_3 - \mu' \tau_0) \tag{3.4}$$

of the F phase, the finite spin polarization

$$\langle \Psi^\dagger \sigma_3 \otimes \tilde{\tau}_0 \otimes \tau_0 \Psi \rangle = \sum_{s,\xi=\pm} \sum_{X=A,B} s \langle (\Psi^s_{K_\xi X})^\dagger \Psi^s_{K_\xi X} \rangle \tag{3.5}$$

is described by the enhanced Zeeman splitting $-\mu' \gg \mu_{\rm Z}$. The coexisting order parameter

$$\langle \Psi^\dagger \sigma_3 \otimes \tilde{\tau}_0 \otimes \tau_3 \Psi \rangle = \sum_{s,\xi=\pm} s\xi \langle (\Psi^s_{K_\xi A})^\dagger \Psi^s_{K_\xi A} - (\Psi^s_{K_\xi B})^\dagger \Psi^s_{K_\xi B} \rangle, \tag{3.6}$$

which is dual to Δ', has the same form as the spin-orbit interaction [40]. Note that in Eq. (3.6), the two valleys contribute with the opposite signs; i.e., this order parameter is valley-odd.

The symmetry-breaking part of the Hamiltonian in the CAF phase,

$$H_1^{\rm CAF} = H_1^{\rm F} + H_1^{\rm AF}, \tag{3.7}$$

is characterized by the additional term

$$H_1^{\rm AF} = \sigma_1 \otimes \tilde{\tau}_3 \otimes (\tilde{\Delta} \tau_3 - \tilde{\mu} \tau_0), \tag{3.8}$$

where we have chosen the x spin axis along the antiferromagnetic vector that can have an arbitrary direction in the plane, perpendicular to the magnetic field [21, 22]. In the purely AF phase (which can exist only in the absence of Zeeman coupling or for the AF vector oriented along, rather then normally to, the magnetic field), the spin density imbalance between the sublattices A and B

$$\langle \Psi^\dagger \sigma_1 \otimes \tilde{\tau}_3 \otimes \tau_3 \Psi \rangle = \sum_{s,s',\xi=\pm} \sigma_1^{ss'} \langle (\Psi^s_{K_\xi A})^\dagger \Psi^{s'}_{K_\xi A} - (\Psi^s_{K_\xi B})^\dagger \Psi^{s'}_{K_\xi B} \rangle \tag{3.9}$$

connected with $\tilde{\Delta}$ coexists with the valley-odd order parameter

$$\langle \Psi^\dagger \sigma_1 \otimes \tilde{\tau}_3 \otimes \tau_0 \Psi \rangle = \sum_{s,s',\xi=\pm} \sum_{X=A,B} \xi \sigma_1^{ss'} \langle (\Psi^s_{K_\xi X})^\dagger \Psi^{s'}_{K_\xi X} \rangle, \tag{3.10}$$

which is dual to $\tilde{\mu}$.

In the CDW phase,

$$H_1^{\mathrm{CDW}} = \sigma_0 \otimes \tilde{\tau}_3 \otimes (\Delta \tau_3 - \mu \tau_0) + H_{\mathrm{Z}}, \tag{3.11}$$

the charge imbalance between the sublattices

$$\langle \Psi^\dagger \sigma_0 \otimes \tilde{\tau}_3 \otimes \tau_3 \Psi \rangle = \sum_{s,\xi=\pm} \langle (\Psi^s_{K_\xi A})^\dagger \Psi^s_{K_\xi A} - (\Psi^s_{K_\xi B})^\dagger \Psi^s_{K_\xi B} \rangle \tag{3.12}$$

described by the Dirac mass Δ coexists with the valley charge imbalance

$$\langle \Psi^\dagger \sigma_0 \otimes \tilde{\tau}_3 \otimes \tau_0 \Psi \rangle = \sum_{s,\xi=\pm} \sum_{X=A,B} \xi \langle (\Psi^s_{K_\xi X})^\dagger \Psi^s_{K_\xi X} \rangle \tag{3.13}$$

dual to the parameter μ.

The Hamiltonian of the KD phase with the symmetry-breaking term (we use the same variables Δ and μ as for the CDW phase)

$$H_1^{\mathrm{KD}} = \sigma_0 \otimes (\tilde{\tau}_1 \cos\theta + \tilde{\tau}_2 \sin\theta) \otimes (\Delta \tau_3 - \mu \tau_0) + H_{\mathrm{Z}} \tag{3.14}$$

is related to its CDW counterpart by the valley isospin rotation

$$H_0 + H_1^{\mathrm{KD}} = S (H_0 + H_1^{\mathrm{CDW}}) S^\dagger \tag{3.15}$$

with

$$S = \frac{1}{\sqrt{2}} \sigma_0 \otimes (\tilde{\tau}_0 + i\tilde{\tau}_1 \sin\theta - i\tilde{\tau}_2 \cos\theta) \otimes \tau_0, \tag{3.16}$$

where the parameter θ is the valley isospin angle describing the phase of the bond density wave.

3.2.2 Representation in the tight-binding model

The components of the Dirac wave function are related to the tight-binding amplitudes $\psi_s(\mathbf{R}_X)$ at the atomic sites $\mathbf{R}_A = \mathbf{n} \equiv n_1\mathbf{a}_1 + n_2\mathbf{a}_2$, $\mathbf{R}_B = \mathbf{n} + \boldsymbol{\delta}_i$ $(n_1, n_2 \in \mathbb{Z})$ by

$$\psi_s(\mathbf{R}_X) = \sum_{\xi=\pm} \Psi^s_{K_\xi X}(\mathbf{R}_X) e^{i\xi\mathbf{K}\cdot\mathbf{R}_X}, \tag{3.17}$$

where $\pm\mathbf{K} = (\pm 4\pi/(3a), 0)$ are the momenta corresponding to $K_\pm$ points, $\mathbf{a}_1 = (a/2, a\sqrt{3}/2)$, $\mathbf{a}_2 = (a/2, -a\sqrt{3}/2)$ are the lattice vectors, $\mathbf{a}_3 = -\mathbf{a}_1 - \mathbf{a}_2$, and the three vectors $\boldsymbol{\delta}_1 = (\mathbf{a}_1 - \mathbf{a}_2)/3$, $\boldsymbol{\delta}_2 = (\mathbf{a}_2 - \mathbf{a}_3)/3$, $\boldsymbol{\delta}_3 = (\mathbf{a}_3 - \mathbf{a}_1)/3$ connect the NN sites (Fig. 3.1).

The tight-binding Hamiltonian incorporating only the NN hopping terms is

$$\mathcal{H}_0 = -t \sum_{\mathbf{n}} \sum_{s=\pm} \sum_{i=1}^{3} (a^\dagger_{\mathbf{n}s} b_{\mathbf{n}+\boldsymbol{\delta}_i, s} + \text{H.c.}), \tag{3.18}$$

where $a_{\mathbf{R}_A,s}$ and $b_{\mathbf{R}_B,s}$ are Fermi operators corresponding to the atomic orbitals at the sites $\mathbf{R}_A$ and $\mathbf{R}_B$. In the continuum limit, it leads to the free Dirac Hamiltonian (3.1). The mean-field potentials specific to each phase can be introduced as

$$\begin{aligned}
\mathcal{H}_1^{\text{F}} &= -\mu'\Omega_3^+ - \Delta'\Lambda_3^-, \\
\mathcal{H}_1^{\text{AF}} &= \tilde{\Delta}\Omega_1^- + \tilde{\mu}\Lambda_1^+, \\
\mathcal{H}_1^{\text{CDW}} &= \Delta\Omega_0^- + \mu\Lambda_0^+ + \mathcal{H}_{\text{Z}}, \\
\mathcal{H}_{\text{Z}} &= \mu_{\text{Z}}\Omega_3^+,
\end{aligned} \tag{3.19}$$

where the valley-even symmetry breaking terms are represented by the on-site energies

$$\Omega^\pm_\alpha = \sum_{\mathbf{n}} \sum_{s,s'=\pm} \sigma_\alpha^{ss'} (a^\dagger_{\mathbf{n}s} a_{\mathbf{n}s'} \pm b^\dagger_{\mathbf{n}+\boldsymbol{\delta}_1,s} b_{\mathbf{n}+\boldsymbol{\delta}_1,s'}), \tag{3.20}$$

and the valley-odd potentials are accounted for by using the imaginary NNN hopping parameters [40–42]:

$$\Lambda^\pm_\alpha = 3^{-\frac{3}{2}} i \sum_{\mathbf{n}} \sum_{s,s'=\pm} \sum_{i=1}^{3} \sigma_\alpha^{ss'} (a^\dagger_{\mathbf{n}s} a_{\mathbf{n}+\mathbf{a}_i,s'} \pm b^\dagger_{\mathbf{n}+\boldsymbol{\delta}_1,s} b_{\mathbf{n}+\boldsymbol{\delta}_1+\mathbf{a}_i,s'} - \text{H.c.}). \tag{3.21}$$

For the KD phase, we use

$$\mathcal{H}_1^{\mathrm{KD}} = \sum_{\mathbf{n}} \sum_{s,\kappa=\pm} \sum_{i=1}^{3} \left(\frac{\Delta - \kappa\mu}{3} e^{i\kappa \mathbf{K}(2\mathbf{n}+\delta_i) - i\kappa\theta} a^\dagger_{\mathbf{n}s} b_{\mathbf{n}+\delta_i,s} + \text{H.c.} \right) + \mathcal{H}_Z, \tag{3.22}$$

where the real and imaginary modulations of the NN hopping t are described by the parameters Δ and μ, respectively. Note that the hopping parameters are constant along the directions of armchair edges (Fig. 3.1). As we will see in Sec. 3.3, in a low-energy Dirac model, the abrupt change of the NN hopping parameter from t to zero at the first missing row of bonds at the armchair edge can be viewed as an infinitely large Kekulé mass term at the boundary.

Finally, we consider the (real) NNN hopping term:

$$\mathcal{H}' = -t' \sum_{\mathbf{n}} \sum_{s=\pm} \sum_{i=1}^{3} (a^\dagger_{\mathbf{n}s} a_{\mathbf{n}+\mathbf{a}_i,s} + b^\dagger_{\mathbf{n}+\delta_1,s} b_{\mathbf{n}+\delta_1+\mathbf{a}_i,s} + \text{H.c.}). \tag{3.23}$$

As far as the bulk spectrum is concerned, this term adds a constant $3t'$ to the energy [43] (implicitly subtracted in what follows) and leads to the small LL shifts $\Delta E \sim t'a^2/l^2$ [44], where $l = \sqrt{\hbar c/(eB_\perp)}$ is the magnetic length.

The magnetic field is introduced in the tight-binding Hamiltonian by the Peierls substitution

$$c_i^\dagger c_j \to c_i^\dagger c_j \exp\left(\frac{ie}{\hbar c} \int_{\mathbf{r}_i}^{\mathbf{r}_j} d\mathbf{r} \cdot \mathbf{A} \right) \tag{3.24}$$

in the hopping terms corresponding to the transitions between the lattice sites $\mathbf{r}_i$ and $\mathbf{r}_j$.

3.2.3 Boundary conditions

For a zigzag ribbon $0 < y < W$, the tight-binding amplitudes vanish on the first missing rows of atoms (Fig. 3.1):

$$\psi_s(\mathbf{R}_A|_{y=0}) = \psi_s(\mathbf{R}_B|_{y=W}) = 0. \tag{3.25}$$

This condition uniquely defines the finite difference boundary problem in the case $t' = 0$ and translates, according to Eq. (3.17), into the boundary conditions [45]

$$\Psi^s_{K_\pm A}(x, 0) = \Psi^s_{K_\pm B}(x, W) = 0 \tag{3.26}$$

for the Dirac model, which also can be written as [46, 47]

$$\begin{aligned}(1 + \sigma_0 \otimes \tilde{\tau}_3 \otimes \tau_3)\Psi(x, 0) = 0, \\ (1 - \sigma_0 \otimes \tilde{\tau}_3 \otimes \tau_3)\Psi(x, W) = 0.\end{aligned} \tag{3.27}$$

In the case $t' \neq 0$, the tight-binding equations have to be supplemented with the condition that the amplitudes $\psi_s(\mathbf{R}_X)$ vanish also on the second missing rows of atoms, and the effective boundary conditions for the Dirac model in this case are [48, 49]

$$\begin{aligned}\Psi^s_{K_\pm A}(x, 0) = (t'/t)\Psi^s_{K_\pm B}(x, 0), \\ \Psi^s_{K_\pm B}(x, W) = (t'/t)\Psi^s_{K_\pm A}(x, W),\end{aligned} \tag{3.28}$$

or, equivalently,

$$\begin{aligned}[1 + \sigma_0 \otimes \tilde{\tau}_3 \otimes (\tau_3 \cos\vartheta - \tau_1 \sin\vartheta)]\Psi(x, 0) = 0, \\ [1 - \sigma_0 \otimes \tilde{\tau}_3 \otimes (\tau_3 \cos\vartheta + \tau_1 \sin\vartheta)]\Psi(x, W) = 0,\end{aligned} \tag{3.29}$$

where $\tan(\vartheta/2) = t'/t$.

For the armchair edge at $x = x_0$, the vanishing of the tight-binding amplitudes at the first missing row of atoms (Fig. 3.1),

$$\psi_s(\mathbf{R}_A|_{x=x_0}) = \psi_s(\mathbf{R}_B|_{x=x_0}) = 0, \tag{3.30}$$

implies, according to Eq. (3.17), the continuum model boundary condition [45]

$$\sum_{\xi=\pm} e^{i\xi\theta_0/2}\Psi^s_{K_\xi X}(x_0, y) = 0, \qquad X = A, B, \tag{3.31}$$

which can also be written as [46, 47]

$$[1 + \sigma_0 \otimes (\tilde{\tau}_2 \cos\theta_0 - \tilde{\tau}_1 \sin\theta_0) \otimes \tau_2]\Psi(x_0, y) = 0, \tag{3.32}$$

where the valley isospin angle $\theta_0 = 8\pi x_0/(3a)$ depends on the position of the edge. For a single edge (in the case of a half-plane), the factors $e^{\pm i\theta_0/2}$ in Eq. (3.31) change only the phases of the wave functions in each valley $K_{\xi=\pm}$ and thus are important only in the case of a narrow (compared to the magnetic length) ribbon when the boundary conditions at the opposite edges have to be taken into account simultaneously [45, 47] or when the valleys are coupled by the symmetry-breaking term of the bulk Hamiltonian (the KD phase).

3.2.4 General solution for the wave function

In the case of zigzag edges along the x axis, we choose the Landau gauge $(A_x, A_y) = (-B_\perp y, 0)$. The wave functions are plane waves in the x direction,

$$\Psi(\mathbf{r}) = e^{ikx}\Psi(\eta), \qquad \eta = y/l - kl, \tag{3.33}$$

and the Dirac equation acquires the form

$$\left[-\epsilon_0\sigma_0 \otimes \tilde{\tau}_0 \otimes (\tau_+\hat{a} + \tau_-\hat{a}^\dagger) + H_1^{\text{gen}} - E\right]\Psi(\eta) = 0, \tag{3.34}$$

where $\tau_\pm = (\tau_1 \pm i\tau_2)/2$ are projectors, $\hat{a} = 2^{-1/2}(\eta + \partial_\eta)$, $\hat{a}^\dagger = 2^{-1/2}(\eta - \partial_\eta)$ are the annihilation and creation operators, and $\epsilon_0 = \sqrt{2}\hbar v_F/l$ is the Landau energy scale. The general solution of this equation is given in terms of the parabolic cylinder functions $U(a, z)$ and $V(a, z)$ [50]:

$$\Psi^s_{K_\xi}(\eta) = \sum_i \left\{ \begin{pmatrix} C^{is\xi}_{U,1} U\left(\frac{1}{2} - \lambda^{s\xi}_i,\, \sqrt{2}\eta\right) \\ C^{is\xi}_{U,2} U\left(-\frac{1}{2} - \lambda^{s\xi}_i,\, \sqrt{2}\eta\right) \end{pmatrix} + \begin{pmatrix} C^{is\xi}_{V,1} V\left(\frac{1}{2} - \lambda^{s\xi}_i,\, \sqrt{2}\eta\right) \\ C^{is\xi}_{V,2} V\left(-\frac{1}{2} - \lambda^{s\xi}_i,\, \sqrt{2}\eta\right) \end{pmatrix} \right\}, \qquad s, \xi = \pm. \tag{3.35}$$

Substituting this solution into Eq. (3.34) and using the recurrence relations for the parabolic cylinder functions

$$\begin{aligned} \hat{a}U\left(-\tfrac{1}{2} - \lambda,\, \sqrt{2}\eta\right) &= \lambda U\left(\tfrac{1}{2} - \lambda,\, \sqrt{2}\eta\right), \\ \hat{a}^\dagger U\left(\tfrac{1}{2} - \lambda,\, \sqrt{2}\eta\right) &= U\left(-\tfrac{1}{2} - \lambda,\, \sqrt{2}\eta\right), \\ \hat{a}V\left(-\tfrac{1}{2} - \lambda,\, \sqrt{2}\eta\right) &= V\left(\tfrac{1}{2} - \lambda,\, \sqrt{2}\eta\right), \\ \hat{a}^\dagger V\left(\tfrac{1}{2} - \lambda,\, \sqrt{2}\eta\right) &= \lambda V\left(-\tfrac{1}{2} - \lambda,\, \sqrt{2}\eta\right) \end{aligned} \tag{3.36}$$

leads to the system of algebraic equations. Solving this system for each phase gives the correspondence between the coefficients $C^{is\xi}_{U,i}$, $C^{is\xi}_{V,i}$ and the energy dependence of parameters $\lambda^{s\xi}_i$.

In the following, we will often assume that the ribbon is wide enough ($W \gg l$) so that the bulk LLs are well formed and the states localized near each edge can be considered independently. In this case, one can use the solutions for the half planes $y > 0$ and $y < W$ instead of (3.35). On a semi-infinite plane $y > 0$, the normalizable wave functions contain only the parabolic cylinder functions $U(a,\, \sqrt{2}\eta)$ which are bounded at $\eta \to \infty$, and $C^{is\xi}_{V,j} = 0$. For the half plane $y < W$, the solution is given by

$$\Psi^s_{K_\xi}(\eta) = \sum_i \begin{pmatrix} -C^{is\xi}_{U,1} U(\frac{1}{2} - \lambda^{s\xi}_i, -\sqrt{2}\eta) \\ C^{is\xi}_{U,2} U(-\frac{1}{2} - \lambda^{s\xi}_i, -\sqrt{2}\eta) \end{pmatrix}. \tag{3.37}$$

The bulk solutions must be normalizable on an infinite plane and contain only the bounded at $\eta \to \pm\infty$ parabolic cylinder functions

$$U\Big(-\tfrac{1}{2} - n,\ \sqrt{2}\eta\Big) = 2^{-\frac{n}{2}} e^{-\frac{\eta^2}{2}} H_n(\eta), \quad n = 0, 1, 2, \ldots, \tag{3.38}$$

where $H_n(\eta)$ are the Hermite polynomials. This is possible when $\lambda^{s\xi}_i = n$ is a positive integer,

$$\Psi^s_{K_\xi}(\eta) = e^{-\frac{\eta^2}{2}} \begin{pmatrix} C^{s\xi}_1 H_{n-1}(\eta) \\ C^{s\xi}_2 H_n(\eta) \end{pmatrix}, \tag{3.39}$$

or when $\lambda^{s\xi}_i = 0$ and $C^{is\xi}_{U,1} = 0$,

$$\Psi^s_{K_\xi}(\eta) = e^{-\frac{\eta^2}{2}} \begin{pmatrix} 0 \\ C^{s\xi} H_0(\eta) \end{pmatrix}. \tag{3.40}$$

For the armchair edges along the y axis, we choose the gauge $(A_x, A_y) = (0, B_\perp x)$. The wave functions are plane waves in the y direction,

$$\Psi(\mathbf{r}) = e^{iky} \widetilde{\Psi}(\eta), \qquad \eta = x/l + kl, \tag{3.41}$$

and the Dirac equation becomes

$$\Big[-i\epsilon_0 \sigma_0 \otimes \tilde{\tau}_0 \otimes (\tau_+ \hat{a} - \tau_- \hat{a}^\dagger) + H^{\text{gen}}_1 - E\Big] \widetilde{\Psi}(\eta) = 0. \tag{3.42}$$

Its general solution can be obtained from the solution (3.35) of Eq. (3.34) by the unitary transformation

$$\widetilde{\Psi}(\eta) = \frac{1}{\sqrt{2}} \sigma_0 \otimes \tilde{\tau}_0 \otimes (\tau_0 + i\tau_3) \Psi(\eta), \tag{3.43}$$

which does not change the form of H^{gen}_1.

3.3 Spectra of edge states

3.3.1 CDW phase

The symmetry-breaking term (3.11) corresponding to the CDW order does not mix different spin ($s = \pm$) and valley ($\xi = \pm$) components that satisfy

$$[-\epsilon_0(\tau_+\hat{a} + \tau_-\hat{a}^\dagger) + \xi(\Delta\tau_3 - \mu\tau_0) - \mathcal{E}_s]\Psi^s_{K_\xi}(\eta) = 0, \tag{3.44}$$

where $\mathcal{E}_s = E - s\mu_Z$. The general solution is given by [25, 26]

$$\Psi^s_{K_\xi}(\eta) = C_U^{s\xi}\begin{pmatrix} \frac{\mathcal{E}_s+\xi(\mu+\Delta)}{\epsilon_0}U(\frac{1}{2} - \lambda^s_\xi,\, \sqrt{2}\eta) \\ -U(-\frac{1}{2} - \lambda^s_\xi,\, \sqrt{2}\eta) \end{pmatrix} + C_V^{s\xi}\begin{pmatrix} -V(\frac{1}{2} - \lambda^s_\xi,\, \sqrt{2}\eta) \\ \frac{\mathcal{E}_s+\xi(\mu-\Delta)}{\epsilon_0}V(-\frac{1}{2} - \lambda^s_\xi,\, \sqrt{2}\eta) \end{pmatrix}, \tag{3.45}$$

where

$$\lambda^s_\xi = \frac{(\mathcal{E}_s + \xi\mu)^2 - \Delta^2}{\epsilon_0^2}. \tag{3.46}$$

The bulk LLs, which correspond to the positive integer values of λ^s_ξ, are

$$\begin{aligned} E^{s\xi}_{n\pm} &= s\mu_Z - \xi\mu \pm \sqrt{\epsilon_0^2 n + \Delta^2}, \qquad n \geq 1, \\ E^{s\xi}_0 &= s\mu_Z - \xi(\mu + \Delta). \end{aligned} \tag{3.47}$$

Imposing zigzag boundary conditions (3.27) on the solution (3.45),

$$\begin{aligned} (\tau_0 + \xi\tau_3)\Psi^s_{K_\xi}(-kl) &= 0, \\ (\tau_0 - \xi\tau_3)\Psi^s_{K_\xi}(W/l - kl) &= 0, \end{aligned} \tag{3.48}$$

one obtains $\lambda^\pm_\xi = \lambda^\xi_n(k)$, where $\lambda = \lambda^+_n(k)$ is the nth root of the equation [26]

$$\begin{aligned} &\lambda U\Big(\tfrac{1}{2} - \lambda, -\sqrt{2}kl\Big)V\Big(-\tfrac{1}{2} - \lambda,\, \sqrt{2}(W/l - kl)\Big) \\ &\qquad - U\Big(-\tfrac{1}{2} - \lambda,\, \sqrt{2}(W/l - kl)\Big)V\Big(\tfrac{1}{2} - \lambda, -\sqrt{2}kl\Big) = 0, \end{aligned} \tag{3.49}$$

and $\lambda^-_n(k) = \lambda^+_n(W/l^2 - k)$. Using Eq. (3.46), we obtain the energy spectrum

$$E^{s\xi}_{n\pm}(k) = s\mu_Z - \xi\mu \pm \sqrt{\Delta^2 + \epsilon_0^2\lambda^\xi_n(k)}. \tag{3.50}$$

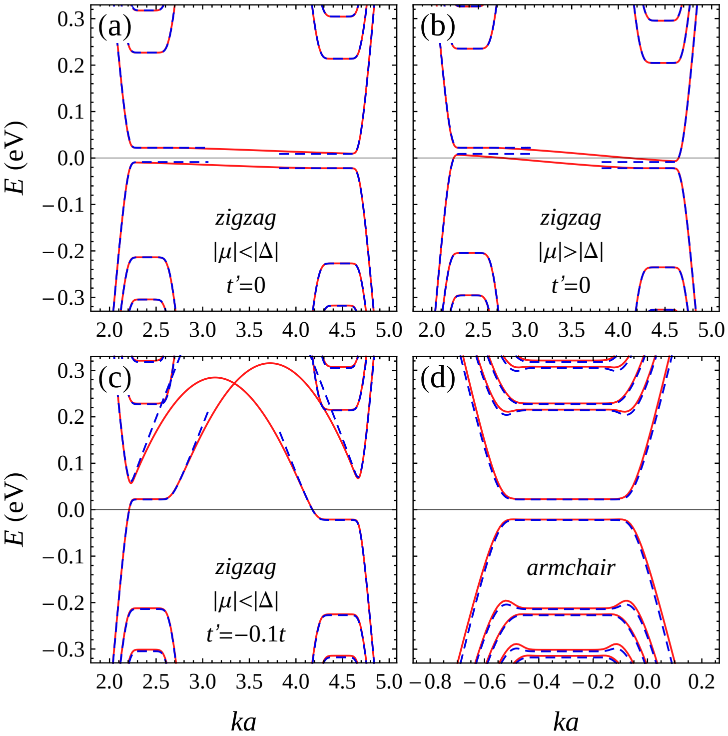

Figure 3.2: Spectrum of graphene ribbons of the width $W = 10l$ in perpendicular magnetic field $B_\perp = 40\,\mathrm{T}$ for the CDW phase calculated numerically within the tight-binding (solid line) and Dirac (dashed line) models. Values of parameters used here: (a), (c), (d) $\mu = 0.03\epsilon_0$, $\Delta = 0.07\epsilon_0$; (b) $\mu = 0.07\epsilon_0$, $\Delta = 0.03\epsilon_0$. For the armchair ribbon, the NNN hopping $t' = -0.1t$ is taken into account only in the tight-binding calculations. The overall energy shift of $3t'$ is subtracted and the Zeeman splitting is neglected.

The lowest solution $\lambda_0^+(k)$ is a monotonically increasing function with $\lambda_0^+(k \to -\infty) \to 0$ [26]. This implies that the gap in the energy spectrum is

$$E_{\mathrm{gap}} = 2(|\Delta| - |\mu| - \mu_Z) \tag{3.51}$$

[Fig. 3.2(a)]. In the case $E_{\mathrm{gap}} < 0$, the gapless edge states are present. There is a pair of such states of the same spin that counterpropagate at each edge, and the Dirac model captures only one gapless state from each pair [Fig. 3.2(b)]. The other gapless states are located on the edge state branches connecting the two valleys [51,52], which have a finite dispersion at nonzero μ.

In the case of a finite NNN hopping, applying the boundary conditions (3.29) to the solution (3.45),

$$\begin{aligned}&[\tau_0 + \xi(\tau_3 \cos\vartheta - \tau_1 \sin\vartheta)]\Psi^s_{K_\xi}(-kl) = 0,\\ &[\tau_0 - \xi(\tau_3 \cos\vartheta + \tau_1 \sin\vartheta)]\Psi^s_{K_\xi}(W/l - kl) = 0,\end{aligned} \tag{3.52}$$

leads to the dispersion equation

$$\frac{\mathcal{E}_s \pm (\mu + \Delta)}{\epsilon_0} U\Big(\tfrac{1}{2} - \lambda^s_\pm, -\sqrt{2}kl\Big) \pm (t'/t)^{\pm 1} U\Big(-\tfrac{1}{2} - \lambda^s_\pm, -\sqrt{2}kl\Big) = 0. \tag{3.53}$$

for the edge $y = 0$ in the valley $K_\pm$. The corresponding equation for the edge $y = W$ is

$$\frac{\mathcal{E}_s \pm (\mu + \Delta)}{\epsilon_0} U\Big(\tfrac{1}{2} - \lambda^s_\pm, \sqrt{2}(kl - W/l)\Big) \mp (t'/t)^{\mp 1} U\Big(-\tfrac{1}{2} - \lambda^s_\pm, \sqrt{2}(kl - W/l)\Big) = 0. \tag{3.54}$$

Here we have used $C^{s\xi}_V = 0$ for the solution on a half plane $y > 0$ and took into account Eq. (3.37) for the solution on a half plane $y < W$.

At finite t', the edge state branches between the two valleys are dispersive. Indeed, within the Dirac model, these edge modes approach the linear asymptotes

$$\begin{aligned}E^{s\xi}_{y=0} &\simeq s\mu_Z - \xi\mu - \Delta\cos\vartheta + \xi\hbar v_F k \sin\vartheta,\\ E^{s\xi}_{y=W} &\simeq s\mu_Z - \xi\mu + \Delta\cos\vartheta + \xi\hbar v_F (k - W/l^2)\sin\vartheta,\end{aligned} \tag{3.55}$$

which can be obtained from dispersion equations (3.53)–(3.54) by using the asymptotic formula [53, 54]

$$\frac{U\Big(\tfrac{1}{2} - \lambda, -\sqrt{2}kl\Big)}{U\Big(-\tfrac{1}{2} - \lambda, -\sqrt{2}kl\Big)} \simeq -\frac{kl + \sqrt{k^2l^2 - 2\lambda}}{\sqrt{2}\lambda}, \tag{3.56}$$

for $\lambda \gg |kl| \gg 1$ (it breaks down at $k > 0$, $\lambda \simeq n$, $n \in \mathbb{Z}$, which corresponds to the avoided crossings with the bulk LLs). Equation (3.55) agrees with the previously obtained dispersion of the corresponding edge modes at zero magnetic field [49, 55]. This result from the Dirac model is a good approximation only in the vicinity of the $K_\pm$ points, and from the tight-binding calculations we see that these edge modes, in fact, attain their maxima between the two valleys [Fig. 3.2(c)]. In the absence of the symmetry-breaking parameters μ, Δ, and μ_Z, the maximum deviation from the LLL energy is equal to $-t'$ and corresponds to the state which is localized exclusively on the outermost row of atoms [43] (it can be easily shown that the effect of experimentally accessible magnetic fields on this state is negligible). Therefore, this edge state branch closes the spectrum gap (if present) provided that $|\Delta/t'| \lesssim 1/2$. This condition is expected to be satisfied even for the highest accessible magnetic fields ($B \lesssim 50$ T).

Indeed, the magnitude of the NNN hopping parameter $t' \simeq -0.3$ eV [44] exceeds the energy scale $e^2/(\varepsilon_g \varepsilon_s l) \sim 0.01\sqrt{B_\perp[\mathrm{T}]}$ eV of the Coulomb interactions responsible for the LLL splitting, where the dielectric constants $\varepsilon_g = 1 + \pi e^2/(2\hbar\varepsilon_s v_F)$ and ε_s describe the intrinsic and the substrate-induced screening, respectively [36].

In the case of a half plane with the armchair edge at $x = x_0$, the boundary condition (3.32) can be rewritten, using Eq. (3.43), as

$$(1 - \tilde{\tau}_2 \otimes \tau_1) \begin{pmatrix} \Psi^s_{K_+} \\ e^{-i\theta_0} \Psi^s_{K_-} \end{pmatrix}_{\eta = kl + x_0/l} = 0. \tag{3.57}$$

Substituting the solution (3.45) into this equation with $x_0 = 0$ gives the dispersion equation [25]

$$F_1\left(\mathcal{E}_s, \sqrt{2}kl\right) = 0, \tag{3.58}$$

where

$$F_1(\mathcal{E}_s, z) \equiv \frac{\mathcal{E}_s^2 - (\mu + \Delta)^2}{\epsilon_0^2} U\left(\tfrac{1}{2} - \lambda^s_+, z\right) U\left(\tfrac{1}{2} - \lambda^s_-, z\right) - U\left(-\tfrac{1}{2} - \lambda^s_+, z\right) U\left(-\tfrac{1}{2} - \lambda^s_-, z\right), \tag{3.59}$$

and λ^s_ξ are defined in Eq. (3.46). The dispersion equation for a half plane $x < W$,

$$F_1\left(\mathcal{E}_s, -\sqrt{2}(kl + W/l)\right) = 0, \tag{3.60}$$

will be used for the spectrum at the opposite edge of the wide ribbon. At $\mu = 0$, Eq. (3.58) reduces to the equation [25]

$$\lambda\, U^2\left(\tfrac{1}{2} - \lambda, \sqrt{2}kl\right) - U^2\left(-\tfrac{1}{2} - \lambda, \sqrt{2}kl\right) = 0 \tag{3.61}$$

for $\lambda^s_+ = \lambda^s_- = \lambda$, which has the solutions $\lambda = \widetilde{\lambda}_n(k)$. Taking into account that the lowest solution $\widetilde{\lambda}_0(k)$ is a monotonic function and $\widetilde{\lambda}_0(k \to -\infty) \to 0$, we see that the spectrum

$$E^s_{n\pm}(k) = s\mu_Z \pm \sqrt{\Delta^2 + \epsilon_0^2 \widetilde{\lambda}_n(k)} \tag{3.62}$$

has a gap of $2(|\Delta| - \mu_Z)$. In the case of a finite μ, we find numerically that although the lowest energy solution of dispersion equation (3.58) can be nonmonotonic, the spectrum gap is still very close to the bulk LLL splitting,

$$E_{\mathrm{gap}} \simeq 2(|\Delta + \mu| - \mu_Z), \tag{3.63}$$

provided that $|\mu| \ll \epsilon_0$ [Fig. 3.2(d)]. The effect of the NNN hopping on the edge gap is also found to be very small if $|t'/t| \ll 1$.

3.3.2 KD phase

The symmetry-breaking term (3.14) of the KD phase mixes the two valleys but leaves the spin components ($s = \pm$) uncoupled:

$$\Big[-\epsilon_0 \tilde{\tau}_0 \otimes (\tau_+ \hat{a} + \tau_- \hat{a}^\dagger) + (\tilde{\tau}_1 \cos\theta + \tilde{\tau}_2 \sin\theta) \otimes (\Delta\tau_3 - \mu\tau_0) - \mathcal{E}_s\Big]\Psi_s^{\mathrm{KD}}(\eta) = 0. \tag{3.64}$$

The general solution $\Psi_s^{\mathrm{KD}}(\eta) \equiv [\Psi_{K_+}^{s,\mathrm{KD}}(\eta), \Psi_{K_+}^{s,\mathrm{KD}}(\eta)]^T$ of the above equation is obtained from the solution $\Psi_s(\eta) \equiv [\Psi_{K_+}^s(\eta), \Psi_{K_+}^s(\eta)]^T$ for the CDW phase (3.45) by the valley isospin rotation (3.16), and the bulk energy spectrum is identical to the spectrum (3.47) of the CDW phase. Imposing the zigzag boundary conditions (3.27) on the solution of Eq. (3.64), one gets the equations

$$\begin{aligned} &(1 + \tilde{\tau}_3 \otimes \tau_3)\Psi_s^{\mathrm{KD}}(-kl) = 0, \\ &(1 - \tilde{\tau}_3 \otimes \tau_3)\Psi_s^{\mathrm{KD}}(W/l - kl) = 0, \end{aligned} \tag{3.65}$$

which are equivalent to the equations

$$\begin{aligned} &[1 - (\tilde{\tau}_1 \cos\theta + \tilde{\tau}_2 \sin\theta) \otimes \tau_3]\Psi_s(-kl) = 0, \\ &[1 + (\tilde{\tau}_1 \cos\theta + \tilde{\tau}_2 \sin\theta) \otimes \tau_3]\Psi_s(W/l - kl) = 0, \end{aligned} \tag{3.66}$$

in terms of the solution (3.45) for the CDW phase. The resulting dispersion equation for a zigzag ribbon,

$$\det\begin{pmatrix} Z_+(-kl) & Z_+(W/l - kl) \\ -Z_-(-kl) & Z_-(W/l - kl) \end{pmatrix} = 0, \tag{3.67}$$

with the 2×2 blocks $Z_\pm(\eta)$ defined as

$$Z_\pm(\eta) = \begin{pmatrix} \frac{\mathcal{E}_s \pm \mu \pm \Delta}{\epsilon_0} U(\frac{1}{2} - \lambda_\pm^s, \sqrt{2}\eta) & \pm U(-\frac{1}{2} - \lambda_\pm^s, \sqrt{2}\eta) \\ V(\frac{1}{2} - \lambda_\pm^s, \sqrt{2}\eta) & \frac{\mu - \Delta \pm \mathcal{E}_s}{\epsilon_0} V(-\frac{1}{2} - \lambda_\pm^s, \sqrt{2}\eta) \end{pmatrix} \tag{3.68}$$

and $\lambda_\pm^s$ given by Eq. (3.46), is independent of the angle θ.

The spectrum, shown in Fig. 3.3(a), has two dispersionless (in the limit $W \gg l$) edge modes $E = \pm\mu_Z$ [35, 56], which lie inside the bulk gap (assuming $2\mu_Z < |\mu + \Delta|$).

In the case $t' \neq 0$, the modified zigzag boundary conditions (3.29) applied to the solution

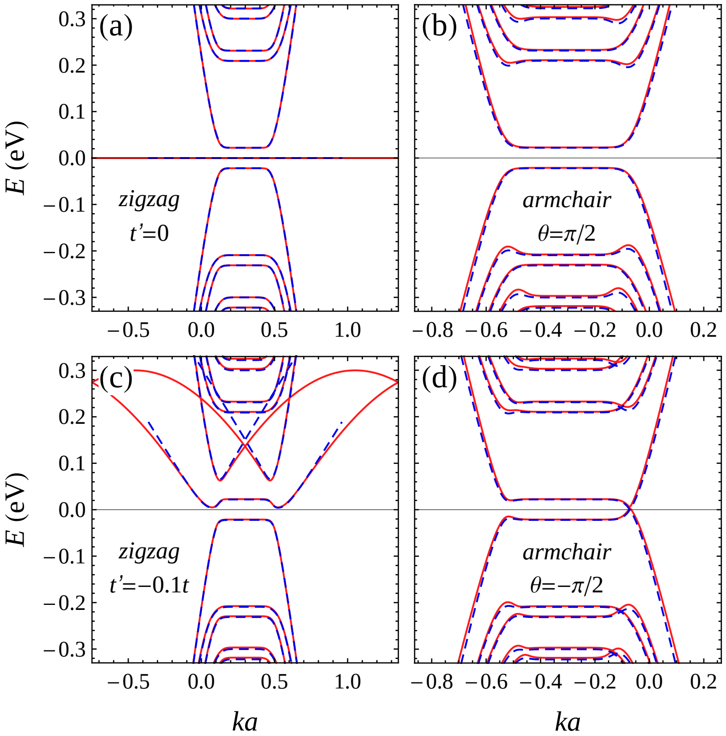

Figure 3.3: Spectrum of graphene ribbons of the width $W = 10l$ in perpendicular magnetic field $B_\perp = 40\,\mathrm{T}$ for the KD phase calculated numerically within the tight-binding (solid line) and Dirac (dashed line) models. Values of parameters used here: $\mu = \Delta = 0.05\epsilon_0$. For the armchair ribbon ($N = 333$), the NNN hopping $t' = -0.1t$ is taken into account only in the tight-binding calculations. The overall energy shift of $3t'$ is subtracted and the Zeeman splitting is neglected.

at $y = 0$,

$$[1 - (\tilde{\tau}_1 \cos\theta + \tilde{\tau}_2 \sin\theta) \otimes (\tau_3 \cos\vartheta - \tau_1 \sin\vartheta)]\Psi_s(-kl) = 0, \tag{3.69}$$

lead to the dispersion equation

$$F_2^{(0)}\left(\mathcal{E}_s, -\sqrt{2}kl\right) - \tan(\vartheta) F_1\left(\mathcal{E}_s, -\sqrt{2}kl\right) = 0, \tag{3.70}$$

where $F_1(\mathcal{E}_s, z)$ is defined in Eq. (3.59) and

$$F_2^{(n)}(\mathcal{E}_s, z) \equiv \sum_{\xi=\pm} (\xi)^n \frac{\mathcal{E}_s + \xi(\mu + \Delta)}{\epsilon_0} U\left(\tfrac{1}{2} - \lambda^s_\xi, z\right) U\left(-\tfrac{1}{2} - \lambda^s_{-\xi}, z\right). \tag{3.71}$$

The dispersion equation for the edge $y = W$ is obtained from Eq. (3.70) by replacing $k \to W/l^2 - k$. The edge modes are not dispersionless at $t' \neq 0$, but in contrast to the CDW phase, the finite edge gap approximately equal to the half of the bulk gap remains even at $|t'| \gg |\mu|, |\Delta|$

[Fig. 3.3(c)]. In fact, one can easily check that Eq. (3.70) does not have solution $\mathcal{E}_s = 0$ at $t' \neq 0$; thus the edge gap is always larger than the half of the bulk gap. In the case $\mu = 0$, one can also obtain analytically the ratio between the edge and the bulk gaps:

$$\frac{E_{\text{gap}}}{2|\Delta|} = \frac{1 + |\sin\vartheta|}{2}. \tag{3.72}$$

In the case $t' = \mu = 0$, one has $\lambda_+^s = \lambda_-^s$ and Eq. (3.70) simplifies to

$$\mathcal{E}_s U\Big(-\frac{1}{2} - \frac{\mathcal{E}_s^2 - \Delta^2}{\epsilon_0^2}, -\sqrt{2}kl\Big) U\Big(\frac{1}{2} - \frac{\mathcal{E}_s^2 - \Delta^2}{\epsilon_0^2}, -\sqrt{2}kl\Big) = 0. \tag{3.73}$$

In Ref. [28], only the solutions corresponding to the third factor on the left-hand side of the above equation were found.

For the armchair edge $x = x_0$, the boundary condition (3.32) can be written as

$$[1 + (\tilde{\tau}_2 \cos\theta_0 - \tilde{\tau}_1 \sin\theta_0) \otimes \tau_2] \widetilde{\Psi}_s^{\text{KD}}(kl + x_0/l) = 0, \tag{3.74}$$

or, using Eqs. (3.43) and (3.16),

$$\Big\{1 + [(\tilde{\tau}_1 \sin\theta - \tilde{\tau}_2 \cos\theta)\cos(\theta - \theta_0) - \tilde{\tau}_3 \sin(\theta - \theta_0)] \otimes \tau_1\Big\} \Psi_s(kl + x_0/l) = 0, \tag{3.75}$$

in terms of the solutions for the CDW phase. For the half plane $x > 0$, we use the solution (3.45) with $C_V^{s\xi} = 0$, which leads to the dispersion equation

$$F_1\big(\mathcal{E}_s, \sqrt{2}kl\big) - \sin(\theta) F_2^{(1)}\big(\mathcal{E}_s, \sqrt{2}kl\big) = 0. \tag{3.76}$$

In the case $\sin\theta = 0$, it simplifies to the corresponding dispersion equation (3.58) for the CDW phase, in particular, for $\mu = 0$ it reduces to Eq. (3.61) [28]. At $\theta = \pm\pi/2$, Eq. (3.76) can be factorized into two equations:

$$\frac{\xi\mathcal{E}_s + \mu + \Delta}{\varepsilon_0} U\big(\tfrac{1}{2} - \lambda_\xi^s, \sqrt{2}kl\big) \pm U\big(-\tfrac{1}{2} - \lambda_\xi^s, \sqrt{2}kl\big) = 0, \tag{3.77}$$

where $\xi = \pm$ correspond to the eigenstates of the valley isospin matrix $\tilde{\tau}_2$. In particular, when $\theta = \theta_{\text{cr}}$ with the critical angle

$$\theta_{\text{cr}} = -\operatorname{sgn}(\mu + \Delta)\frac{\pi}{2}, \tag{3.78}$$

Eq. (3.77) has a solution $\mathcal{E}_s = 0$ for each $\xi = \pm$ and the spectrum is gapless [Fig. 3.3(d)]. In the case $\mu = 0$, one can obtain analytically from Eq. (3.76) the θ dependence of the ratio between

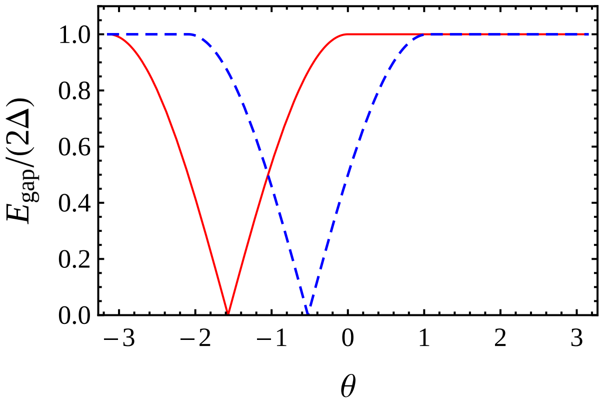

Figure 3.4: Edge gap at $x = 0$ (solid line) and $x = W$ (dashed line) in an armchair ribbon as a function of the valley isospin orientation of the KD order parameter. Here $\mu = \mu_Z = t' = 0$ and $N = 3n$, $n \in \mathbb{Z}$. For $N = 3n \pm 1$, the dashed curve is shifted horizontally with $\theta \to \theta \mp 2\pi/3$.

the edge and the bulk gaps (Fig. 3.4):

$$\frac{E_{\mathrm{gap}}}{2|\Delta|} = \begin{cases} |\cos\theta|, & \Delta\sin\theta < 0, \\ 1, & \Delta\sin\theta > 0. \end{cases} \tag{3.79}$$

Qualitatively similar behavior (with Δ replaced by $\Delta+\mu$) is observed numerically for $\mu \neq 0$. At nonzero μ_Z, the spectrum is gapless for a finite range of θ, namely, when $|\theta - \theta_{\mathrm{cr}}| \lesssim \mu_Z/|\Delta + \mu|$.

For the edge $x = W$, applying the boundary condition (3.75) to the corresponding solution for a half plane $x < W$ [see Eq. (3.37)] yields Eq. (3.76) with $k \to -k - W/l^2$, $\theta \to \theta_W - \theta$, where

$$\theta_W = \frac{8\pi W}{3a} = \frac{4\pi(N+1)}{3}, \tag{3.80}$$

and the dispersion equation is written as

$$F_1\Big(\mathcal{E}_s, -\sqrt{2}(kl + W/l)\Big) + \sin\Big(\theta + \tfrac{2\pi m}{3}\Big)F_2^{(1)}\Big(\mathcal{E}_s, -\sqrt{2}(kl + W/l)\Big) = 0. \tag{3.81}$$

Here $m = 0, \pm 1$ depends on the number of atoms N across the ribbon, $N+1 = 3n+m$, $n \in \mathbb{Z}$. For the edge $x = W$, the critical angle at which Eq. (3.81) has solution $\mathcal{E}_s = 0$ is $\theta'_{\mathrm{cr}} = -\theta_{\mathrm{cr}} - 2\pi m/3$. This implies that the spectrum cannot be gapless at both edges simultaneously (Fig. 3.4).

Edge-gap closing at a critical valley isospin angle of the KD order parameter was recently pointed out in a tight-binding study of Ref. [56] at $B = 0$. In the case of a strong magnetic field, this phenomenon can be simply understood by noticing that the armchair boundary condition (3.32) is equivalent to the infinite Kekulé mass boundary term (rather than the infinite

Dirac mass boundary condition commonly used in graphene [57–59])

$$V_{\text{conf}}(x) = n_x M(x) \sigma_0 \otimes (\tilde{\tau}_2 \cos\theta_0 - \tilde{\tau}_1 \sin\theta_0) \otimes \tau_3, \tag{3.82}$$

which confines the motion of electrons to the region $n_x(x - x_0) < 0$, where $M(x) = M_0 \Theta(n_x(x - x_0))$, $n_x = \pm 1$ is the x component of the outward unit vector normal to the boundary, $\Theta(x)$ is the Heaviside step function, and $M_0 \to +\infty$. Indeed, for a two-component spinor the confining Berry-Mondragon mass term $M(x)\tau_3$ implies the boundary condition $(1 - n_x \tau_2)\Psi^s_{K_\xi}(x_0, y) = 0$ [60], from which the armchair boundary condition (3.32) is obtained by adding the valley matrix structure $\tilde{\tau}' \equiv \tilde{\tau}_2 \cos\theta_0 - \tilde{\tau}_1 \sin\theta_0$. In the absence of valley symmetry breaking in the bulk, $V_{\text{conf}}(x)$ produces the edge splitting of LLs that correspond to the different $\tilde{\tau}'$ eigenstates [23, 29, 61]. The spatially homogeneous LLL splitting of the same valley components is caused by the KD symmetry-breaking term (3.14) with $\theta = \theta_0 \pm \pi/2$. In particular, when $\theta = \theta_0 \pm n_x \theta_{\text{cr}}$, the constant bulk and growing near the edge boundary contributions have the opposite signs and cancel each other at some distance from the edge; i.e., the gap closes.

Note that in the case of a smooth confining Dirac mass potential $\widetilde{V}_{\text{conf}}(y) = V(y)\sigma_0 \otimes \tilde{\tau}_3 \otimes \tau_3$, the edge state spectrum of the KD phase was found to be gapped [27, 36]. For this type of boundary one should expect, by the same argument, that the spectrum is gapless in the CDW phase with the appropriate sign of $\Delta + \mu$. Indeed, for the abruptly changing at $y = 0$ potential $V(y) = M_0 \Theta(-y)$, which is equivalent to imposing the boundary conditions $(1 - \xi\tau_1)\Psi^s_{K_\xi}(-kl) = 0$ on the solution (3.52) with $C^{s\xi}_V = 0$, one obtains in the K_ξ valley the same dispersion equation (3.77) with the upper sign.

3.3.3 AF, CAF, and F phases

While we consider the Hamiltonian (3.7) of the CAF phase in general, the F and AF phases are treated as the special cases with $\tilde{\Delta} = \tilde{\mu} = 0$ and $\Delta' = \mu' = 0$, respectively. The valley components $\Psi_{K_\xi}(\eta) = [\Psi^+_{K_\xi}(\eta), \Psi^-_{K_\xi}(\eta)]^T$ decouple and the energy eigenvalue equation for each valley ($\xi = \pm$) reads

$$\left[-\epsilon_0 \sigma_0 \otimes (\tau_+ \hat{a} + \tau_- \hat{a}^\dagger) + \sigma_3 \otimes (\Delta' \tau_3 - \mu' \tau_0) + \xi \sigma_1 \otimes (\tilde{\Delta} \tau_3 - \tilde{\mu} \tau_0) - E\right] \Psi_{K_\xi}(\eta) = 0. \tag{3.83}$$

The general solution is given by

$$\Psi_{K_\xi}(\eta) = \sum_{\kappa=\pm}\left\{C_U^{\kappa\xi}\begin{pmatrix} a_\kappa^+ U(\frac{1}{2}-\lambda_\kappa,\, \sqrt{2}\eta) \\ -b_\kappa U(-\frac{1}{2}-\lambda_\kappa,\, \sqrt{2}\eta) \\ \xi c_\kappa^+ U(\frac{1}{2}-\lambda_\kappa,\, \sqrt{2}\eta) \\ \xi d^+ U(-\frac{1}{2}-\lambda_\kappa,\, \sqrt{2}\eta) \end{pmatrix} + C_V^{\kappa\xi}\begin{pmatrix} b_\kappa V(\frac{1}{2}-\lambda_\kappa,\, \sqrt{2}\eta) \\ -a_\kappa^- V(-\frac{1}{2}-\lambda_\kappa,\, \sqrt{2}\eta) \\ \xi d^- V(\frac{1}{2}-\lambda_\kappa,\, \sqrt{2}\eta) \\ \xi c_\kappa^- V(-\frac{1}{2}-\lambda_\kappa,\, \sqrt{2}\eta) \end{pmatrix}\right\}, \tag{3.84}$$

where we introduced

$$\begin{aligned} a_\kappa^\pm &= (E \pm \Delta' - \mu')g^\pm - (E \pm \Delta' + \mu')\epsilon_0^2\lambda_\kappa, \\ b_\kappa &= \epsilon_0[(E-\mu')^2 - \Delta'^2 - \tilde{\Delta}^2 + \tilde{\mu}^2 - \epsilon_0^2\lambda_\kappa], \\ c_\kappa^\pm &= (\tilde{\Delta} \mp \tilde{\mu})g^\pm - (\tilde{\Delta} \pm \tilde{\mu})\epsilon_0^2\lambda_\kappa, \\ d^\pm &= 2\epsilon_0[\tilde{\mu}(\Delta' \pm E) - \mu'\tilde{\Delta}], \\ g^\pm &= E^2 - (\mu' \pm \Delta')^2 - (\tilde{\mu} \pm \tilde{\Delta})^2, \end{aligned} \tag{3.85}$$

and

$$\lambda_\pm = \frac{1}{\epsilon_0^2}\left(E^2 + \mu'^2 + \tilde{\mu}^2 - \Delta'^2 - \tilde{\Delta}^2 \pm 2\sqrt{E^2(\mu'^2 + \tilde{\mu}^2) - (\mu'\tilde{\Delta} - \tilde{\mu}\Delta')^2}\right). \tag{3.86}$$

The bulk LLs corresponding to the positive integer values of λ_κ are

$$\begin{aligned} E_{n\pm}^\kappa &= \pm\left[\beta^2 + \left(\alpha + \kappa\sqrt{\gamma^2 + \epsilon_0^2 n}\right)^2\right]^{1/2}, \qquad \kappa = \pm, \quad n \geq 1, \\ E_{0\pm} &= \pm\sqrt{(\mu' + \Delta')^2 + (\tilde{\mu} + \tilde{\Delta})^2}, \end{aligned} \tag{3.87}$$

where

$$\begin{aligned} \alpha &= \sqrt{\mu'^2 + \tilde{\mu}^2}, \\ \beta &= (\mu'\tilde{\Delta} - \tilde{\mu}\Delta')/\alpha, \\ \gamma &= (\mu'\Delta' + \tilde{\mu}\tilde{\Delta})/\alpha. \end{aligned} \tag{3.88}$$

Note that the ferromagnetic parameter μ' includes the bare Zeeman splitting μ_Z. In the special case when the valley-odd potentials are absent ($\tilde{\mu} = \Delta' = 0$), the bulk spectrum (3.87) reduces to [21,23,24]

$$\begin{aligned} E_{n\pm}^\kappa &= \pm\sqrt{\tilde{\Delta}^2 + (|\mu'| + \kappa\epsilon_0\sqrt{n})^2}, \quad n \geq 1, \\ E_{0\pm} &= \pm\sqrt{\tilde{\Delta}^2 + \mu'^2}. \end{aligned} \tag{3.89}$$

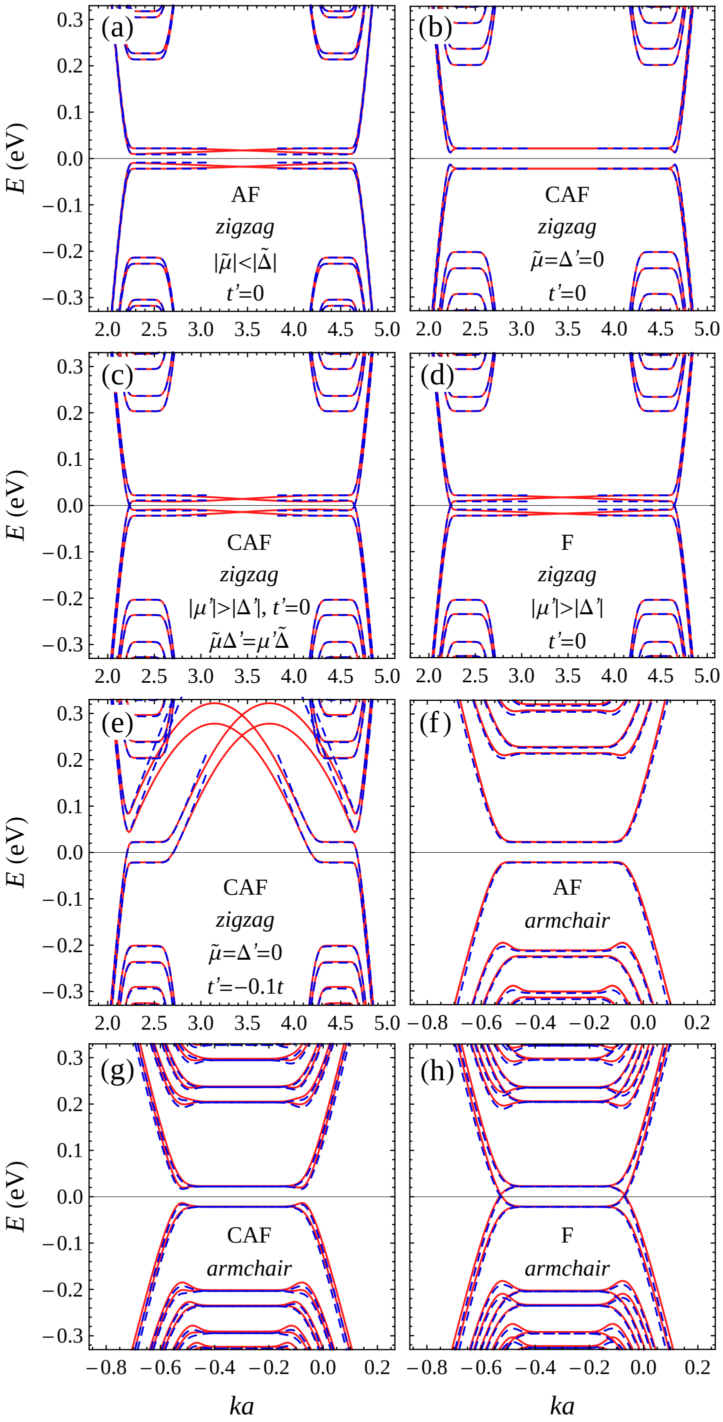

Figure 3.5: Spectrum of graphene ribbons of the width $W = 10l$ in perpendicular magnetic field $B_\perp = 40\,\mathrm{T}$ for the AF, CAF, and F phases calculated numerically within the tight-binding (solid line) and Dirac (dashed line) models. Values of parameters used here: (a), (f) $\mu' = \Delta' = 0$, $\tilde{\mu} = 0.03\epsilon_0$, $\tilde{\Delta} = 0.07\epsilon_0$; (b), (e) $\tilde{\mu} = \Delta' = 0$, $\mu' = -0.08\epsilon_0$, $\tilde{\Delta} = 0.06\epsilon_0$; (c), (g) $\mu' = -0.045\epsilon_0$, $\Delta' = -0.015\epsilon_0$, $\tilde{\mu} = 0.06\epsilon_0$, $\tilde{\Delta} = 0.02\epsilon_0$; (d), (h) $\tilde{\mu} = \tilde{\Delta} = 0$, $\mu' = -0.07\epsilon_0$, $\Delta' = -0.03\epsilon_0$. For the armchair ribbon, the NNN hopping $t' = -0.1t$ is taken into account only in the tight-binding calculations. The overall energy shift of $3t'$ is subtracted.

Imposing the zigzag boundary conditions (3.27) at the two edges of the ribbon,

$$\begin{aligned} &\sigma_0 \otimes (\tau_0 + \xi\tau_3)\Psi^s_{K_\xi}(-kl) = 0, \\ &\sigma_0 \otimes (\tau_0 - \xi\tau_3)\Psi^s_{K_\xi}(W/l - kl) = 0, \end{aligned} \tag{3.90}$$

one arrives at two identical equations (3.49) for $\lambda = \lambda_\pm$ in the K_+ valley and the corresponding equations for the CDW phase in the K_- valley. Therefore, in the K_ξ valley one has $\lambda_\pm = \lambda^n_\xi(k)$. As follows from Eq. (3.86), this implies the energy spectrum

$$E^{\xi\kappa}_{n\pm}(k) = \pm\sqrt{\beta^2 + \left(\alpha + \kappa\sqrt{\gamma^2 + \epsilon_0^2\lambda^\xi_n(k)}\right)^2}, \qquad \kappa = \pm, \quad n = 0, 1, 2, \dots . \tag{3.91}$$

Taking into account that the lowest solution $\lambda^\xi_0(k)$ changes continuously from 0 to $+\infty$, we see that the lowest energy branch is monotonic if $|\gamma| > \alpha$ or has an extremum otherwise. Thus, the spectrum gap in the Dirac model is equal to

$$E_{\text{gap}} = 2\sqrt{\beta^2 + \Theta(|\gamma| - \alpha)(|\gamma| - \alpha)^2}. \tag{3.92}$$

In the case $\mu'\tilde{\Delta} = \tilde{\mu}\Delta'$ [this includes AF and F phases; see Figs. 3.5(a), 3.5(c), 3.5(d)], the spectrum (3.91) is given by

$$E^{\xi\kappa}_{n\pm}(k) = \pm\left|\sqrt{\mu'^2 + \tilde{\mu}^2} + \kappa\sqrt{\Delta'^2 + \tilde{\Delta}^2 + \epsilon_0^2\lambda^\xi_n(k)}\right|. \tag{3.93}$$

A pair of counterpropagating gapless edge states is present at each edge if

$$\sqrt{\mu'^2 + \tilde{\mu}^2} > \sqrt{\Delta'^2 + \tilde{\Delta}^2};$$

otherwise the gap in the spectrum is equal to

$$E_{\text{gap}} = 2\left(\sqrt{\Delta'^2 + \tilde{\Delta}^2} - \sqrt{\mu'^2 + \tilde{\mu}^2}\right). \tag{3.94}$$

Note that the gapless states in the F phase with $|\mu'| < |\Delta'|$ are located between the two valleys [40] and are not captured by the Dirac model [25, 26, 62].

In the absence of valley-odd potentials [$\tilde{\mu} = \Delta' = 0$; see Fig. 3.5(b)], the spectrum (3.91) is given by

$$E^{\xi\kappa}_{n\pm}(k) = \pm\sqrt{\tilde{\Delta}^2 + \left(|\mu'| + \kappa\epsilon_0\sqrt{\lambda^\xi_n(k)}\right)^2}, \tag{3.95}$$

and the ratio of the edge gap $E_{\text{gap}} = 2|\tilde{\Delta}|$ to the bulk gap $E_{0+} - E_{0-} = 2\sqrt{\tilde{\Delta}^2 + \mu'^2}$ changes from unity in the AF phase ($\mu' = 0$) to zero in the F phase ($\tilde{\Delta} = 0$). The behavior of edge state spectrum in this case qualitatively agrees with the recent numerical self-consistent Hartree-Fock study [31], where the modification of the order parameter at the boundary was taken into account.

In the case of a finite NNN hopping parameter, the boundary condition at $y = 0$,

$$\sigma_0 \otimes [\tau_0 + \xi(\tau_3 \cos\vartheta - \tau_1 \sin\vartheta)]\Psi_{K_\xi}(-kl) = 0, \tag{3.96}$$

gives the dispersion equation

$$\begin{aligned} &g^+ u_{++}^{(-)} + \epsilon_0^2 (t'/t)^{2\xi} u_{--}^{(-)} \\ &\quad + \xi(t'/t)^{\xi}\epsilon_0 E\left\{u_{+-}^{(-)} + u_{-+}^{(-)} + \frac{4[\mu'(\Delta' + \mu') + \tilde{\mu}(\tilde{\Delta} + \tilde{\mu})](u_{+-}^{(-)} - u_{-+}^{(-)})}{\epsilon_0^2(\lambda_+ - \lambda_-)}\right\} = 0, \end{aligned} \tag{3.97}$$

where we introduced

$$u_{\alpha\beta}^{(\pm)} = U\Big(\alpha\tfrac{1}{2} - \lambda_+, \pm\sqrt{2}kl\Big)U\Big(\beta\tfrac{1}{2} - \lambda_-, \pm\sqrt{2}kl\Big). \tag{3.98}$$

For the edge $y = W$, the dispersion equation is obtained from (3.97) by replacing $k \to W/l^2 - k$ and exchanging the valleys. Similarly to the CDW phase, the edge state branch connecting the two valleys becomes dispersive at finite t' [Fig. 3.5(e)] and makes the spectrum gapless provided that $|t'|$ exceeds the LLL splitting $2E_{0+}$ with E_{0+} given in Eq. (3.87).

In the case of an armchair ribbon, the boundary condition (3.32) at $x = x_0$ can be written as

$$[1 + (\tilde{\tau}_2 \cos\theta_0 - \tilde{\tau}_1 \sin\theta_0) \otimes \sigma_0 \otimes \tau_2]\begin{pmatrix} \widetilde{\Psi}_{K_+} \\ \widetilde{\Psi}_{K_-} \end{pmatrix}_{x=x_0} = 0, \tag{3.99}$$

or, using Eq. (3.43),

$$(1 - \tilde{\tau}_2 \otimes \sigma_0 \otimes \tau_1)\begin{pmatrix} \Psi_{K_+} \\ e^{-i\theta_0}\Psi_{K_-} \end{pmatrix}_{\eta = kl + x_0/l} = 0. \tag{3.100}$$

Substituting the solution (3.84) into this equation with $x_0 = 0$ leads to the dispersion equation

$$\begin{aligned} &g^+ u_{++}^{(+)} - \epsilon_0^2 u_{--}^{(+)} \pm \Bigg\{\epsilon_0(\mu' + \Delta')(u_{+-}^{(+)} + u_{-+}^{(+)}) \\ &\quad + \frac{4[\mu'(E^2 - \tilde{\Delta}^2) + \tilde{\Delta}\tilde{\mu}(\Delta' - \mu') + \Delta'\tilde{\mu}^2]}{\epsilon_0(\lambda_+ - \lambda_-)}(u_{+-}^{(+)} - u_{-+}^{(+)})\Bigg\} = 0. \end{aligned} \tag{3.101}$$

For the edge $x = W$, the replacement $k \to -W/l^2 - k$ has to be made in the above equation.

In the absence of the valley-odd potentials ($\tilde{\mu} = \Delta' = 0$) the dispersion equation (3.101) reduces to two identical equations (3.61) for $\lambda = \lambda_\pm$. Therefore, the spectrum in this case is given by

$$E^{\kappa}_{n\pm}(k) = \pm\sqrt{\tilde{\Delta}^2 + \left(|\mu'| + \kappa\epsilon_0\sqrt{\tilde{\lambda}_n(k)}\right)^2}, \qquad \kappa = \pm. \tag{3.102}$$

The edge gap, corresponding to the minimum value of the lowest positive energy branch $E^{-}_{0+}(k)$, is equal to $2|\tilde{\Delta}|$ [23]. We find numerically that at nonzero $\tilde{\mu}$ and Δ' ($|\tilde{\mu}|, |\tilde{\Delta}| \ll \epsilon_0$), the lowest branches of the spectrum have qualitatively similar behavior. The edge gap is approximately equal to $E_{\rm gap} \simeq 2|\tilde{\Delta}+\tilde{\mu}|$ and is almost unaffected by the finite NNN hopping parameter (provided $|t'/t| \ll 1$). The ratio of the edge gap to the bulk gap

$$\frac{E_{\rm gap}}{E_{0+} - E_{0-}} \simeq \left[1 + \left(\frac{\mu' + \Delta'}{\tilde{\mu} + \tilde{\Delta}}\right)^2\right]^{-1/2} \tag{3.103}$$

changes from unity in the AF phase to zero in the F phase [Figs. 3.5(f)–3.5(h)], in agreement with the previous theoretical results [23, 31] and experiment [34].

3.4 Conclusion

In this chapter, we studied the edge state spectrum of the $\nu = 0$ quantum Hall state in monolayer graphene in the CDW, KD, AF, CAF, and F phases. The main result is establishing the criterion for the existence of gapless current-carrying excitations in each phase, which provides the concrete theoretical predictions from the mean-field model with the homogeneous symmetry-breaking terms in the cases of ideal zigzag and armchair edges.

Our analysis shows that the existence of gapless edge states depends on the edge type, and the difference between the spectra of zigzag and armchair ribbons is even more profound in the case of a finite NNN hopping term.

For a ribbon with armchair edges, the influence of the NNN hopping parameter and the ratio of symmetry-breaking terms (chemical potentials and mass gaps) on the spectrum is negligible for all phases. In the CDW and AF phases, the band gap is equal to the bulk LLL splitting, in agreement with the previous studies [20,25,26]. For the transition from the CAF to F phase, we obtain the closing of the edge gap, which is consistent with the earlier theoretical results [23,31] and the recent experiment [34]. In the KD phase, the spectrum is generically gapped but the edge gap closes at a certain valley isospin angle of the KD order parameter.

In the case of zigzag edges, the band gap is strongly affected by the finite NNN hopping parameter. At $t' = 0$, the spectrum is gapped in the KD phase and gapless in the F phase. For the CDW and AF phases, the gapless edge states exist if the chemical-potential-like symmetry breaking terms exceed the corresponding mass gaps, in agreement with Refs. [25, 26]. In the CAF phase, the band gap can vary between zero and the size of the bulk LLL splitting, depending on the ratios between four different symmetry-breaking terms. At a finite NNN hopping parameter larger than the bulk LLL splitting, the band gap is closed in all considered phases, except the KD one, due to the deformation of the edge state branch connecting the two valleys; for the KD phase, the edge gap becomes approximately equal to the half of the bulk gap. It is notable that the KD phase is the only state which can have the gapped spectrum at such a large value of NNN hopping for both edge types (as was already indicated in Sec. 3.3, the experimental value $|t'| \simeq 0.3$ eV [44] is indeed large).

As shown in Ref. [47], mixed armchair/zigzag edges with the intermediate orientation are generally described within the Dirac model by the zigzag-like boundary condition whereas the number of dispersionless edge states is determined by the percentage of zigzag edge segments or, equivalently, by the momentum separation of the $K_{\pm}$ points projected along the ribbon. This suggests that results obtained here for the zigzag case should hold in general for a mixed edge with the only difference being a reduced bandwidth of the intervalley edge state branch (given by $|t'|$ for a purely zigzag boundary). Therefore, in the cases when the spectrum is gapless due to this zigzag edge state branch, one can expect the gap opening at some critical deviation from the zigzag direction, when the edge state bandwidth becomes smaller than the bulk LLL splitting.

Our results for the case of armchair edges support the currently accepted CAF-F scenario [23, 31, 32, 34] of the observed gradual insulator-metal transition in the tilted magnetic field [34]. For the zigzag edges and finite NNN hopping, however, we find that CAF phase has gapless edge excitations. Whether these excitations indeed lead to a conducting state or they are modified substantially beyond the present model is an important question. As a first step, it would be reasonable to take into account the variation of the order parameter near the edges [20, 29–32]. This issue will be considered elsewhere.

3.5 Appendix. Tight-binding Hamiltonian for graphene ribbon

3.5.1 Zigzag ribbon: CDW and CAF phases

For a zigzag ribbon, the free part of the tight-binding Hamiltonian (including the NNN hopping terms) can be written as

$$\mathcal{H}_0 + \mathcal{H}' = -\int_{-\pi/a}^{\pi/a} \frac{dk}{2\pi} \chi^\dagger(k) \sigma_0 \otimes \left\{ t \begin{pmatrix} 0 & M_1 \\ M_1^T & 0 \end{pmatrix} + 2t' \operatorname{Re} \begin{pmatrix} M_2^+ & 0 \\ 0 & M_2^- \end{pmatrix} \right\} \chi(k), \tag{3.104}$$

where the $4N$ components of the vectors

$$\chi(k) = \begin{pmatrix} \chi_A^+(k) \\ \chi_B^+(k) \\ \chi_A^-(k) \\ \chi_B^-(k) \end{pmatrix}, \qquad \chi_X^s(k) = \begin{pmatrix} c_{Xs1}(k) \\ c_{Xs2}(k) \\ \vdots \\ c_{XsN}(k) \end{pmatrix}, \tag{3.105}$$

are the Fourier-transformed in the x direction lattice fermion operators,

$$\begin{pmatrix} a_{jxs} \\ b_{jxs} \end{pmatrix} = \sqrt{a} \int_{-\pi/a}^{\pi/a} \frac{dk}{2\pi} e^{ikx} \begin{pmatrix} c_{Asj}(k) \\ c_{Bsj}(k) \end{pmatrix}, \quad j = 1, \ldots, N. \tag{3.106}$$

The symmetry-breaking terms (3.20)–(3.21) are given by

$$\Omega_\alpha^\pm = \int_{-\pi/a}^{\pi/a} \frac{dk}{2\pi} \chi^\dagger(k) \sigma_\alpha \otimes \begin{pmatrix} \mathbb{1}_N & 0 \\ 0 & \pm\mathbb{1}_N \end{pmatrix} \chi(k), \tag{3.107}$$

$$\Lambda_\alpha^\pm = \int_{-\pi/a}^{\pi/a} \frac{dk}{2\pi} \chi^\dagger(k) \sigma_\alpha \otimes \left\{ \frac{2}{3\sqrt{3}} \operatorname{Im} \begin{pmatrix} M_2^+ & 0 \\ 0 & \pm M_2^- \end{pmatrix} \right\} \chi(k). \tag{3.108}$$

The matrix elements of M_1 and $M_2^\pm$ are expressed as

$$\begin{aligned} [M_1]_{jj'} &= \delta_{j',j+1} + 2\delta_{jj'} \cos(k_j a/2) \\ [M_2^\pm]_{jj'} &= \delta_{jj'} e^{ik_j^\pm a} + (\delta_{j',j+1} + \delta_{j',j-1}) e^{-i(k_j^\pm + k_{j'}^\pm)a/4}, \end{aligned} \tag{3.109}$$

where we introduced

$$k_j = k - \frac{\pi\phi}{a}\left(2j - \frac{1}{3}\right), \qquad k_j^{\pm} = k_j \mp \frac{\pi\phi}{3a}. \tag{3.110}$$

Here $\phi = \sqrt{3}a^2/(4\pi l^2)$ is the magnetic flux through a hexagonal unit cell in units of the magnetic flux quantum.

3.5.2 Zigzag ribbon: KD phase

The Kekulé order term (3.22) triples the number of nonequivalent atoms in the zigzag direction (Fig. 3.1), and the full mean-field Hamiltonian can be written as

$$\mathcal{H}_0 + \mathcal{H}' + \mathcal{H}_{\mathrm{KD}} = \sum_{s=\pm} \int_{-\frac{\pi}{3a}}^{\frac{\pi}{3a}} \frac{dk}{2\pi} \chi_s^{\dagger}(k) H_s(k) \chi_s(k), \tag{3.111}$$

where $\chi_s(k)$ is the $6N$-component vector

$$\chi_s(k) = \begin{pmatrix} \chi_{A_1}^s(k) \\ \chi_{A_2}^s(k) \\ \chi_{A_3}^s(k) \\ \chi_{B_1}^s(k) \\ \chi_{B_2}^s(k) \\ \chi_{B_3}^s(k) \end{pmatrix}, \qquad \chi_X^s(k) = \begin{pmatrix} c_{Xs1}(k) \\ c_{Xs2}(k) \\ \vdots \\ c_{XsN}(k) \end{pmatrix}, \tag{3.112}$$

and the blocks of the matrix

$$H_s(k) = \begin{pmatrix} Y_+ & X \\ X^{\dagger} & Y_- \end{pmatrix} + s\mu_Z \mathbb{1}_{6N}, \tag{3.113}$$

are given by

$$X = \begin{pmatrix} \beta_0 M_3 & \beta_1 M_4 & \beta_2 M_4^{\dagger} \\ \beta_1 M_4^{\dagger} & \beta_2 M_3 & \beta_0 M_4 \\ \beta_2 M_4 & \beta_0 M_4^{\dagger} & \beta_1 M_3 \end{pmatrix}, \tag{3.114}$$

$$Y_{\pm} = -t' \begin{pmatrix} 0 & (M_2^{\pm})^{\dagger} & M_2^{\pm} \\ M_2^{\pm} & 0 & (M_2^{\pm})^{\dagger} \\ (M_2^{\pm})^{\dagger} & M_2^{\pm} & 0 \end{pmatrix}. \tag{3.115}$$

The matrix elements of M_3 and M_4 are

$$\begin{aligned} [M_3]_{jj'} &= \delta_{j',j+1}, \\ [M_4]_{jj'} &= \delta_{jj'} e^{ik_j a/2}, \end{aligned} \tag{3.116}$$

and we introduced

$$\beta_j \equiv -t + \frac{2}{3}\Delta \cos\Big(\theta - \frac{2\pi j}{3}\Big) + \frac{2i}{3}\mu \sin\Big(\theta - \frac{2\pi j}{3}\Big). \tag{3.117}$$

3.5.3 Armchair ribbon

For an armchair ribbon, the free part of the Hamiltonian (including the NNN hopping terms) reads

$$\mathcal{H}_0 + \mathcal{H}' = -\int_{-\frac{\pi}{\sqrt{3}a}}^{\frac{\pi}{\sqrt{3}a}} \frac{dk}{2\pi} \chi^\dagger(k)\sigma_0 \otimes \left\{ t \begin{pmatrix} 0 & M_5 \\ M_5^\dagger & 0 \end{pmatrix} + t' \begin{pmatrix} M_6^+ & 0 \\ 0 & M_6^+ \end{pmatrix} \right\} \chi(k), \tag{3.118}$$

where $\chi(k)$ is defined in Eq. (3.105) with

$$\begin{pmatrix} a_{jys} \\ b_{jys} \end{pmatrix} = (\sqrt{3}a)^{\frac{1}{2}} \int_{-\frac{\pi}{\sqrt{3}a}}^{\frac{\pi}{\sqrt{3}a}} \frac{dk}{2\pi} e^{iky} \begin{pmatrix} c_{Asj}(k) \\ c_{Bsj}(k) \end{pmatrix}, \quad j = 1, \ldots, N. \tag{3.119}$$

The symmetry-breaking terms (3.20)–(3.21) are given by

$$\Omega_\alpha^\pm = \int_{-\frac{\pi}{\sqrt{3}a}}^{\frac{\pi}{\sqrt{3}a}} \frac{dk}{2\pi} \chi^\dagger(k)\sigma_\alpha \otimes \begin{pmatrix} \mathbb{1}_N & 0 \\ 0 & \pm\mathbb{1}_N \end{pmatrix} \chi(k), \tag{3.120}$$

$$\Lambda_\alpha^\pm = 3^{-\frac{3}{2}} i \int_{-\frac{\pi}{\sqrt{3}a}}^{\frac{\pi}{\sqrt{3}a}} \frac{dk}{2\pi} \chi^\dagger(k)\sigma_\alpha \otimes \begin{pmatrix} M_6^- & 0 \\ 0 & \pm M_6^- \end{pmatrix} \chi(k), \tag{3.121}$$

$$\mathcal{H}_{\mathrm{KD}} = \int_{-\frac{\pi}{\sqrt{3}a}}^{\frac{\pi}{\sqrt{3}a}} \frac{dk}{2\pi} \chi^\dagger(k)\sigma_0 \otimes \begin{pmatrix} 0 & M_7 \\ M_7^\dagger & 0 \end{pmatrix} \chi(k) + \mathcal{H}_{\mathrm{Z}}. \tag{3.122}$$

The matrix elements of M_5, $M_6^{\pm}$, and M_7 are

$$\begin{aligned}
[M_5]_{jj'} &= \delta_{j'j} e^{\frac{i\widetilde{k}_j a}{\sqrt{3}}} + (\delta_{j',j+1} + \delta_{j',j-1}) e^{-\frac{i(\widetilde{k}_j + \widetilde{k}_{j'})a}{4\sqrt{3}}}, \\
[M_6^{\pm}]_{jj'} &= \delta_{j',j-2} \pm \delta_{j',j+2} \\
&\quad + 2(\delta_{j',j+1} \pm \delta_{j',j-1}) \cos\Big((\widetilde{k}_j + \widetilde{k}_{j'}) a \sqrt{3}/4\Big), \\
[M_7]_{jj'} &= (\beta_{j+j'} + t)[M_5]_{jj'},
\end{aligned} \tag{3.123}$$

where $\widetilde{k}_j = k + 2\pi\phi j/(\sqrt{3}a)$.

Bibliography

[1] P. K. Pyatkovskiy and V. A. Miransky, Phys. Rev. B **90**, 195407 (2014).

[2] K. S. Novoselov, A. K. Geim, S. V. Morozov, D. Jiang, M. I. Katsnelson, I. V. Grigorieva, S. V. Dubonos, and A. A. Firsov, Nature **438**, 197 (2005).

[3] Y. Zhang, Y.-W. Tan, H. L. Stormer, and P. Kim, Nature **438**, 201 (2005).

[4] V. P. Gusynin and S. G. Sharapov, Phys. Rev. Lett. **95**, 146801 (2005).

[5] N. M. R. Peres, F. Guinea, and A. H. Castro Neto, Phys. Rev. B **73**, 125411 (2006).

[6] Y. Zhang, Z. Jiang, J. P. Small, M. S. Purewal, Y.-W. Tan, M. Fazlollahi, J. D. Chudow, J. A. Jaszczak, H. L. Stormer, and P. Kim, Phys. Rev. Lett. **96**, 136806 (2006).

[7] Z. Jiang, Y. Zhang, H. L. Stormer, and P. Kim, Phys. Rev. Lett. **99**, 106802 (2007).

[8] X. Du, I. Skachko, F. Duerr, A. Luican, and E. Y. Andrei, Nature **462**, 192 (2009).

[9] K. I. Bolotin, F. Ghahari, M. D. Shulman, H. L. Stormer, and P. Kim, Nature **462**, 196 (2009).

[10] J. G. Checkelsky, L. Li, and N. P. Ong, Phys. Rev. Lett. **100**, 206801 (2008).

[11] J. G. Checkelsky, L. Li, and N. P. Ong, Phys. Rev. B **79**, 115434 (2009).

[12] J. Alicea and M. P. A. Fisher, Phys. Rev. B **74**, 075422 (2006).

[13] V. P. Gusynin, V. A. Miransky, S. G. Sharapov, and I. A. Shovkovy, Phys. Rev. B **74**, 195429 (2006).

[14] L. Sheng, D. N. Sheng, F. D. M. Haldane, and L. Balents, Phys. Rev. Lett. **99**, 196802 (2007).

[15] I. F. Herbut, Phys. Rev. B **75**, 165411 (2007).

[16] K. Nomura, S. Ryu, and D.-H. Lee, Phys. Rev. Lett. **103**, 216801 (2009).

[17] C.-Y. Hou, C. Chamon, and C. Mudry, Phys. Rev. B **81**, 075427 (2010).

[18] D. A. Abanin, P. A. Lee, and L. S. Levitov, Phys. Rev. Lett. **96**, 176803 (2006).

[19] D. A. Abanin, K. S. Novoselov, U. Zeitler, P. A. Lee, A. K. Geim, and L. S. Levitov, Phys. Rev. Lett. **98**, 196806 (2007).

[20] J. Jung and A. H. MacDonald, Phys. Rev. B **80**, 235417 (2009).

[21] I. F. Herbut, Phys. Rev. B **76**, 085432 (2007).

[22] M. Kharitonov, Phys. Rev. B **85**, 155439 (2012).

[23] M. Kharitonov, Phys. Rev. B **86**, 075450 (2012).

[24] B. Roy, M. P. Kennett, and S. Das Sarma, Phys. Rev. B **90**, 201409 (2014).

[25] V. P. Gusynin, V. A. Miransky, S. G. Sharapov, and I. A. Shovkovy, Phys. Rev. B **77**, 205409 (2008).

[26] V. P. Gusynin, V. A. Miransky, S. G. Sharapov, I. A. Shovkovy, and C. M. Wyenberg, Phys. Rev. B **79**, 115431 (2009).

[27] M. O. Goerbig, C. R. Phys. **12**, 369 (2011).

[28] Z. Yang and J. H. Han, Phys. Rev. B **81**, 115405 (2010).

[29] H. A. Fertig and L. Brey, Phys. Rev. Lett. **97**, 116805 (2006).

[30] E. Shimshoni, H. A. Fertig, and G. V. Pai, Phys. Rev. Lett. **102**, 206408 (2009).

[31] J. L. Lado and J. Fernández-Rossier, Phys. Rev. B **90**, 165429 (2014).

[32] G. Murthy, E. Shimshoni, and H. A. Fertig, Phys. Rev. B **90**, 241410 (2014).

[33] Y. Zhao, P. Cadden-Zimansky, F. Ghahari, and P. Kim, Phys. Rev. Lett. **108**, 106804 (2012).

[34] A. F. Young, J. D. Sanchez-Yamagishi, B. Hunt, S. H. Choi, K. Watanabe, T. Taniguchi, R. C. Ashoori, and P. Jarillo-Herrero, Nature **505**, 528 (2014).

[35] M. Arikawa, H. Aoki, and Y. Hatsugai, AIP Conf. Proc. **1399**, 823 (2011).

[36] M. O. Goerbig, Rev. Mod. Phys. **83**, 1193 (2011).

[37] E. V. Gorbar, V. P. Gusynin, V. A. Miransky, and I. A. Shovkovy, Phys. Rev. B **78**, 085437 (2008).

[38] E. V. Gorbar, V. P. Gusynin, V. A. Miransky, and I. A. Shovkovy, Phys. Rev. B **85**, 235460 (2012).

[39] M. Kharitonov, Phys. Rev. B **86**, 195435 (2012).

[40] C. L. Kane and E. J. Mele, Phys. Rev. Lett. **95**, 226801 (2005).

[41] F. D. M. Haldane, Phys. Rev. Lett. **61**, 2015 (1988).

[42] H. Watanabe, Y. Hatsugai, and H. Aoki, Phys. Rev. B **82**, 241403 (2010).

[43] K. Sasaki, S. Murakami, and R. Saito, Appl. Phys. Lett. **88**, 113110 (2006).

[44] A. Kretinin, G. L. Yu, R. Jalil, Y. Cao, F. Withers, A. Mishchenko, M. I. Katsnelson, K. S. Novoselov, A. K. Geim, and F. Guinea, Phys. Rev. B **88**, 165427 (2013).

[45] L. Brey and H. A. Fertig, Phys. Rev. B **73**, 235411 (2006).

[46] E. McCann and V. I. Fal'ko, J. Phys.: Condens. Matter **16**, 2371 (2004).

[47] A. R. Akhmerov and C. W. J. Beenakker, Phys. Rev. B **77**, 085423 (2008).

[48] J. Wurm, K. Richter, and I. Adagideli, Phys. Rev. B **84**, 075468 (2011).

[49] J. A. M. van Ostaay, A. R. Akhmerov, C. W. J. Beenakker, and M. Wimmer, Phys. Rev. B **84**, 195434 (2011).

[50] M. Abramowitz and I. A. Stegun, *Handbook of Mathematical Functions with Formulas, Graphs, and Mathematical Tables* (U.S. Goverment Printing Office, Washington, DC, 1972).

[51] M. Fujita, K. Wakabayashi, K. Nakada, and K. Kusakabe, J. Phys. Soc. Jpn. **65**, 1920 (1996).

[52] K. Nakada, M. Fujita, G. Dresselhaus, and M. S. Dresselhaus, Phys. Rev. B **54**, 17954 (1996).

[53] F. W. J. Olver, J. Res. Natl. Bur. Stand. B **63**, 131 (1959).

[54] P. K. Pyatkovskiy, Phys. Rev. B **88**, 205417 (2013).

[55] G. Tkachov and M. Hentschel, Phys. Rev. B **86**, 205414 (2012).

[56] P.-Y. Chang, C. Mudry, and S. Ryu, J. Stat. Mech. **2014**, P09014 (2014).

[57] J. Tworzydło, B. Trauzettel, M. Titov, A. Rycerz, and C. W. J. Beenakker, Phys. Rev. Lett. **96**, 246802 (2006).

[58] J. A. Fürst, J. G. Pedersen, C. Flindt, N. A. Mortensen, M. Brandbyge, T. G. Pedersen, and A.-P. Jauho, New J. Phys. **11**, 095020 (2009).

[59] T. Stauber and J. Schliemann, New J. Phys. **11**, 115003 (2009).

[60] M. V. Berry and R. J. Mondragon, Proc. R. Soc. London A **412**, 53 (1987).

[61] J. Tworzydło, I. Snyman, A. R. Akhmerov, and C. W. J. Beenakker, Phys. Rev. B **76**, 035411 (2007).

[62] A. De Martino, A. Hütten, and R. Egger, Phys. Rev. B **84**, 155420 (2011).

Chapter 4

Broken-symmetry quantum Hall states in bilayer graphene

4.1 Introduction

The interaction-induced phenomena in bilayer graphene have attracted a significant attention due to the peculiar band structure and the rich symmetry in this system [1]. Within the non-interacting model of bilayer graphene, the lowest Landau level (LLL) is eightfold degenerate due to the spin and valleys degrees of freedom and the additional orbital $n = 0, 1$ level degeneracy, which results in the step of the quantized Hall conductivity $\sigma_{xy} = \nu e^2/h$ between the filling factors $\nu = \pm 4$ [2]. The additional quantum Hall plateaux $\nu = 0, \pm 1, \pm 2, \pm 3$ observed in the higher quality samples at strong magnetic fields [3–12] indicate that this degeneracy is completely lifted due to the interactions. Because of the SU(4) spin-valley symmetry and the orbital LLL degeneracy, there is a number of possible states (phases) that can correspond to a given plateau. Changing the applied perpendicular electric field and tilting the magnetic field with respect to the graphene plane allows to induce various phase transitions [13]. Among the proposed candidates for the $\nu = 0$ state are the ferromagnetic (F) and the layer polarized (LP) [14–19], the Kekulé distortion (KD) and the partially layer polarized (PLP) [20], and the canted antiferromagnetic (CAF) [20–22] phases. Different ground states have also been suggested for other filling factors [12, 15, 23].

In Refs. [14, 15], the possible phases have been examined by solving the gap equation in the LLL approximation with the screened Coulomb interaction and the order parameter assumed to be diagonal in both spin and the valley isospin. The obtained behavior of the LLL gap and the phase transitions qualitatively agree with the results of the experiments. In Ref. [20], on the other hand, the most general form of the order parameter matrix has been used and the energy functional has been minimized for the case of the local interaction terms. One of the resulting ground states, the CAF phase appears to be realized in experiments with perpendicular magnetic field and zero bias [13].

In this chapter we extend the analysis of Refs. [14, 15] to the case of nondiagonal order parameters and take into account all possible short-interaction terms that lead to the different broken-symmetry phases. We find the solutions of the gap equation for the even filling factors.

The chapter is organized as follows. In Sec. 4.2 we describe the low-energy continuum two-band model with different interaction terms. In Sec. 4.3 we derive the gap equation and the free energy functional in the general case. The solutions of the gap equation are obtained in Sec. 4.4 for the filling factor $\nu = 0$ and in Sec. 4.5 for $\nu = \pm 2$. The discussion of the main results is given in Sec. 4.6.

4.2 Model

We use the two-band low-energy model with the eight-component spinors defined as $\Psi = (\Psi^{+}_{K_+}, \Psi^{-}_{K_+}, \Psi^{+}_{K_-}, \Psi^{-}_{K_-})^{\mathsf{T}}$, where

$$\Psi^{s}_{K_+} = \begin{pmatrix} \Psi^{s}_{K_+A_1} \\ \Psi^{s}_{K_+B_2} \end{pmatrix}, \qquad \Psi^{s}_{K_-} = \begin{pmatrix} \Psi^{s}_{K_-B_2} \\ \Psi^{s}_{K_-A_1} \end{pmatrix}, \tag{4.1}$$

and the full Hamiltonian $H = H_0 + H_{\text{int}}$. The free part,

$$H_0 = \int d^2\mathbf{r}\, \Psi^{\dagger}(\mathbf{r}) \left(\mathcal{H}_{\text{sym}} + \mathcal{H}_{\text{ext}}\right) \Psi(\mathbf{r}), \tag{4.2}$$

includes the kinetic term

$$\mathcal{H}_{\text{sym}} = -\frac{1}{2m} \tilde{\tau}_0 \otimes \sigma_0 \otimes \begin{pmatrix} 0 & (\hat{\pi}_x - i\hat{\pi}_y)^2 \\ (\hat{\pi}_x + i\hat{\pi}_y)^2 & 0 \end{pmatrix}, \qquad \hat{\boldsymbol{\pi}} = -i\hbar\nabla + \frac{e}{c}\mathbf{A}, \tag{4.3}$$

invariant under the U(4) symmetry with generators $\sigma_\alpha \otimes \tilde{\tau}_\beta \otimes \tau_0$, $\alpha, \beta = 0, 1, 2, 3$, and the symmetry-breaking external potential terms

$$\mathcal{H}_{\text{ext}} = Z\, \sigma_3 \otimes \tilde{\tau}_0 \otimes \tau_0 + \tilde{\Delta}_0\, \sigma_0 \otimes \tilde{\tau}_3 \otimes \tau_3, \tag{4.4}$$

where $Z = \mu_B B$ is the Zeeman coupling (μ_B is the Bohr magneton) and $2\tilde{\Delta}_0 = eE_\perp d$ is a top-bottom gates voltage imbalance due to the electric field orthogonal to the bilayer planes ($d \simeq 0.35$ nm is the interlayer distance). The Pauli matrices σ_i, $\tilde{\tau}_i$, and τ_i, $i = 1, 2, 3$ (σ_0, $\tilde{\tau}_0$, and τ_0 are the unit matrices), act on the spin ($s = \pm$), valley ($K_\pm$), and layer-sublattice (A_1 and B_2) components (the basis spin states correspond to the direction of the external magnetic field that can be tilted with respect to the graphene plane). The interaction part consists of the long-range Coulomb term and the lattice-scale interactions,

$$H_{\text{int}} = H_{\text{Coul}} + H_{\text{lat}}. \tag{4.5}$$

The long-range Coulomb interaction term

$$\begin{aligned} H_{\text{Coul}} &= \frac{e^2}{2\kappa}\int d^3\mathbf{x}\, d^3\mathbf{x}'\, \frac{n(\mathbf{x})n(\mathbf{x}')}{|\mathbf{x}-\mathbf{x}'|} && (4.6)\\ &= \frac{1}{2}\int d^2\mathbf{r}\, d^3\mathbf{r}' \begin{pmatrix} \rho_1(\mathbf{r}) \\ \rho_2(\mathbf{r}) \end{pmatrix}^{\mathsf{T}} \begin{pmatrix} V(\mathbf{r}-\mathbf{r}') & V_{12}(\mathbf{r}-\mathbf{r}') \\ V_{12}(\mathbf{r}-\mathbf{r}') & V(\mathbf{r}-\mathbf{r}') \end{pmatrix} \begin{pmatrix} \rho_1(\mathbf{r}') \\ \rho_2(\mathbf{r}') \end{pmatrix} && (4.7)\\ &= \frac{1}{2}\int d^2\mathbf{r}\, d^2\mathbf{r}' \left[\rho(\mathbf{r})V(\mathbf{r}-\mathbf{r}')\rho(\mathbf{r}') + 2\rho_1(\mathbf{r})V_{\text{IL}}(\mathbf{r}-\mathbf{r}')\rho_2(\mathbf{r}')\right], && (4.8) \end{aligned}$$

where $\mathbf{x} \equiv (\mathbf{r}, z)$, $\mathbf{r} \equiv (x, y)$, contains the layer-symmetric part

$$V(\mathbf{r}) = \frac{e^2}{\kappa|\mathbf{r}|} \tag{4.9}$$

and the asymmetric interlayer part

$$V_{\text{IL}}(\mathbf{r}) = V_{12}(\mathbf{r}) - V(\mathbf{r}), \qquad V_{12}(\mathbf{r}) = \frac{e^2}{\kappa\sqrt{\mathbf{r}^2 + d^2}}. \tag{4.10}$$

Here κ is the dielectric constant,

$$n(\mathbf{x}) = \delta\left(z - \frac{d}{2}\right)\rho_1(\mathbf{r}) + \delta\left(z + \frac{d}{2}\right)\rho_2(\mathbf{r}) \tag{4.11}$$

is the three-dimensional charge density,

$$\rho_1(\mathbf{r}) = \sum_{s,\xi=\pm} [\Psi^s_{K_\xi A_1}(\mathbf{r})]^\dagger \Psi^s_{K_\xi A_1}(\mathbf{r}) = \Psi^\dagger(\mathbf{r})P_1\Psi(\mathbf{r}), \tag{4.12}$$

$$\rho_2(\mathbf{r}) = \sum_{s,\xi=\pm} [\Psi^s_{K_\xi B_2}(\mathbf{r})]^\dagger \Psi^s_{K_\xi B_2}(\mathbf{r}) = \Psi^\dagger(\mathbf{r})P_2\Psi(\mathbf{r}) \tag{4.13}$$

are the two-dimensional charge densities in the layers 1 and 2, $\rho(\mathbf{r}) \equiv \rho_1(\mathbf{r}) + \rho_2(\mathbf{r})$ is the total two-dimensional charge density, and

$$P_1 = \frac{1 + \tilde{\tau}_3 \otimes \sigma_0 \otimes \tau_3}{2}, \qquad P_2 = \frac{1 - \tilde{\tau}_3 \otimes \sigma_0 \otimes \tau_3}{2} \tag{4.14}$$

are projectors on states in the corresponding layer. The short-range symmetry-breaking interaction term, which consists of the lattice-scale part of the Coulomb interactions and the electron-phonon interactions, has the following general form:

$$H_{\text{lat}} = \frac{1}{2}\int d^2\mathbf{r} \sum_{\alpha,\beta=0}^{3} g_{\alpha\beta}[\Psi^\dagger(\mathbf{r})\mathcal{T}_{\alpha\beta}\Psi(\mathbf{r})]^2. \tag{4.15}$$

Here the 8×8 matrices $\mathcal{T}_{\alpha\beta}$ are defined as

$$\mathcal{T}_{\alpha\beta} = \tilde{\tau}_\alpha \otimes \sigma_0 \otimes \tau_\beta, \qquad \alpha, \beta = 0, 1, 2, 3, \tag{4.16}$$

and there are eight independent coupling constants $g_{\perp\perp} \equiv g_{11} = g_{12} = g_{21} = g_{22}$, $g_{\perp z} \equiv g_{10} = g_{20}$, $g_{z\perp} \equiv g_{01} = g_{02}$, $g_{\perp 0} \equiv g_{13} = g_{23}$, $g_{0\perp} \equiv g_{31} = g_{32}$, $g_{zz} \equiv g_{33}$, $g_{z0} \equiv g_{30}$, $g_{0z} \equiv g_{03}$ (the constant g_{00} is included in the symmetric part of the Coulomb potential).

4.3 Gap equation

The effective action in the two-loop approximation is a functional for the full Green's function G and has the form

$$\begin{aligned}
\Gamma(G) = &-i\,\mathrm{Tr}[\mathrm{Ln}\,G^{-1} + S^{-1}G - 1] - \frac{1}{2}\int d^3u\, d^3u' \Big\{ \mathrm{tr}[G(u,u')G(u',u)]V^{\text{eff}}(u-u') \\
&+ 2\,\mathrm{tr}[P_1 G(u,u')P_2 G(u',u)]V_{\text{IL}}^{\text{eff}}(u-u') + \sum_{\alpha,\beta=0}^{3} g_{\alpha\beta}\,\mathrm{tr}[\mathcal{T}_{\alpha\beta}G(u,u')\mathcal{T}_{\alpha\beta}G(u',u)]\delta^3(u-u') \Big\} \\
&+ \frac{1}{2}\int d^3u\, d^3u' \Big\{ \mathrm{tr}[G(u,u)]\,\mathrm{tr}[G(u',u')]V(u-u') + 2\,\mathrm{tr}[P_1G(u,u)]\,\mathrm{tr}[P_2G(u',u')]V_{\text{IL}}(u-u') \\
&+ \sum_{\alpha,\beta=0}^{3} g_{\alpha\beta}\,\mathrm{tr}[\mathcal{T}_{\alpha\beta}G(u,u)]\,\mathrm{tr}[\mathcal{T}_{\alpha\beta}G(u',u')]\delta^3(u-u') \Big\},
\end{aligned} \tag{4.17}$$

where $u \equiv (t, \mathbf{r})$ and S is the free Green's function corresponding to the Hamiltonian H_0. The trace Tr, the logarithm, and the product $S^{-1}G$ are taken in the functional sense, and the trace tr runs over the spinor indices. In the Fock term [the first integral in the right-hand side of

Eq. (4.17)], we take into account the screening of the long-range Coulomb potential leading to the effective potentials $V^{\text{eff}}(u)$ and $V^{\text{eff}}_{\text{IL}}(u)$, whereas in the Hartree term (the second integral), the bare potentials $V(u)$, $V_{\text{IL}}(u)$ are used. The screened potentials are given by [14]

$$V^{\text{eff}}(u) = e^2 \int\limits_{-\infty}^{\infty} \frac{d\omega}{2\pi} \int \frac{d^2k}{2\pi} \frac{e^{i\mathbf{kr}-i\omega t}}{\kappa k + 4\pi e^2 \Pi(\omega, \mathbf{k})}, \tag{4.18}$$

$$V^{\text{eff}}_{\text{IL}}(u) = -e^2 \int\limits_{-\infty}^{\infty} \frac{d\omega}{2\pi} \int \frac{d^2k}{2\pi} \frac{(1-e^{-kd})e^{i\mathbf{kr}-i\omega t}}{\kappa k + 2\pi e^2[\Pi_{11}(\omega, \mathbf{k}) - \Pi_{12}(\omega, \mathbf{k})](1-e^{-kd})}, \tag{4.19}$$

where $\Pi(\omega, \mathbf{k}) = \Pi_{11}(\omega, \mathbf{k}) + \Pi_{12}(\omega, \mathbf{k})$ and polarization functions $\Pi_{ij}(\omega, \mathbf{k})$ describe the electron density correlations on the layers i and j:

$$\delta(\omega + \omega')\delta(\mathbf{k} + \mathbf{k}')\Pi_{ij}(\omega, \mathbf{k}) = -i\langle 0|\rho_i(\omega, \mathbf{k})\rho_j(\omega', \mathbf{k}')|0\rangle. \tag{4.20}$$

The stationary condition $\delta\Gamma(G)/\delta G = 0$ leads to the gap equation

$$\begin{aligned} G(u_1, u_2) = {} & S(u_1, u_2) + i \int d^3u_1'\, d^3u_2'\, S(u_1, u_1') \Big\{ G(u_1', u_2') V^{\text{eff}}(u_1' - u_2') \\ & + [P_1 G(u_1', u_2') P_2 + P_2 G(u_1', u_2') P_1] V^{\text{eff}}_{\text{IL}}(u_1' - u_2') \Big\} G(u_2', u_2) \\ & - i \int d^3u_2'\, S(u_1, u_2') \Big\{ \text{tr}[G(u_2', u_2')] \tilde{V}(0) + \big(P_1\, \text{tr}[P_2 G(u_2', u_2')] + P_2\, \text{tr}[P_1 G(u_2', u_2')] \big) \tilde{V}_{IL}(0) \\ & - \sum_{\alpha,\beta=0}^{3} g_{\alpha\beta} \mathcal{T}_{\alpha\beta} \big(G(u_2', u_2') \mathcal{T}_{\alpha\beta} - \text{tr}[\mathcal{T}_{\alpha\beta} G(u_2', u_2')] \big) \Big\} G(u_2', u_2), \end{aligned} \tag{4.21}$$

where $\tilde{V}(0)$ and $\tilde{V}_{\text{IL}}(0)$ are the Fourier transforms of $V(u)$ and $V_{\text{IL}}(u)$ taken at $\omega = \mathbf{k} = 0$. Separating the Schwinger phase factors $e^{i\Phi(\mathbf{r}_1, \mathbf{r}_2)}$ in the gauge $(A_x, A_y) = (0, B_\perp x)$,

$$\Phi(\mathbf{r}_1, \mathbf{r}_2) = -\frac{(x_1 + x_2)(y_1 - y_2)}{2l^2} = e \int\limits_{\mathbf{r}_1}^{\mathbf{r}_2} d\mathbf{r} \cdot \mathbf{A}(\mathbf{r}), \tag{4.22}$$

from the translationally invariant parts of the Green's functions,

$$S(u_1, u_2) = e^{i\Phi(\mathbf{r}_1, \mathbf{r}_2)} \tilde{S}(u_1 - u_2), \qquad G(u_1, u_2) = e^{i\Phi(\mathbf{r}_1, \mathbf{r}_2)} \tilde{G}(u_1 - u_2), \tag{4.23}$$

and making the Fourier transform with respect to t, we arrive at

$$\begin{aligned}
\tilde{G}(\Omega, \mathbf{r}) &= \tilde{S}(\Omega, \mathbf{r}) + i \int\limits_{-\infty}^{\infty} \frac{d\omega}{2\pi} \int d^2\mathbf{r}_1'\, d^2\mathbf{r}_2'\, e^{i[(x-x_2')y_1'-(y-y_2')x_1']/2l^2} \\
&\times \tilde{S}(\Omega, \mathbf{r}-\mathbf{r}_1') \Big\{ \tilde{G}(\omega, \mathbf{r}_1'-\mathbf{r}_2') V^{\text{eff}}(\Omega-\omega, \mathbf{r}_1'-\mathbf{r}_2') \\
&+ [P_1 \tilde{G}(\omega, \mathbf{r}_1'-\mathbf{r}_2') P_2 + P_2 \tilde{G}(\omega, \mathbf{r}_1'-\mathbf{r}_2') P_1] V_{IL}(\Omega-\omega, \mathbf{r}_1'-\mathbf{r}_2') \Big\} \tilde{G}(\Omega, \mathbf{r}_2') \\
&- i \int d^2\mathbf{r}_2'\, e^{i(xy_2'-yx_2')/2l^2} \tilde{S}(\Omega, \mathbf{r}-\mathbf{r}_2') \Big\{ \mathrm{tr}[\tilde{G}(0)] \tilde{V}_{eff}(0) + \Big(P_1\, \mathrm{tr}[P_2 \tilde{G}(0)] + P_2\, \mathrm{tr}[P_1 \tilde{G}(0)]\Big) \tilde{V}_{IL}(0) \\
&- \sum_{\alpha,\beta=0}^{3} g_{\alpha\beta} \mathcal{T}_{\alpha\beta} \Big(\tilde{G}(0) \mathcal{T}_{\alpha\beta} - \mathrm{tr}[\mathcal{T}_{\alpha\beta} \tilde{G}(0)] \Big) \Big\} \tilde{G}(\Omega, \mathbf{r}_2'). \qquad (4.24)
\end{aligned}$$

To solve this gap (Schwinger-Dyson) equation, we need to use a specific form (ansatz) for the full propagator. The translational invariant part of the free propagator in the LLL approximation reads

$$\tilde{S}(\omega, \mathbf{r}) = \frac{e^{-\rho/2}}{2\pi l^2} [L_0(\rho) + L_1(\rho)]\, S(\omega) \otimes P_-, \qquad (4.25)$$

where

$$S(\omega) \equiv \frac{1}{\omega + \mu_0 + i\delta\, \mathrm{sgn}\,\omega + \tilde{\Delta}_0\, \sigma_0 \otimes \tilde{\tau}_3 - Z\, \sigma_3 \otimes \tilde{\tau}_0}, \qquad \rho \equiv \frac{\mathbf{r}^2}{2l^2}, \qquad P_\pm \equiv \frac{1 \pm \tau_3}{2}, \quad (4.26)$$

and μ_0 is the (bare) chemical potential. For the full propagator, we also keep only the LLL terms and use the ansatz

$$\tilde{G}(\omega, \mathbf{r}) = \frac{e^{-\rho/2}}{2\pi l^2} [G_0(\omega) L_0(\rho) + G_1(\omega) L_1(\rho)] \otimes P_-, \qquad (4.27)$$

where

$$G_n(\omega) = \frac{1}{\omega - \mathcal{M}_n + i\delta\, \mathrm{sgn}\,\omega}, \qquad n = 0, 1, \qquad (4.28)$$

and $\mathcal{M}_0$, $\mathcal{M}_1$ are 4×4 Hermitian matrices. Substituting expressions (4.25), (4.28) into gap equation (4.24) and using the static approximation $\Pi_{ij}(\omega, \mathbf{k}) = \Pi_{ij}(0, \mathbf{k})$ for the polarization functions in Eqs. (4.18)–(4.19), one arrives at the following equations for the matrices $\mathcal{M}_n$:

$$\begin{aligned}
\mathcal{M}_n = -\mu_0 T_{00} - \tilde{\Delta}_0 T_{03} + Z T_{30} + \frac{1}{4} \sum_{n'=0,1} \Big\{ & v_{n+n'} Q_{n'} + u^z_{n+n'} T_{03} Q_{n'} T_{03} \\
& - \tilde{u}_z T_{03}\, \mathrm{tr}(Q_{n'} T_{03}) + u_\perp \sum_{\alpha=1,2} T_{0\alpha} [Q_{n'} T_{0\alpha} - \mathrm{tr}(Q_{n'} T_{0\alpha})] \Big\}, \qquad (4.29)
\end{aligned}$$

where $T_{\alpha\beta} \equiv \sigma_\alpha \otimes \tilde{\tau}_\beta$, $\alpha, \beta = 0, 1, 2, 3$, and

$$Q_n = \frac{i}{\pi} \int_{-\infty}^{\infty} \frac{d\omega}{\omega - \mathcal{M}_n + i\delta \operatorname{sgn} \omega}. \tag{4.30}$$

Due to the overall neutrality of the system, we drop the Hartree term, proportional to $\operatorname{tr}(Q_n)$ [15]. Parameters

$$v_n \equiv \frac{1}{ml^2}[2I_{n+1}(x) - I^{\mathrm{IL}}_{n+1}(x)] + u_0, \qquad n = 0, 1, 2, \tag{4.31}$$

$$u^z_n \equiv u_z + \frac{1}{ml^2} I^{\mathrm{IL}}_{n+1}(x), \qquad n = 0, 1, 2, \tag{4.32}$$

$$\tilde{u}_z \equiv u_z + \frac{e^2 d}{\kappa l^2}, \tag{4.33}$$

depend on the coupling constants

$$u_j \equiv \frac{g_{j0} + g_{jz}}{\pi l^2}, \qquad j = 0, z, \perp, \tag{4.34}$$

and the screened Coulomb interaction terms

$$I_n(x) = \int_0^\infty dy \, \frac{e^{-y} f_n(y)}{\kappa \sqrt{xy} + 4\pi \tilde{\Pi}_+(y)}, \tag{4.35}$$

$$I^{\mathrm{IL}}_n(x) = \int_0^\infty dy \, \frac{e^{-y} f_n(y)(1 - e^{-\sqrt{2y}d/l})}{\kappa \sqrt{xy} + 2\pi \tilde{\Pi}_-(y)(1 - e^{-\sqrt{2y}d/l})}, \tag{4.36}$$

where $f_i(y) = [1, y, (1 - y)^2]$ for $i = 1, 2, 3$, respectively, and

$$\tilde{\Pi}_\pm(y) \equiv \frac{\hbar^2}{m}[\Pi_{11}(0, k) \pm \Pi_{12}(0, k)], \qquad y \equiv k^2 l^2/2, \tag{4.37}$$

are the dimensionless static polarization functions, given by [14]

$$\begin{aligned} \tilde{\Pi}_\pm(y) = \frac{1}{2\pi} e^{-y} \Bigg\{ & \sum_{n,m=2}^{n_{\max}} (-1)^{n+m} \frac{M_n M_m [I_{n-2,m-2}(y) + I_{nm}(y)] \mp 2 I^{(2)}_{n-2,m-2}(y)}{M_n M_m (M_n + M_m)} \\ & + 2 \sum_{n=2}^{n_{\max}} (-1)^n \frac{I_{0n}(y) - I_{1n}(y)}{M_n} \Bigg\}. \end{aligned} \tag{4.38}$$

In the above expression, $M_n = \sqrt{n(n-1)}$, $n_{\max}$ is a summation cutoff [$\tilde{\Pi}_+$(y) is convergent while $\tilde{\Pi}_-(y)$ diverges logarithmically], which can be estimated as $n_{\rm max} \approx 45/B[\mathrm{T}]$ from the applicability of the low-energy effective model [14], and

$$I_{nm}(y) = L_m^{n-m}(y)L_n^{m-n}(y), \qquad I_{nm}^{(2)}(y) = (m+1)(m+2)L_{m+2}^{n-m}(y)L_n^{m-n}(y), \tag{4.39}$$

where $L_n^m(y)$ are generalized Laguerre polynomials.

Matrices $\mathcal{M}_0$, $\mathcal{M}_1$ can be written, in general, as

$$\mathcal{M}_n = U_n^\dagger \mathcal{E}_n U_n, \qquad \mathcal{E}_n = \begin{pmatrix} E_n^a & 0 & 0 & 0 \\ 0 & E_n^b & 0 & 0 \\ 0 & 0 & E_n^c & 0 \\ 0 & 0 & 0 & E_n^d \end{pmatrix}, \qquad n = 0, 1, \tag{4.40}$$

where U_n are unitary matrices, and the elements $E_n^a \leq E_n^b \leq E_n^c \leq E_n^d$ of diagonal matrices $\mathcal{E}_n$ are shifted due to the interactions energies of the LLL sublevels. Matrices Q_n are diagonalized by the same unitary transformations,

$$Q_n = \frac{i}{\pi} U_n^\dagger \left(\int\limits_{-\infty}^{\infty} \frac{d\omega}{\omega - \mathcal{E}_n + i\delta\,\mathrm{sgn}\,\omega} \right) U_n = U_n^\dagger \mathcal{S}_n U_n, \tag{4.41}$$

where

$$\mathcal{S}_n = \begin{pmatrix} \mathrm{sgn}\, E_n^a & 0 & 0 & 0 \\ 0 & \mathrm{sgn}\, E_n^b & 0 & 0 \\ 0 & 0 & \mathrm{sgn}\, E_n^c & 0 \\ 0 & 0 & 0 & \mathrm{sgn}\, E_n^d \end{pmatrix}, \qquad n = 0, 1, \tag{4.42}$$

are the diagonal matrices with elements +1 for the empty sublevels and −1 for the filled sublevels. The filling factor is thus equal to

$$\nu = -\frac{1}{2} \sum_{n=0,1} \mathrm{tr}(\mathcal{S}_n). \tag{4.43}$$

Once Q_n are known, the gap equation (4.29) immediately gives the solutions for $\mathcal{M}_n$. In Refs. [14, 15], matrices $\mathcal{M}_n$ were assumed to be diagonal, in which case all possible matrices Q_n are also diagonal and obtained from $\mathcal{S}_n$ by the finite number of permutations of the diagonal elements. In the case of an arbitrary Hermitian matrix $\mathcal{M}_n$, there is a manifold of matrices Q_n for a given $\mathcal{S}_n$, and Eq. (4.29) becomes difficult to solve because of the complicated dependence (4.30) of Q_n on the matrices $\mathcal{M}_n$. It turns out that Q_n are easier to find by a different approach: minimizing the the free energy density

$$\mathcal{F} = -\frac{\Gamma}{TV} + \frac{\mu_0 \nu}{2\pi l^2} \tag{4.44}$$

with respect to Q_n after substituting our ansatz for the Green's functions into the expression (4.17) for the effective action. The advantage is that resulting expression for $\mathcal{F}$,

$$\begin{aligned}\mathcal{F} = -\frac{1}{4\pi l^2} \sum_{n=0,1} \Bigg\{ &-\tilde{\Delta}_0 \operatorname{tr}(T_{03} Q_n) + Z \operatorname{tr}(T_{30} Q_n) \\ &+ \frac{1}{8} \sum_{n'=0,1} \Bigg[v_{n+n'} \operatorname{tr}(Q_n Q_{n'}) + u^z_{n+n'} \operatorname{tr}(T_{03} Q_n T_{03} Q_{n'}) - \tilde{u}_z \operatorname{tr}(T_{03} Q_n) \operatorname{tr}(T_{03} Q_{n'}) \\ &+ \sum_{\alpha=1,2} u_\perp [\operatorname{tr}(T_{0\alpha} Q_n T_{0\alpha} Q_{n'}) - \operatorname{tr}(T_{0\alpha} Q_n) \operatorname{tr}(T_{0\alpha} Q_{n'})] \Bigg] \Bigg\},\end{aligned} \tag{4.45}$$

does not depend on $\mathcal{M}_n$. Here we also dropped the Hartree term, proportional to

$$\left(\sum_{n=0,1} \operatorname{tr}(Q_n) \right)^2. \tag{4.46}$$

In the absence of symmetry-breaking terms, the free energy (4.45) reads

$$\mathcal{F} = -\frac{1}{8\pi l^2} \left[v_0 + v_2 + \frac{v_1}{2} \operatorname{tr}(Q_0 Q_1) \right]. \tag{4.47}$$

Let us consider only even filling factors $\nu = 0, \pm 2$. Then the above expression is minimized when $Q_0 = Q_1 \equiv Q$, i.e., when the two orbital states $n = 0$ and $n = 1$ are filled simultaneously for a given spin and valley isospin, in agreement with Refs. [24, 25]. We assume that this is still valid in the presence of symmetry-breaking terms (much smaller than the Coulomb interaction). Then the free energy (4.45) simplifies to

$$\mathcal{F} = -\frac{v_0 + v_2 + 2v_1}{8\pi l^2} - \frac{2}{\pi l^2} \left[-\tilde{\Delta}_0 X_{03} + Z X_{30} + u^z Y_{03} - \tilde{u}_z X_{03}^2 + u_\perp (Y_{01} + Y_{02} - X_{01}^2 - X_{02}^2) \right], \tag{4.48}$$

where $u^z \equiv (u^z_0 + 2u^z_1 + u^z_2)/4$ and

$$X_{\alpha\beta} \equiv \frac{1}{4} \operatorname{tr}(T_{\alpha\beta} Q), \qquad Y_{\alpha\beta} \equiv \frac{1}{16} \operatorname{tr}[(T_{\alpha\beta} Q)^2]. \tag{4.49}$$

4.4 Filling factor $\nu = 0$

In the case $\nu = 0$, Q has two doubly degenerate eigenvalues 1 and -1. The set of all possible matrices with these eigenvalues provides a matrix representation of a Grassmannian

$$\mathrm{Gr}(2,4) = \frac{\mathrm{U}(4)}{\mathrm{U}(2)\times\mathrm{U}(2)}, \tag{4.50}$$

and one has to find the global minimum of thermodynamic potential (4.48) on this eight-dimensional manifold. We examine only some local minimums corresponding to the phases that has been previously discussed in the literature.

The minimization of (4.48) over valley-isospin-diagonal matrices Q yields

$$Q = T_{30}\cos\theta + (T_{13}\cos\phi + T_{23}\sin\phi)\sin\theta, \tag{4.51}$$

where the angle ϕ describes the orientation of the antiferromagnetic vector in the plane perpendicular to the magnetic field, and

$$\cos\theta = \begin{cases} 1, & Z > -2u_\perp \quad \text{(F phase)} \\ -\dfrac{Z}{2u_\perp}, & Z < -2u_\perp \quad \text{(CAF phase)} \end{cases} \tag{4.52}$$

determines the angle θ between the spin polarization (ferromagnetic) vector and the direction of magnetic field ($Z > 0$ is assumed). In the ferromagnetic (F) phase,

$$\mathcal{M}_n = -\mu_0 - \tilde{\Delta}_0 T_{03} + \left(Z + \frac{I_{n+1}(x) + I_{n+2}(x)}{2ml^2} + \frac{u_0 + u_z}{2} + u_\perp\right)T_{30} \tag{4.53}$$

and the free energy is equal to

$$\mathcal{F} = -\frac{1}{2\pi l^2}\left\{\frac{1}{2ml^2}[I_1(x) + 2I_2(x) + I_3(x)] + 4Z + u_0 + u_z + 2u_\perp\right\}. \tag{4.54}$$

For the canted antiferromagnetic (CAF) phase, we have

$$\mathcal{M}_n = -\mu_0 - \tilde{\Delta}_0 T_{03} + \left(\frac{I_{n+1}(x) + I_{n+2}(x)}{2ml^2} + \frac{u_0 + u_z}{2} - u_\perp\right)Q \tag{4.55}$$

and

$$\mathcal{F} = -\frac{1}{2\pi l^2}\left\{\frac{1}{2ml^2}[I_1(x) + 2I_2(x) + I_3(x)] - \frac{Z^2}{u_\perp} + u_0 + u_z - 2u_\perp\right\}. \tag{4.56}$$

The same results can be obtained directly by solving the gap equation (4.29) with the matrices $\mathcal{M}_n$ taken as general valley-isospin-diagonal Hermitian matrices. If we choose the matrices $\mathcal{M}_n$ to be diagonal in the (real) spin states instead, the analytical calculations can be carried out only in the simplified case $I_1(x) = I_3(x)$, $I_1^{\mathrm{IL}}(x) = I_3^{\mathrm{IL}}(x)$. In this approximation, one has

$$Q = T_{03}\cos\vartheta + (T_{01}\cos\varphi + T_{02}\sin\varphi)\sin\vartheta \tag{4.57}$$

where the angle φ describes the orientation of the xy component in the valley isospin space corresponding tot the Kekulé distortion (KD) order parameter, and

$$\cos\vartheta = \begin{cases} -\operatorname{sgn}\tilde{\Delta}_0, & |\tilde{\Delta}_0| > u_z - u_\perp + 2\alpha - \beta \qquad \text{(LP phase)} \\ \dfrac{\tilde{\Delta}_0}{u_\perp - u_z + \beta - 2\alpha}, & |\tilde{\Delta}_0| < u_z - u_\perp + 2\alpha - \beta \qquad \text{(PLP phase)} \end{cases} \tag{4.58}$$

where

$$\alpha \equiv \frac{e^2 d}{\kappa l^2}, \qquad \beta \equiv \frac{1}{4ml^2}[I_1^{\mathrm{IL}}(x) + 2I_2^{\mathrm{IL}}(x) + I_3^{\mathrm{IL}}(x)], \tag{4.59}$$

determines the ratio between the KD and the layer-polarized (LP) orders ($\tilde{\Delta}_0 > 0$ is assumed). In the purely LP phase ($\sin\vartheta = 0$),

$$\mathcal{M}_n = -\mu_0 + ZT_{30} - \left[\tilde{\Delta}_0 + \left(\frac{I_{n+1}(x) + I_{n+2}(x)}{2ml^2} + \frac{u_0 - 3u_z}{2} - u_\perp\right)\operatorname{sgn}\tilde{\Delta}_0\right]T_{03} \tag{4.60}$$

and the free energy is equal to

$$\mathcal{F} = -\frac{1}{2\pi l^2}\left\{\frac{1}{2ml^2}[I_1(x) + 2I_2(x) + I_3(x)] + 4|\tilde{\Delta}_0| + u_0 - 2u_\perp - 3u_z - 4\alpha\right\}. \tag{4.61}$$

For the partially layer polarized (PLP) phase, we have

$$\mathcal{M}_n = -\mu_0 + ZT_{30} + \left(\frac{I_{n+1}(x) + I_{n+2}(x)}{2ml^2} - \beta + \frac{u_0 - u_z}{2} - 2u_\perp\right)Q \tag{4.62}$$

and

$$\mathcal{F} = -\frac{1}{2\pi l^2}\left\{\frac{1}{2ml^2}[I_1(x) + 2I_2(x) + I_3(x)] - 2\beta - \frac{2\tilde{\Delta}_0^2}{u_\perp - u_z + \beta - 2\alpha} + u_0 - u_z - 4u_\perp\right\}. \tag{4.63}$$

In the unbiased case ($\tilde{\Delta}_0 = 0$), the $\tilde{\tau}_3$-component of the PLP order parameter vanishes and one has purely KD state.

Comparing the free energies in the different phases, we obtain the following equations for the phase boundaries:

- F-CAF:
$$u_\perp + \frac{Z}{2} = 0; \tag{4.64}$$

- F-LP:
$$u_z + u_\perp + \alpha + Z - |\tilde{\Delta}_0| = 0; \tag{4.65}$$

- CAF-LP (exists only if $\alpha < \beta$):
$$u_z + \alpha - \frac{Z^2}{4u_\perp} - |\tilde{\Delta}_0| = 0; \tag{4.66}$$

- F-PLP (exists only if $\alpha > \beta$):
$$2Z + u_z + 3u_\perp + \beta - \frac{\tilde{\Delta}_0^2}{2\alpha - \beta + u_z - u_\perp} - \frac{Z^2}{2u_\perp} = 0; \tag{4.67}$$

- LP-PLP:
$$u_z - u_\perp + 2\alpha - \beta - |\tilde{\Delta}_0| = 0; \tag{4.68}$$

- PLP-CAF:
$$u_z + u_\perp + \beta - \frac{\tilde{\Delta}_0^2}{2\alpha - \beta + u_z - u_\perp} - \frac{Z^2}{2u_\perp} = 0. \tag{4.69}$$

These phases are shown on Fig. 4.1 for three cases of parameters α and β defined in Eq. (4.59). The second case, $\alpha = \beta$, is realized when all symmetry-breaking interactions are local and has been considered in Ref. [20]. Indeed, if one replaces the layer-asymmetric part of the long-range Coulomb potential $V_{IL}(u)$ with the contact interaction

$$V^{\mathrm{IL}}(u) \to G^{\mathrm{IL}}_{\mathrm{int}} \delta^3(u), \tag{4.70}$$

one has instead of (4.59)

$$\alpha = \beta = -\frac{G^{IL}_{\mathrm{int}}}{2\pi l^2}, \tag{4.71}$$

which is equivalent to redefining the coupling constants

$$u_0 \to u_0 + \frac{G^{\mathrm{IL}}_{\mathrm{int}}}{2\pi l^2}, \qquad u_z \to u_z - \frac{G^{\mathrm{IL}}_{\mathrm{int}}}{2\pi l^2}. \tag{4.72}$$

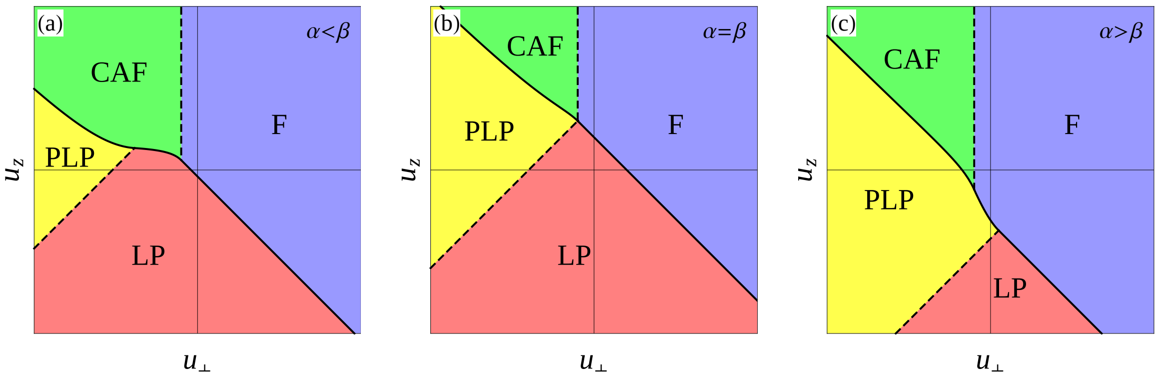

Figure 4.1: Phase diagram of the $\nu = 0$ state in the $(u_\perp, u_z)$ plane in three cases: (a) $\alpha < \beta$, (b) $\alpha = \beta$, (c) $\alpha > \beta$. Solid (dashed) lines correspond to the first (second) order phase transitions.

In our model with the long-range Coulomb interactions,

$$\alpha = \frac{e^2 d}{\kappa l^2} \simeq \frac{0.77}{\kappa} B_\perp[\mathrm{T}]\,\mathrm{meV}, \tag{4.73}$$

and the parameter β depends on the integrals $I_n^{\mathrm{IL}}(x)$, $n = 1, 2, 3$. Taking into account that $d/l \simeq 0.013\sqrt{B[\mathrm{T}]} \ll 1$, we obtain from Eq. (4.36):

$$I_n^{\mathrm{IL}}(x) \simeq \int\limits_0^\infty \frac{dy\, e^{-y} f_n(y) \sqrt{2y} d/l}{\kappa\sqrt{xy} + 2\pi\tilde{\Pi}_-(y)\sqrt{2y} d/l} \simeq \int\limits_0^\infty \frac{dy\, e^{-y} f_n(y)}{2.8\kappa + 2\pi\tilde{\Pi}_-(y)}. \tag{4.74}$$

This expression dependent on magnetic field strength only through the value of the summation cutoff in Eq. (4.38). Evaluating (4.74) numerically for different values of κ and $n_{\max}$, we find that the inequality $\alpha > \beta$ is always satisfied. This implies that the case shown in Fig. 4.1(c) always takes place.

Parameters Z and $\tilde{\Delta}_0$ can be tuned experimentally by tilting the magnetic field and changing the gate voltage, respectively. Taking such values of parameters u_z and $u_\perp$ that in the absence of electric field ($\tilde{\Delta}_0 = 0$) and at small Z the system is in the CAF state, we obtain the phase diagram in the $(Z, \tilde{\Delta}_0)$ plane shown in Fig. 4.2. It qualitatively agrees with the experimental results of Ref. [13], although our model predicts the same slope

$$\frac{\partial|\tilde{\Delta}_0|}{\partial Z} = 1 \tag{4.75}$$

for the and F-LP transition as given by Refs. [15, 20] and almost the same slope for the F-PLP

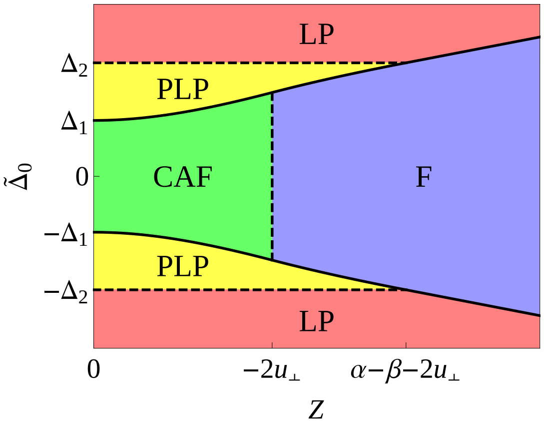

Figure 4.2: Phase diagram of the $\nu = 0$ state in the $(Z, \tilde{\Delta}_0)$ plane in the case $\alpha > \beta$. Solid (dashed) lines correspond to the first (second) order phase transitions, $\Delta_1 \equiv \sqrt{\Delta_2(u_z + u_\perp + \beta)}$, $\Delta_2 \equiv u_z - u_\perp + 2\alpha - \beta$.

transition, while the experimental value is [13]

$$\frac{\partial|\tilde{\Delta}_0|}{\partial Z} \approx 4. \tag{4.76}$$

In comparison with Ref. [20], where only the local interaction terms were considered and all four phases met at a single point, our model predicts the finite F-PLP phase boundary.

4.5 Filling factors $\nu = \pm 2$

In the case $\nu = 2$ (the solutions for the filling factor $\nu = -2$ can be obtained by changing the signs of the energies), the matrix Q has eigenvalues $(-1, -1, -1, +1)$. To find the global minimum of thermodynamic potential (4.48) on the six-dimensional manifold U(4)/[U(1) × U(3)], which we parametrize as

$$Q = -\mathbb{1}_4 + 2WW^\dagger, \tag{4.77}$$

where the unit vector

$$W = \begin{pmatrix} \cos\theta_1 \\ \sin\theta_1 \cos\theta_2 e^{i\phi_1} \\ \sin\theta_1 \sin\theta_2 \cos\theta_3 e^{i\phi_2} \\ \sin\theta_1 \sin\theta_2 \sin\theta_3 e^{i\phi_3} \end{pmatrix}, \tag{4.78}$$

depends on six real variables (angles) θ_i, ϕ_i, $i = 1, 2, 3$. Equation (4.49), reduces to

$$X_{\alpha\beta} = -\delta_{\alpha 0}\delta_{\beta 0} + \frac{1}{2}W^\dagger T_{\alpha\beta}W, \qquad Y_{\alpha\beta} = \frac{1}{4}(W^\dagger T_{\alpha\beta}W)^2, \tag{4.79}$$

and the free energy (4.48) reads

$$\mathcal{F} = -\frac{\nu_0 + \nu_2 + 2\nu_1}{8\pi l^2} - \frac{1}{\pi l^2}\Big[-\tilde{\Delta}_0 W^\dagger T_{03}W + ZW^\dagger T_{30}W + \frac{\beta-\alpha}{2}(W^\dagger T_{03}W)^2\Big]. \tag{4.80}$$

Note that for all local interaction terms, the Hartree and Fock contributions to the free energy cancel out in the case $\nu = 2$. Using (4.78), we have

$$W^\dagger T_{03}W = 2(c_1 + c_3 - c_1c_3 - c_2c_3 + c_1c_2c_3) - 1, \tag{4.81}$$

$$W^\dagger T_{30}W = 2(c_1 + c_2 - c_1c_2) - 1, \qquad c_i \equiv \cos^2\theta_i, \quad i = 1, 2, 3. \tag{4.82}$$

Thus, we need to maximize the expression

$$\begin{aligned} &-\tilde{\Delta}_0[2(c_1 + c_3 - c_1c_3 - c_2c_3 + c_1c_2c_3) - 1] + Z[2(c_1 + c_2 - c_1c_2) - 1] \\ &\qquad + \frac{\beta-\alpha}{2}[2(c_1 + c_3 - c_1c_3 - c_2c_3 + c_1c_2c_3) - 1]^2 \end{aligned} \tag{4.83}$$

over $c_1, c_2, c_3 \in [0, 1]$. In the case $\alpha < \beta + |\tilde{\Delta}_0|$, the maximum is reached at $c_1 = 0$, $c_2 = 1$ (c_3 can be arbitrary) if $\tilde{\Delta}_0 > 0$, or at $c_1 = 1$ (c_2, c_3 can be arbitrary) if $\tilde{\Delta}_0 < 0$, which implies

$$Q = -\begin{pmatrix} \tilde{\tau}_3 \operatorname{sgn}\tilde{\Delta}_0 & 0 \\ 0 & \tilde{\tau}_0 \end{pmatrix}. \tag{4.84}$$

The matrix $\mathcal{M}_n$ can be written as

$$\begin{aligned} \mathcal{M}_n = &-\mu_0 - u_\perp + (Z + u_\perp)T_{30} - [\tilde{\Delta}_0 + (u_z - \alpha)\operatorname{sgn}\tilde{\Delta}_0]T_{03} \\ &+ \left(\frac{I_{n+1}(x) + I_{n+2}(x)}{2ml^2} + \frac{u_0 + u_z}{2} - u_\perp\right)Q \end{aligned} \tag{4.85}$$

and the free energy is equal to

$$\mathcal{F} = -\frac{1}{2\pi l^2}\left\{\frac{1}{2ml^2}[I_1(x) + 2I_2(x) + I_3(x)] + 2|\tilde{\Delta}_0| + 2Z + u_0 - \alpha\right\}. \tag{4.86}$$

This result coincides with the one obtained in Ref. [15], where this phase is called a partially spin-layer polarized (PSLP) solution.

In the case $\alpha > \beta + |\tilde{\Delta}_0|$, the maximum is reached at $2c_1 = 1 - \tilde{\Delta}_0/(\alpha - \beta)$, $c_2 = 1$ (c_3 can be arbitrary), which implies

$$Q = -\begin{pmatrix} \tilde{\tau}_3 \cos\vartheta + (\tilde{\tau}_1 \cos\varphi + \tilde{\tau}_2 \sin\varphi)\sin\vartheta & 0 \\ 0 & \tilde{\tau}_0 \end{pmatrix}, \qquad \cos\vartheta = \frac{\tilde{\Delta}_0}{\alpha - \beta}. \tag{4.87}$$

The matrix $\mathcal{M}_n$ can be written as

$$\mathcal{M}_n = -\mu_0 + ZT_{30} + \left(\frac{I_{n+1}(x) + I_{n+2}(x)}{2ml^2} - \beta + \frac{u_0 - u_z}{2} - u_\perp\right)Q - \begin{pmatrix} 0 & 0 \\ 0 & \tilde{\tau}_{\mathcal{M}} \end{pmatrix}, \tag{4.88}$$

where

$$\tilde{\tau}_{\mathcal{M}} \equiv u_z + 2u_\perp + \beta + (\tilde{\Delta}_0 - u_z \cos\vartheta)\tilde{\tau}_3 + u_\perp(\tilde{\tau}_1 \cos\varphi + \tilde{\tau}_2 \sin\varphi)\sin\vartheta, \tag{4.89}$$

and the free energy is equal to

$$\mathcal{F} = -\frac{1}{2\pi l^2}\left\{\frac{1}{2ml^2}[I_1(x) + 2I_2(x) + I_3(x)] + \frac{\tilde{\Delta}_0^2}{\alpha - \beta} + 2Z + u_0 - \beta\right\}. \tag{4.90}$$

According to the numerical result $\alpha > \beta$, this ground state is always energetically favourable in the absence of the perpendicular electric field ($\tilde{\Delta}_0 = 0$). This phase with the ferromagnetic-like polarization in the spin space and Kekulé order in the valley isospin space has been suggested as a candidate for the observed at strong magnetic fields at filling factor $\nu = 2$ in Ref. [12]. It has a lower free energy than the PSLP phase due to the absence of the electrostatic layer polarization energy cost [the Hartree term proportional to α in Eq. (4.86)] which is larger than the exchange term proportional to β in Eq. (4.90). When $0 < |\tilde{\Delta}_0| < \alpha - \beta$, the valley-isospin angle has also a $\tilde{\tau}_3$ component and upon changing $|\tilde{\Delta}_0|$ from 0 to $\alpha - \beta$ the state continuously evolves to the PSLP phase.

4.6 Conclusions

In this chapter, the analysis of Refs. [14,15] has been extended to the case of a general (nondiagonal) order parameter matrix and performed taking into account the additional local symmetry-breaking interaction terms. We derived the general gap equation in the LLL approximation with the screened Coulomb interaction and the static approximation for the polarization function. We also derived the expression for the free energy density, which depends only on the quantum numbers of the filled and empty LLL sublevels. The minimization of the free energy and solving the gap equation has been done for the even filling factors $\nu = 0, \pm 2$.

The solutions of the gap equation in the case $\nu = 0$ agree with the previously obtained results [20] in the case of the local interactions. The nonlocality of the layer-asymmetric part of the Coulomb interaction leads to the modification of the phase diagram, in particular, the transition between the F and the PLP becomes possible. The phase transitions predicted by the considered model upon changing electric fields and the tilt angles of magnetic field qualitatively agree with the experiment [13].

For the case of filling factors $\nu = \pm 2$, we find that at large values of the electric field, the ground state is both spin and layer polarized. At smaller fields, in continuously evolves to a phase where the layer polarization coexists with the Kekulé order (interlayer coherence).

Taking into account that the static screening approximation substantially underestimates the strength of the Coulomb interaction [16], it would be important to incorporate the dynamical (frequency-dependent) polarization function in the gap equation. Also, while the use of LLL approximation is justified in the case of the LL energy separation exceeding the interaction-induced gaps [14, 15], a more accurate description requires including the higher LLs in the analysis.

Bibliography

[1] E. McCann and M. Koshino, Rep. Prog. Phys. **76**, 056503 (2013).

[2] K. S. Novoselov, E. McCann, S. V. Morozov, V. I. Fal'ko, M. I. Katsnelson, U. Zeitler, D. Jiang, F. Schedin, and A. K. Geim, Nat. Phys. **2**, 177 (2006).

[3] B. E. Feldman, J. Martin, and A. Yacoby, Nat. Phys. **5**, 889 (2009).

[4] Y. Zhao, P. Cadden-Zimansky, Z. Jiang, and P. Kim, Phys. Rev. Lett. **104**, 066801 (2010).

[5] R. T. Weitz, M. T. Allen, B. E. Feldman, J. Martin, and A. Yacoby, Science **330**, 812 (2010).

[6] J. Martin, B. E. Feldman, R. T. Weitz, M. T. Allen, and A. Yacoby, Phys. Rev. Lett. **105**, 256806 (2010).

[7] S. Kim, K. Lee, and E. Tutuc, Phys. Rev. Lett. **107**, 016803 (2011).

[8] F. Freitag, J. Trbovic, M. Weiss, and C. Schönenberger, Phys. Rev. Lett. **108**, 076602 (2012).

[9] J. Velasco, J., L. Jing, W. Bao, Y. Lee, P. Kratz, V. Aji, M. Bockrath, C. N. Lau, C. Varma, R. Stillwell, D. Smirnov, F. Zhang, J. Jung, and A. H. MacDonald, Nat. Nanotechnol. **7**, 156 (2012).

[10] H. van Elferen, A. Veligura, E. Kurganova, U. Zeitler, J. Maan, N. Tombros, I. Vera-Marun, and B. van Wees, Phys. Rev. B **85**, 115408 (2012).

[11] J. Velasco, Y. Lee, Z. Zhao, L. Jing, P. Kratz, M. Bockrath, and C. N. Lau, Nano Lett. **14**, 1324 (2014).

[12] J. Velasco, Jr, Y. Lee, F. Zhang, K. Myhro, D. Tran, M. Deo, D. Smirnov, A. H. MacDonald, and C. N. Lau, Nat. Commun. **5**, 4550 (2014).

[13] P. Maher, C. R. Dean, A. F. Young, T. Taniguchi, K. Watanabe, K. L. Shepard, J. Hone, and P. Kim, Nat. Phys. **9**, 154 (2013).

[14] E. V. Gorbar, V. P. Gusynin, and V. A. Miransky, Phys. Rev. B **81**, 155451 (2010).

[15] E. V. Gorbar, V. P. Gusynin, J. Jia, and V. A. Miransky, Phys. Rev. B **84**, 235449 (2011).

[16] E. V. Gorbar, V. P. Gusynin, V. A. Miransky, and I. A. Shovkovy, Phys. Rev. B **85**, 235460 (2012).

[17] E. V. Gorbar, V. P. Gusynin, and V. A. Miransky, JETP Letters **91**, 314 (2010).

[18] R. Nandkishore and L. Levitov, arXiv:1105.2026 .

[19] C. Tőke and V. I. Fal'ko, Phys. Rev. B **83**, 115455 (2011).

[20] M. Kharitonov, Phys. Rev. Lett. **109**, 046803 (2012).

[21] M. Kharitonov, Phys. Rev. B **86**, 075450 (2012).

[22] M. Kharitonov, Phys. Rev. B **86**, 195435 (2012).

[23] K. Dhochak, E. Shimshoni, and E. Berg, arXiv:1409.1241 .

[24] Y. Barlas, R. Côté, K. Nomura, and A. MacDonald, Phys. Rev. Lett. **101**, 097601 (2008).

[25] D. Abanin, S. Parameswaran, and S. Sondhi, Phys. Rev. Lett. **103**, 076802 (2009).

Chapter 5

Conclusions

In this thesis, we studied different broken-symmetry quantum Hall phases in monolayer and bilayer graphene and the properties of edge excitations corresponding to these phases. Within the effective low-energy continuum model, we calculated the edge state spectrum in both monolayer and bilayer graphene with the splitting of the lowest Landau level. Cases with the current-carrying gapless edge states that may be observed in experiments have been identified. We also solved the gap equation in bilayer graphene in the presence of general symmetry-breaking terms and obtained the phase diagram for different values of external electric field and tilt angles of the magnetic field.

In Chapter 1, we reviewed the basic features of the low-energy continuum models for monolayer and bilayer graphene, the structure of the bulk and edge state energy spectrum in the presence of external magnetic field, and different sources of the symmetry breaking.

In Chapter 2, we considered bilayer graphene in an external magnetic field without dynamical symmetry breaking, when the LLL splitting is induced by the external electric field. Using the four-band continuum model, we derived the analytic expressions for the wave functions and the dispersion equations for graphene ribbons or semi-infinite planes with zigzag or armchair edges. These dispersion equations have been solved numerically and the edge state spectra for each type of the boundary were obtained. We have found that the gapless edge states are present only in the case of zigzag edge. At weak intervalley scattering, these states are expected to carry the edge currents and lead to the finite conductivity of the $\nu = 0$ quantum Hall state. We also explored the behavior of zigzag edge states in the limit of a small magnetic field at a fixed value of the perpendicular electric field. It would be interesting to extend this analysis to the case of different order parameters that can be generated dynamically.

In Chapter 3, we derived and solved numerically the dispersion equations for the edge excitations of different $\nu = 0$ quantum Hall states with dynamically broken symmetry in monolayer graphene. Using two different approaches, the continuum Dirac Hamiltonian and the tight-binding equations, we calculated the edge state spectra in the mean-field model with the charge density wave, Kekulé distortion, ferromagnetic, and (canted) antiferromagnetic order parameters. The criteria for the existence of gapless edge states are formulated for each broken-symmetry phase and boundary type. We also show that the next-to-nearest neighbor hopping parameter has a crucial effect on the edge state properties in the case of zigzag boundary. An important question that should be addressed in the future studies is whether the gapless edge excitations found in some phases indeed lead to a conducting state or they are modified substantially when the spatial variation of the order parameters is taken into account.

In Chapter 4, we explored the broken-symmetry quantum Hall phases at even filling factors in bilayer graphene. Phase transitions caused by the interplay between different symmetry-breaking terms were analyzed by solving the gap equation in the LLL approximation with the long-range Coulomb screened potential and the static polarization function. For the case $\nu = 0$, we obtained the modification of the phase diagram due to the long-range part of the layer-asymmetric Coulomb interaction. For the filling factor $\nu = \pm 2$, two possible ground states have been revealed with the continuous phase transition taking place upon changing the external electric field. It would be interesting to generalize our study to the case of odd filling factors and include the effects of Landau level mixing and dynamically screened Coulomb potential.

Curriculum Vitae

Name:	Pavlo Piatkovskyi
Post-Secondary Education and Degrees:	Kyiv National Taras Shevchenko University Kyiv, Ukraine 2001 - 2005 B.Sc.
	Kyiv National Taras Shevchenko University Kyiv, Ukraine 2005 - 2006 M.Sc.
	The University of Western Ontario London, Ontario, Canada 2009 - 2010 M.Sc.
	The University of Western Ontario London, Ontario, Canada 2011 - 2014 Ph.D. candidate
Honours and Awards:	Ontario Graduate Scholarship 2012–2013, 2013–2014, 2014–2015
	UWO Faculty of Science Graduate Student Teaching Assistant Award 2013–2014
Related Work Experience:	Teaching Assistant The University of Western Ontario 2009 - 2014

Publications:

P. K. Pyatkovskiy, *Dynamical polarization, screening, and plasmons in gapped graphene*,
J. Phys.: Condens. Matter **21**, 025506 (2009).

P. K. Pyatkovskiy and V. P. Gusynin, *Dynamical polarization of graphene in a magnetic field*,
Phys. Rev. B **83**, 075422 (2011).

P. K. Pyatkovskiy, *Edge states in bilayer graphene in a magnetic field*,
Phys. Rev. B **88**, 205417 (2013).

P. K. Pyatkovskiy and V. A. Miransky, *Spectrum of edge states in the* $\nu = 0$ *quantum Hall phases in graphene*, Phys. Rev. B **90**, 195407 (2014).